# AN ABSTRACT OF THE THESIS OF

Juan Muglia for the degree of Doctor of Philosophy in Ocean, Earth, and Atmospheric Sciences presented on June 12, 2017.

Title: The Ocean Circulation and Carbon Cycle during the Last Glacial Maximum

Abstract approved: _____

Andreas Schmittner

During the Last Glacial Maximum (LGM, $\sim$ 21 ky before present) the atmospheric $CO_2$ concentration was about 100 ppm lower than its pre-industrial (PI) value. The missing carbon from the atmosphere must have been stored in the deep ocean during this period, but the mechanisms driving such re-distribution of the carbon cycle are still uncertain. LGM-PI changes in circulation, stratification, and/or biogeochemistry have been suggested to enhance ocean carbon storage, but quantitative, three-dimensional, data-constrained estimates of these effects remain scarce.

The most recent simulations from the Paleoclimate Model Intercomparison Project 3 (PMIP3) predict an increase and deepening of the LGM Atlantic Meridional Overturning Circulation (AMOC) with respect to PI simulations, although

this is inconsistent with the interpretation of most sedimentary proxy data attributed to this period. The goal of this dissertation is to use an ocean model to constrain the LGM global ocean circulation and biogeochemistry, and asses their effects on the carbon cycle.

We use a three dimensional global circulation model, coupled with a biogeochemical model that includes the interactive cycles of radiocarbon ($^{14}$C), $^{13}$C and $^{15}$N. The inclusion of these three isotopes provides a powerful tool to constrain the possible LGM scenarios, since model results can be directly compared to measurements of the same isotopes from the sediment records. Our physical LGM model set up includes changes in atmospheric $CO_2$, continental ice sheets, orbital parameters and circulation.

By varying meridional moisture transport of the model's atmospheric component, we produce LGM circulations with different AMOC strengths and depths, from a collapsed state, to a strong state similar to PMIP3 models. We find that a weak ($6-9$ Sv) and shallow AMOC underlaid by a more voluminous and carbon-rich Antarctic Bottom Water (AABW) best reproduces glacial $\delta^{13}$C and radiocarbon ages from sedimentary data. This configuration of water masses also maximizes the amount of remineralized organic carbon stored in deep waters. We propose that increased wind stress over the North Atlantic stabilizes the weak AMOC and prevents it from collapsing.

We also evaluate effects of PI-to-LGM changes in atmospheric dust, sedimentary, and hydrothermal fluxes on the ocean's iron and carbon cycles. We find that iron fertilization caused by enhanced dust deposition in the LGM is strongly coun-

tered by a decrease in sedimentary flux due to 125 m lower sea level, which tends to decrease primary productivity. In an upper-limit estimation of Southern Ocean atmospheric iron fertilization, assuming an increase in soluble iron deposition of the order of $\sim 10-20$ times its PI value for this region, combined with changes in sedimentary flux, we obtain higher export production and enhanced accumulation of remineralized organic carbon in deep waters, which would lead to atmospheric carbon sequestration. This bigeochemical state also improves the agreement with $\delta^{13}$C and $\delta^{15}$N reconstructions from the LGM.

The combined results suggest that a weak and shallow AMOC and enhanced iron fertilization conspired to maximize carbon storage in the glacial ocean, and produce part of the glacial-interglacial variations in atmospheric $CO_2$ concentrations.

# The Ocean Circulation and Carbon Cycle during the Last Glacial Maximum

by

Juan Muglia

A THESIS

submitted to

Oregon State University

in partial fulfillment of
the requirements for the
degree of

Doctor of Philosophy

Presented June 12, 2017
Commencement June 2018

Doctor of Philosophy thesis of Juan Muglia presented on June 12, 2017.

APPROVED:

---

Major Professor, representing Ocean, Earth, and Atmospheric Sciences

---

Dean of the College of Earth, Ocean and Atmospheric Sciences

---

Dean of the Graduate School

I understand that my thesis will become part of the permanent collection of Oregon State University libraries. My signature below authorizes release of my thesis to any reader upon request.

---

Juan Muglia, Author

# ACKNOWLEDGEMENTS

To complete a Doctorate of Philosophy program is a process that requires patience, work and commitment from the student. However, it also requires the support, guidance, friendship, and commitment from mentors, teachers, friends, family, colleagues... At the moment of the completion of my dissertation, I am happy to say that I have been very fortunate during this five year period and had all the support I needed.

I first want to thank my advisor and mentor, Dr. Andreas Schmittner. After I applied to graduate school in Oregon State University, he contacted me in early 2012 to offer me a position as a PhD student in his laboratory, to do research on the topic of paleoceanography, a field I had never heard of. I decided to accept his offer, and I am very thankful that I did. Since then he has been a tremendously good mentor for me. He guided me through research, but always letting me make my own decisions on the direction of my work. He heard me, and taught me whenever I needed, and we have discussed science for hours. He supported me to go to many conferences and meetings, and has been very generous by including me in various of his research projects. I hope our scientific and personal relationship continues in the future.

The National Science Foundation was the funding source of my PhD studies and living wages during these five years, through the Marine Geology and Geophysics program (OCE-1131834, OCE-1235544), obtained by Dr. Schmittner. I thus acknowledge this agency, Dr. Schmittner, and Oregon State Unversity, for

providing me with the graduate research assistantship than funded my PhD studies from start to finish.

I also want to thank the members of my committee, Ed Brook, Ricardo Matano, Alan Mix, and Yvette Spitz, for guidance during my studies. Ricardo Matano has always been very generous with me, helping me get installed in Corvallis when I first arrived, and is always there to give me a hand when I needed it.

For the scientific discussions during the time they formed part of Andreas Schmittner's lab, I want to thank Pepijn Bakker and David Ullman. I also thank Chris Somes, who continues to collaborate and give ideas from Germany.

Studying is more fun when you do it with friends, and I cannot leave out from this acknowledgements page (has it gone over a page already?) my class mate, office mate, and friend, Jenny Thomas. We have been through a lot together and we continue being friends and support for each other. I have met many other good friends in my time in Corvallis. This thesis was possible in part thanks to those who are always there for a few laughs in the precise time: Gabriel, Mara, Gonzalo, Vincent, Alejandra, Raul, Isabel, Dolores, Jenessa, Andrea, Diego, Fabian...

I also want to thank the two organizations I am part of, the Association of Latin American Students and the Coalition of Graduate Employees, for existing and for the different kinds of support they give to students.

Finally, I am forever thankful of my family, for existing and being a part of me. One thanks to my big family, in Argentina, and one thanks to my small (but growing!) family here in Corvallis: Patricia and Salvador, who share with me the joy of living.

And a last one: In 2012 I came from a different country to the United States to study, work, travel, form a family. This country and its people have been very generous to me for the past five years. Let this generosity be a common value in all countries and to all people who go from one place to another in the present and in the future.

# CONTRIBUTION OF AUTHORS

For Chapter 2, Juan Muglia performed the computer simulations, analysed results and wrote the manuscript. Andreas Schmittner provided the scientific idea and corrected the manuscript.

For Chapter 3, Juan Muglia provided scientific ideas, wrote code, performed the computer simulations, analysed results and wrote the manuscript. Christopher Somes and Levin Nickelsen wrote code and corrected the manuscript. Andreas Schmittner provided scientific ideas and corrected the manuscript.

For Chapter 4, Juan Muglia provided scientific ideas, performed the computer simulations, analysed results and wrote the manuscript. Luke Skinner provided data and corrected the manuscript. Andreas Schmittner provided data, provided scientific ideas and corrected the manuscript.

# TABLE OF CONTENTS

# TABLE OF CONTENTS (Continued)

# LIST OF FIGURES

# LIST OF FIGURES (Continued)

# LIST OF TABLES

# LIST OF TABLES (Continued)

# LIST OF APPENDIX FIGURES

# LIST OF APPENDIX FIGURES (Continued)

# LIST OF APPENDIX FIGURES (Continued)

# LIST OF APPENDIX TABLES

*In memory of my mom, Ana Maria Gayoso. If I am a scientist it is because of her.*

# Chapter 1: Introduction

## 1.1 Overview

The concentration of $CO_2$ and other trace gases in the atmosphere has varied through glacial/interglacial cycles (Marcott et al., 2014). In particular, during the Last Glacial Maximum (LGM, $\sim$ 21 kyears before present) the concentration of atmospheric $CO_2$ was about 100 ppm lower than in the pre-industrial (PI) climate (Fig. 1.1). This leads to an important scientific question: What are the physical and biogeochemical processes behind the low atmospheric $CO_2$ levels during glacial periods?

To address this question I will use a general circulation model of the world ocean, coupled with a model of biogeochemistry and isotopes, to find possible drivers for the differences between glacial and interglacial climates. In this thesis I focus on the LGM, because of its closeness to present times and the high availability of data collected from sediment and ice cores from this period. However, some of our conclusions may be extended to other glacial periods of similar characteristics.

## 1.2 Glacial Cycles and $CO_2$

For the past two million years the Earth's climate has experienced a series of cold and warm periods, referred to as glacial-interglacial cycles (Elderfield et al.,

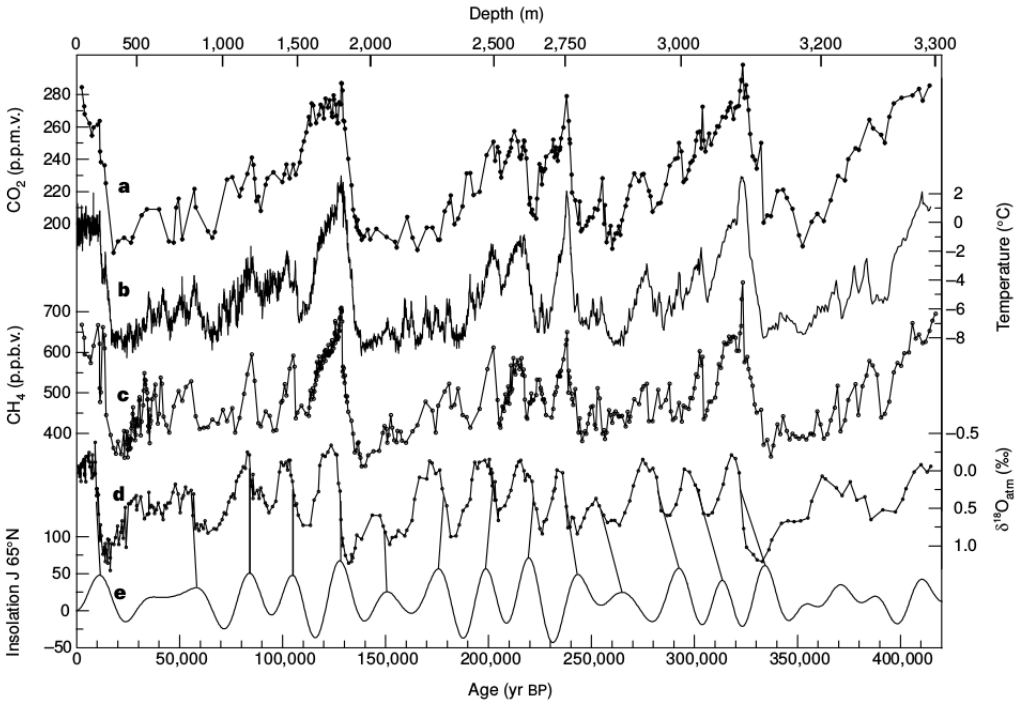


Figure 1.1: Reconstructed atmospheric temperature, trace gases $CO_2$ and $CH_4$, $\delta^{18}O$ (tracer of ice sheet volume), and predicted solar insolation for the past 400 kyears, from the Vostok Antarctic ice core. The remarkable correlation between temperature and $CO_2$ is still not well understood. Image taken from Petit et al. (1999).

2012). During glacial cycles mean surface atmospheric temperatures cool by $5-15$ °C (Petit et al., 1999), and massive ice sheets are formed above North America, northwest Europe and the Patagonian Andes (Clark et al., 2009).

Glacial cycles have been ultimately linked to variations in the eccentricity of the Earth's orbit with the Sun, the inclination of the Earth's axis and its precession angle, which affect the flux of radiation from the Sun reaching the planet and

seasonal patterns and amplitude (Hays et al., 1976). Lower temperatures and higher growth of ice sheets are expected to coincide with colder winters in the Northern Hemisphere.

From sediment and ice stratigraphy numerous properties have been observed to vary along glacial-interglacial cycles (Fig. 1.1). However, the mechanisms that link these properties and produce such variations are not always understood. An important case is atmospheric $CO_2$ concentration. From ice cores it has been observed that $CO_2$ (among other trace gases) varies along glacial cycles, with an amplitude of approximately 100 ppm, with the lower values occurring at cold periods. However, the connection between $CO_2$ and other properties that change periodically with glacial cycles, such as atmospheric temperature and ice sheet volume, is still not well understood.

## 1.3 The carbon pools during glacial periods

At the time scale of glacial cycles, and without taking into account anthropogenic changes, carbon in the climate system can be thought as partitioned among the atmosphere, land (biosphere and soil), the surface and deep ocean, and the sediments. If atmospheric $CO_2$ was lower during glacial periods, then the missing atmospheric carbon must have been stored in one of the other pools, with the ability of being restored back to the atmosphere at the onset of the subsequent deglaciations (Sigman and Boyle, 2000). But where was the carbon stored?

The isotopic ratio $^{13}C/^{12}C$ of benthic foraminifera shows lower values for the

LGM than for the PI. Since organic carbon has low $^{13}C/^{12}C$, this provides evidence that during the LGM there was a transfer of organic carbon from the biosphere to the ocean (Shackleton, 1977). From this isotopic signal and with the use of land vegetation models (e.g. Adams et al., 1990; Harrison and Prentice, 2003), it has been inferred that the carbon content of land was lower during the LGM, ruling it out as a possible storage for atmospheric carbon in glacial periods.

The surface ocean has high gas exchange with the atmosphere (Takahashi et al., 1997), and it lacks the potential to store large amounts of carbon. The deep ocean, on the other hand, has slower gas exchange with the atmosphere ($\sim 1000-5000$ y), and is the largest pool of carbon with an exchange rate on millennial timescales (Broecker, 1982). It could potentially drive glacial-interglacial changes in $CO_2$, storing higher amounts of carbon during glacial periods (Sigman and Boyle, 2000), and releasing them back to the atmosphere during deglaciations. Finding mechanisms through which glacial atmospheric carbon could have been transferred to the deep ocean is one of the most important problems in paleoceanography, and it is the focus of this thesis.

## 1.4 Mechanisms

Changes in ocean circulation, stratification, biogeochemistry, and carbon chemistry have been all proposed to explain the $CO_2$ difference between glacials and interglacials (Sigman and Boyle, 2000).

A voluminous, isolated deep ocean, with low gas exchange with the atmosphere

and high concentrations of remineralized organic carbon could have stored the missing atmospheric carbon. Reconstructions of stable carbon isotope ($^{13}C/^{12}C$) distributions from LGM benthic foraminifera found in sediments indicate that glacial North Atlantic Deep Water (NADW) was shallower, and more remineralized nutrients were accumulated in the deep Atlantic (Gebbie, 2014). At the same time, increased radiocarbon ($^{14}C$) ages of benthic foraminifera have been interpreted as evidence for a more sluggish circulation and more carbon storage (Sarnthein et al., 2013). In concordance with these findings, oxygen isotopes in benthic foraminifera have been used to reconstruct zonal density gradients across ocean basins, providing evidence that the Atlantic Meridional Overturning Circulation (AMOC) was slower during the LGM (Lynch-Stieglitz et al., 2007). However, the interpretation of other sediment data, such as the heavy metal ratio $^{231}Pa/^{230}Th$, indicate a strong glacial AMOC (Gherardi et al., 2009; Böhm et al., 2015).

An increase in biological production and export of organic matter would also transfer $CO_2$ from the atmosphere to deep waters during the LGM. In the present ocean, most of the surface Southern Ocean has high levels of nitrate and phosphate (Levitus et al., 2013), but low concentrations of dissolved iron (DFe), resulting in a large high-nutrient low-chlorophyll region. Higher Southern Ocean DFe concentrations, produced by increased dust deposition, could have intensified the productivity and export production of that region (Martin, 1990), although these processes are also influenced by other factors (e.g., Schmittner and Somes, 2016).

In addition to changes in circulation and/or biogeochemistry, changes in the marine carbonate chemistry could amplify atmospheric $CO_2$ flux to the ocean. The

entrainment of extra $CO_2$ to the surface ocean lowers pH and produces calcium carbonate dissolution at the sediment-water interface in deep water. This increases dissolved carbonate ion concentrations, which increase sea water alkalinity. To return to chemical equilibrium, the ocean takes up additional atmospheric $CO_2$ (Archer et al., 2000; Zeebe and Wolf-Gladrow, 2001). This process has been studied with different ocean models, obtaining atmospheric $CO_2$ draw downs of e.g., 12 ppm (Brovkin et al., 2007) and 40 ppm (Sigman et al., 2010). To include this effect in climate models the sediment carbonates have to be simulated, but the very slow equilibration time of that part of the system, of the order of several thousand years, makes it unfeasible to include them in most three dimensional models (Sigman and Boyle, 2000).

## 1.5 Thesis outline

In the present work we use a physical-biogeochemical model of the global ocean to study different scenarios that could have lead to a decrease in atmospheric $CO_2$ during the LGM. The model includes the interactive cycle of stable isotopes $^{15}N$ and $^{13}C$, as well as radiocarbon ($^{14}C$) which permits the direct comparison of model results to isotope reconstructions from sediments. The inclusion of three independent isotopes enables us to separate physical and biogeochemical effects on the carbon cycle, since the distribution of each isotope depends on different processes.

Apart from this introduction (which acts as chapter 1) the thesis is divided

into three chapters:

## Chapter 2: Wind stress increases glacial Atlantic overturning in climate models

*This chapter was published as a research letter in the journal Geophysical Research Letters (Muglia and Schmittner, 2015).*

We start our analysis by studying the glacial circulation of models from the Paleoclimate Model Intercomparison Project 3. We find that intensified wind stress over the North Atlantic Ocean, product of the the presence of the Laurentide ice sheet on North America, tends to strengthen and deepen the AMOC in these models. The effect dominates the Atlantic circulation, and we identify it as an important factor for the glacial ocean circulation. On the other hand, most indirect reconstructions suggest that the AMOC was shallower, and possibly weaker, than in modern times. In order to reproduce such a state in ocean models, another process has to be found, that could counter the strengthening of the AMOC by North Atlantic wind stress.

## Chapter 3: Combined effects of atmospheric and seafloor iron fluxes to the glacial ocean

*This chapter has been submitted as an article to the journal Paleoceanography and it is currently under review (Muglia et al., submitted).*

We move our attention to the biogeochemistry of the glacial ocean. The biogeochemical effects of changes in the fluxes of iron to the glacial ocean are studied. We include variations in atmospheric dust, sedimentary, and hydrothermal fluxes, according to LGM estimates. We find that higher dust and hydrothermal fluxes increase global primary productivity and export production, enhancing the accumulation of remineralized organic carbon in the deep ocean. However, the effect is countered by a decrease in the sedimentary flux of iron, caused by the exposure of continental shelves due to lower sea level in the glacial ocean, that tends to decrease primary productivity globally. Only with Southern Ocean atmospheric iron fertilization $\geq 10$ times the preindustrial flux can the sedimentary effect be countered and there be an iron fertilization effect that decreases atmospheric $CO_2$ concentrations.

## Chapter 4: Weak overturning circulation and increased iron fertilization maximized carbon storage in the glacial ocean

*This chapter is in preparation to be sent as an article to a scientific journal.*

We combine the findings of the two previous chapters. The strong AMOC from Chapter 2 is compared to weaker circulation states, generated by decreasing the meridional moisture transport to the Southern Ocean. We use the physical-biogeochemical model constrained by carbon and nitrogen isotopes to explore the effects of AMOC differences and Southern Ocean iron fertilization on the distributions of these isotopes and ocean carbon storage. We find that a weak ($6 - 9$

Sv) and shallow AMOC maximizes carbon storage and best reproduces the sediment data. Increasing the atmospheric soluble iron flux in the Southern Ocean intensifies export production, carbon storage, and improves agreement with isotope reconstructions. Our best fitting model suggests that a weak, shallow AMOC and enhanced iron fertilization conspired to maximize carbon storage in the glacial ocean.

# Chapter 2: Wind stress increases glacial Atlantic overturning in climate models

Juan Muglia[1] and Andreas Schmittner[1]

[1]College of Earth, Ocean and Atmospheric Sciences, Oregon State University, Corvallis, USA

## 2.1 Abstract

Previous Paleoclimate Model Intercomparison Project (PMIP) simulations of the Last Glacial Maximum (LGM) Atlantic Meridional Overturning Circulation (AMOC) showed dissimilar results on transports and structure. Here we analyze the most recent PMIP3 models, which show a consistent increase (on average by $41 \pm 26\,\%$) and deepening ($663 \pm 550$ m) of the AMOC with respect to pre-industrial simulations, in contrast to some reconstructions from proxy data.

Simulations run with the University of Victoria (UVic) ocean circulation model suggest that this is caused by changes in the Northern Hemisphere wind stress,

brought about by the presence of ice sheets over North America in the LGM. When forced with LGM wind stress anomalies from PMIP3 models, the UVic model responds with an increase of the northward salt transport in the North Atlantic, which strengthens North Atlantic Deep Water formation and the AMOC. These results improve our understanding of the LGM AMOC's driving forces, and suggest that some ocean mechanisms may not be correctly represented in PMIP3 models, or some proxy data may need reinterpretation.

## 2.2 Introduction

The Atlantic Meridional Overturning Circulation (AMOC) is a part of the climate system, important for understanding the dynamics of the ocean in a past scenario such as the Last Glacial Maximum (LGM, 26-19 kyr before present (Clark et al., 2009)). It is an indicator of the transport and ventilation rates of the deep ocean, and plays an important role in biogeochemical cycles and the climate of north-western Europe. It is thought to be driven by a variety of processes, such as wind stress, buoyancy fluxes and mixing (Kuhlbrodt et al., 2007). The AMOC can be described by using the meridional streamfunction $\psi(y, z)$, which is the zonally- and depth-integrated meridional velocity in the Atlantic Ocean and has units of volume transport, usually reported in Sverdrups (1 Sv $= 10^6 m^3/s$).

Reconstructions from sediment cores indicate differences between the modern and LGM AMOC. Benthic foraminifera $\delta^{18}$O data suggest a weaker transport of the Gulf Stream (Lynch-Stieglitz et al., 1999) that would make for a weaker AMOC

than today's. Some $^{231}Pa/^{230}Th$ records in the Atlantic basin (McManus et al., 2004) have been interpreted as a weaker AMOC during the LGM, while other studies (e.g. Gherardi et al., 2009) suggest a stronger and shallower circulation. The distribution of $\delta^{13}C$ reconstructed from benthic foraminifera, implies a similar AMOC but shallower North Atlantic Deep Water (NADW) (Gebbie, 2014). Pore water measurements in sediments show that bottom water temperatures were close to freezing point, and that Antarctic Bottom Water (AABW) had higher salinity than NADW (Adkins et al., 2002).

The Paleoclimate Model Intercomparison Project Phase 3 (PMIP3), a joint effort of different coupled ocean-atmosphere general circulation models to simulate the LGM (Braconnot et al., 2012), provides an opportunity to test models that are used for climate projections (Stocker et al., 2013). The PMIP3 experimental design uses prescribed LGM values for orbital parameters, trace gases and ice sheets. Sea level drop is considered in the land-sea masks and background salinities of all models, and bathymetry changes in some of them. Ocean currents, temperature, salinity and other variables are calculated by the models.

The previous version of PMIP (PMIP2) showed dissimilar results between the simulated ocean state of the LGM. Some models predicted a slower and shallower AMOC, while others predicted it as deeper and stronger (Otto-Bliesner et al., 2007). At the same time, relative changes in temperature and salinity between AABW and NADW were different among models. Weber et al. (2007) suggest that the density difference between AABW and NADW controls the AMOC in PMIP2 models, but they did not consider changes in wind stress.

Here we study the AMOC as simulated by PMIP3 models, in their pre-industrial control (PI) and LGM ensembles. We compare simulations to observations, study the changes between the periods and try to understand which processes control these changes in the models.

Coupled ocean-atmospheric models show that a higher ice sheet over North America results in a stronger AMOC (Ullman et al., 2014; Zhang et al., 2014). However, the precise process governing this response, which may be changes in atmospheric circulation, hydrological cycle and buoyancy fluxes, or wind stress, remains unknown.

Among the drivers of the AMOC, wind stress $\tau = (\tau_x, \tau_y)$ plays an important role. It affects the strength of surface currents (e.g. the Gulf Stream), the meridional salt transport and the upwelling of deep waters in the southern hemisphere, which have been suggested to impact the AMOC (Toggweiler and Samuels, 1995). From ocean models, Montoya and Levermann (2008), Oka et al. (2012) and Wunsch (2003) have suggested that stronger LGM winds could have increased the AMOC. Here we quantify wind stress effects on the AMOC, and its role in the LGM circulation of the PMIP3 models.

## 2.3 Materials and Methods

Values of 50 y time-averaged Atlantic meridional streamfunction $\psi(y, z)$ were obtained from eight PMIP3 models. To quantify the effect of wind stress on the AMOC, we conducted sensitivity experiments with the UVic Earth System Climate

Model version 2.9 (Weaver et al., 2001). This model includes a three-dimensional dynamical ocean with 19 vertical levels at $3.6° \times 1.8°$ horizontal resolution governed by the primitive equations, coupled to a two-dimensional single-level atmosphere, with moisture and heat balances and fluxes between the two mediums, and a dynamical sea ice model. Wind stress, wind used in moisture advection and air-sea fluxes as well as clouds are prescribed from a present day monthly climatology. Diapycnal mixing is calculated with a three dimensional parametrization that simulates tide effects (Schmittner and Egbert, 2013).

For the sensitivity experiments, we calculated LGM anomalies (LGM minus PI) of wind stress from the output of the PMIP3 models (Fig. A.1). The LGM anomalies were added to present day fields from the NCEP reanalysis (Kalnay et al., 1996), and used as surface momentum forcing of the ocean and sea ice in the UVic Model. We preformed a different run for each PMIP3 model. Results are compared to a default run with no anomalies added. We also performed experiments with anomalies from four PMIP2 models for which pertinent output was available.

Atmospheric $CO_2$ was set to 185 ppm, with orbital parameters corresponding to 21 kyr. Average salinities were not adjusted for lower than present sea level. We do not a focus here on the effects of a globally uniform increase in salinity.

We used continental ice sheet height and fraction from two different reconstructions: ICE-4G (Peltier, 1994) and the ice sheet that PMIP3 models use, which is a blend of three other reconstructions (Abe-Ouchi et al., 2015). For the experiments with PMIP2 wind stress anomalies, we used ICE-5G (Peltier, 2004), used in that

version of the intercomparison project (Braconnot et al., 2007). In Fig. A.2 we show the ice thickness and fraction of all the ice reconstructions, re-gridded to our model's grid.

A modern distribution of river basins was used. Changing the river routing in North America to account for the Laurentide Ice Sheet did not produce significant changes in the ocean circulation (Fig. A.3).

For each case, the UVic model was run for 2000 years. Results from the last 500 years are presented.

## 2.4 Results

### 2.4.1 AMOC as simulated by PMIP3 models

In Fig. 2.1 (top panels), the upper cell of the AMOC (to which we will simply refer as AMOC) can be distinguished as the zone with positive values of $\psi$ in the upper $\sim$ 2500 m of the water column, spanning from $\sim 30^\circ$ S to $\sim 60^\circ$ N.

The multi-model average PI AMOC value at $25^\circ$ N is $16.48 \pm 3.67$ Sv, with uncertainties defined as the $1\sigma$ standard deviation among models. This number is in agreement with modern measurement-based estimates of 17.2 Sv (McCarthy et al., 2015). Inflow of Circumpolar Deep Water (CPDW) into the Indo-Pacific (IP) is generally lower ($8.6 \pm 3.6$ Sv at $32^\circ$ S) than modern observations of 14.9 Sv (McCarthy et al., 2015). This suggests that AABW formation mechanisms are not correctly represented by the models and/or that diapycnal mixing or geothermal

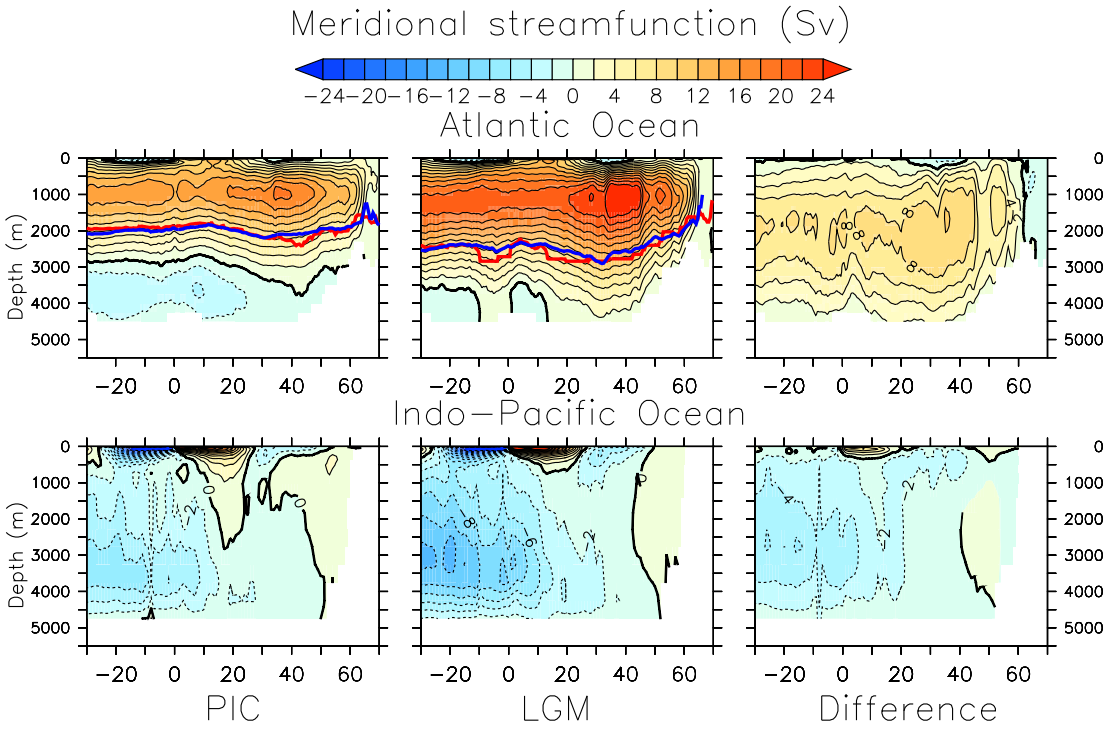


Figure 2.1: Multi-model mean of Atlantic and Indo-Pacific meridional streamfunction $\psi(y, z)$ calculated by PMIP3 models. Abscissa axes are in ° N. First column corresponds to PI simulations, middle corresponds to LGM simulations, and third to the difference. Isoline difference is 2 Sv. In the Atlantic plots, the red line is the depth of the AMOC calculated as the middle depth between $\psi = \psi_{max}$ and $\psi = 0$, and the blue line is the depth where $\psi = \psi_{max}/2$. Positive (negative) values correspond to clockwise (anti-clockwise) circulation.

Table 2.1: Maximum transport and depth of the AMOC at 25° N calculated by PMIP3 models, in their PI and LGM simulations, and percentage of increment between the two periods. Bottom row is the multi-model mean.

| Model | PI/LGM AMOC (Sv) | Change (%) | PI/LGM depth (m) | Change (%) |
|---|---|---|---|---|
| CCSM4 | 19.69/21.53 | 09 | 2608/2333 | -10 |
| GISS | 16.92/22.32 | 32 | 2055/2273 | 11 |
| CNRM | 13.03/22.74 | 74 | 1735/3230 | 86 |
| MPI | 18.19/21.37 | 17 | 1963/1993 | 01 |
| MIROC | 13.56/22.07 | 63 | 1795/2745 | 53 |
| MRI | 14.82/21.76 | 47 | 2193/3363 | 53 |
| FGOALS | 23.02/31.64 | 37 | 1965/2940 | 50 |
| IPSL | 12.64/23.04 | 82 | 2238/2980 | 78 |
| Mean | 16.48/23.31 | 41 | 2069/2732 | 32 |

heat fluxes are underestimated in the abyssal IP.

PMIP3 models show stronger AMOC transport during the LGM (see Fig. 2.1 for the multi-model mean, Figs. A.4, A.5 for each individual model). In most models, the upper clockwise cell reaches deeper in the LGM simulations, suggesting a deeper NADW. CCSM4 shows a shallowing of NADW and increased penetration of AABW in the North Atlantic (NA).

In CCSM4 and GISS the AABW cell is intensified, MPI shows little change, whereas in the five other models the deepening of the NADW cell weakens AABW and pushes it south. Inflow of CPDW into the IP increases by $\sim 5$ Sv (Figs. 2.1, A.6), suggesting that the enhanced NADW flow into the Southern Ocean (SO) contributes to more CPDW flow into the IP.

The LGM multi-model mean of maximum transport of the AMOC at 25° N is $23 \pm 3$ Sv, a $(41 \pm 26)\%$ average increase when compared to PI (Table 2.1).

This strengthening is in contrast with reconstructions of a weaker LGM AMOC (Lynch-Stieglitz et al., 2007; McManus et al., 2004). It is in closer agreement with reconstructions that indicate a stronger AMOC, like Lippold et al. (2012) or Gherardi et al. (2009), although the latter suggests a shallower AMOC.

The NADW depth was estimated in two ways: As the depth at which $\psi$ was one-half of its maximum value, and as the middle depth between the maximum $\psi$ and $\psi = 0$ isolines. Both estimates give similar values (Fig. 2.1). We obtained, on average, 2069 m for the PI and 2732 m for the LGM (32% of increment, Table 2.1). This contrasts with estimates of an LGM NADW between 0 and 1000 m shallower, based on an inverse model solution using carbon and oxygen isotope reconstructions from LGM sediments (Gebbie, 2014).

Concerning bottom temperatures and salinity, PMIP3 PI simulations are in fair agreement with observations (Fig. 2.2). However, LGM simulations are in disagreement with reconstructions from sediment pore water estimates (Adkins et al., 2002). NA bottom waters are too warm, whereas SO and South Pacific are too fresh in the models. None of the models predict saltier AABW than NADW, or bottom water potential temperatures below $-1\,^{\circ}\mathrm{C}$. This is in contrast to PMIP2, where two models (CCSM3 and HADCM3) showed results more in line with Adkins' estimates.

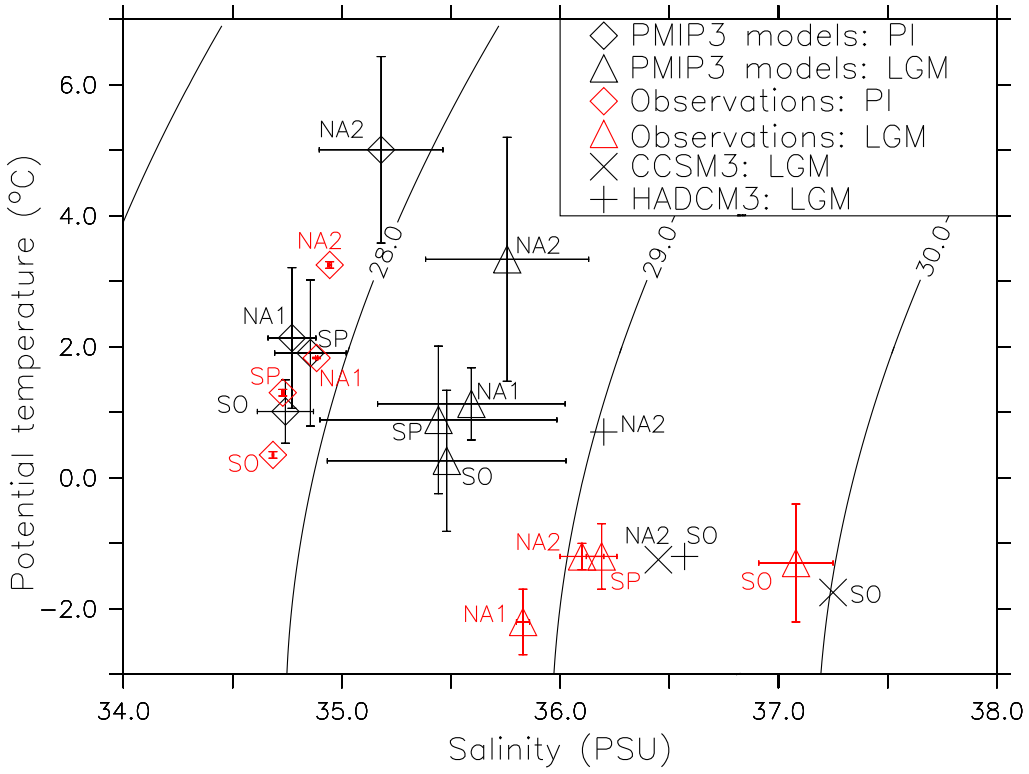


Figure 2.2: Bottom potential temperature-salinity diagram for the PMIP3 multi-model average (in PI and LGM simulations), modern observations and LGM reconstructions from Adkins et al. (2002) for two sites in the North Atlantic, one in the South Pacific and one in the Southern Ocean (Atlantic sector). Also included are two LGM PMIP2 models that showed similarities with reconstructions, taken from Otto-Bliesner et al. (2007). Error bars in the multi-model averages are $1\sigma$ standard deviations. Contours are potential density in kg/m$^3$.

### 2.4.2 Sensitivity experiments with the UVic Model

In the default LGM case with modern winds and PMIP3 ice sheets (Fig. 2.3, top panel), UVic model's AMOC is weaker (9.10 Sv at 25° N) and shallower (1900 m if calculated by the method used in the previous section) than in the preindustrial case (15.78 Sv, 2030 m, Fig. A.7). Since the wind stress is identical in both LGM and PI cases, we deduce that this response is caused by changes in surface buoyancy forcing.

An LGM simulation with modern winds and ICE-4G ice sheets produces a collapsed AMOC. When PMIP3 LGM wind stress anomalies are applied, the AMOC increases for all model cases, producing stable solutions with a transport of $(14.82 \pm 1.59)$ Sv at 25° N (Fig. 2.3). This type of behavior of climate models has been previously documented by Oka et al. (2012).

When using PMIP3 LGM wind stress anomalies and continental ice sheets, the average AMOC at 25° N is $(12.67 \pm 1.10)$ Sv (Table 2.2; Figs. 2.3, A.8 and A.9). This is $(39 \pm 11)$% stronger than the default case with the same ice sheets. Average depth of the AMOC at 25° N is 3000 m. This represents an increment of approximately 54% with respect to the default run. Inflow of CDW is intensified by $\sim 1$ Sv in the IP, whereas AABW flow into the Atlantic is weakened. These changes are consistent, at least qualitatively, with the response of the PMIP3 models to LGM boundary conditions.

For the PMIP2 experiments (Fig. A.10, Table A.1), we find an increment in the AMOC in three cases (CCSM3, MIROC and FGOALS), but no change in one

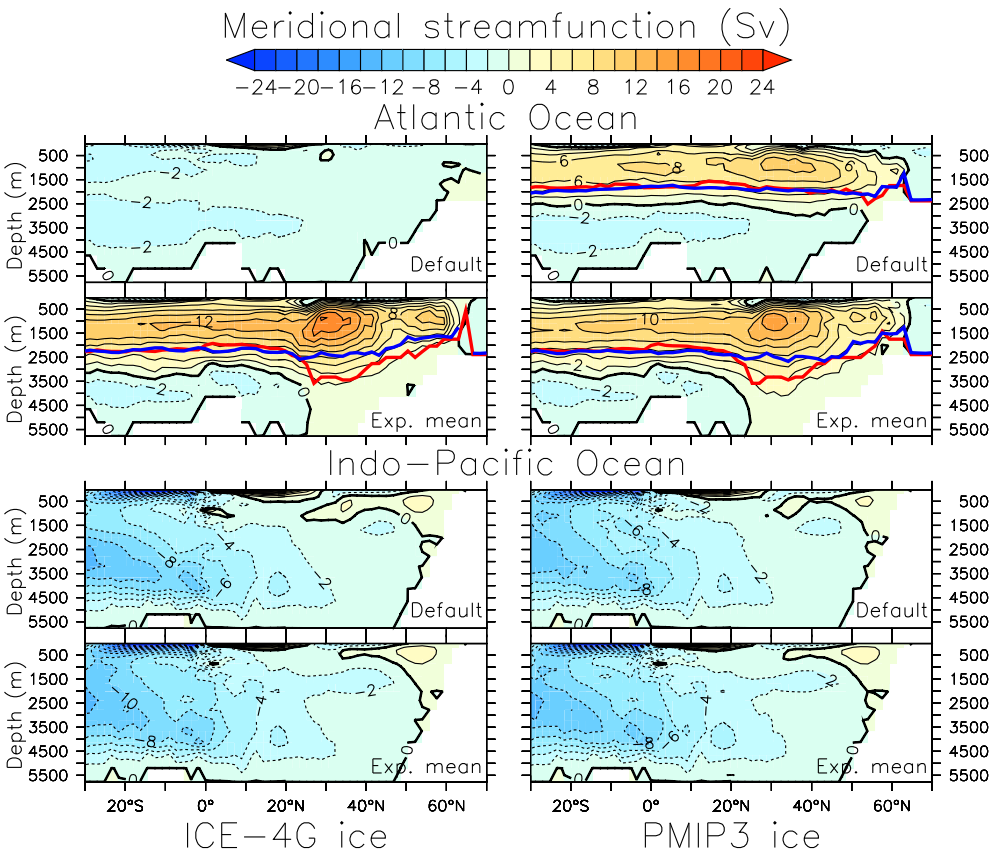


Figure 2.3: LGM meridional streamfunction calculated by UVic. Left (right) column corresponds to runs using the ICE-4G (PMIP3) LGM land ice reconstruction. Default cases use present-day wind stress obtained from NCEP reanalysis. The experiment mean is the average between runs where PMIP3 LGM anomalies are added to NCEP wind stress. Red and blue lines as in Fig. 2.1. Note that the AMOC collapses in the default ICE-4G case.

Table 2.2: Maximum meridional overturning, percentage of increment between wind stress experiments and default run, salt flux $F_{salt}$ in the Atlantic Ocean and depth of the AMOC (all at 25° N) in the UVic model experiments. Each row corresponds to wind stress anomalies from a different PMIP3 model. The top row corresponds to the default case. All numbers correspond to experiments using the PMIP3 ice sheet.

| Model case | AMOC (Sv) | Change (%) | $F_{salt}$ ($10^6$ kg/s) | Depth (m) | Change (%) |
|---|---|---|---|---|---|
| Default | 9.10 | - | 89.23 | 1905 | - |
| CCSM4 | 13.56 | 49 | 99.32 | 3103 | 63 |
| GISS | 11.07 | 22 | 108.60 | 2203 | 16 |
| CNRM | 11.15 | 22 | 106.10 | 3300 | 73 |
| MPI | 12.13 | 33 | 102.70 | 3080 | 62 |
| MIROC | 13.33 | 46 | 98.78 | 3060 | 61 |
| MRI | 13.55 | 49 | 101.00 | 3068 | 61 |
| FGOALS | 13.84 | 52 | 97.77 | 3048 | 60 |
| IPSL | 12.78 | 40 | 96.60 | 3123 | 64 |

case (CNRM). CNRM exhibits smaller changes in wind stress over the NA than the other models, which could be the reason behind the discrepant result.

## 2.5 Discussion

PMIP3 models predict a strengthening and deepening of the AMOC in the LGM. The UVic Model produces a similar result, when forced with LGM wind stress anomalies calculated by the same models.

The zonal component of the PMIP3 wind stress anomaly fields exhibits a conspicuous maximum in the NA region (Fig. A.1). This is an effect of the Laurentide Ice Sheet over North America, which produces stronger and southward-shifted

westerly winds over the NA.

We hypothesize that the increment in the AMOC strength is controlled by stronger westerly winds over the North Atlantic, which increase the northward salt transport. Resulting higher salinities increase the density of surface waters and intensify deep water formation at high latitudes. This hypothesis is confirmed by analysis of the meridional salt flux $F_{salt}$ at 25° N in the Atlantic, defined as

$$F_{salt} = \int_{25^\circ N}^{90^\circ N} \int_{x_1(y)}^{x_2(y)} (P + R - E)\, dxdy, \tag{2.1}$$

where $E$ is evaporation, $P$ is precipitation, and $R$ is river discharge (expressed in kg/(m$^2$s)). Table 2.2 shows that values of $F_{salt}$ are positive at 25° N, indicating a northward salt transport across that latitude. The magnitude in the default simulation is smaller than the ones obtained with any of the PMIP3 wind stress anomalies. There is more salty water being transported northward in the cases with higher wind stress over the NA.

To further test our hypothesis of a NA-driven strengthening of the AMOC in the PMIP3 models, we performed simulations with a multi-model average of the wind stress anomalies, in which we applied the LGM wind stress anomaly only in one hemisphere (Fig. A.11, left column). We label $\Delta\tau_{SH}$ ($\Delta\tau_{NH}$) the case in which it was applied in the Southern (Northern) Hemisphere. We also performed a simulation using the average anomaly in both hemispheres, referred to as full case.

The AMOC in the default case (Fig. A.11(a)) is similar (in values and struc-

ture) to that of $\Delta\tau_{SH}$ (b), while the AMOC in the full case (d) is similar to that of $\Delta\tau_{NH}$ (c), indicating that the differences in the AMOC between PI and LGM simulations is a response to wind stress anomalies in the Northern Hemisphere.

When using LGM wind stress anomalies from the PMIP2 models, the resulting UVic simulated AMOC has in some cases a different sign of change compared to the AMOC from the PMIP2 models (see Otto-Bliesner et al., 2007, for AMOC plots of different PMIP2 models, and compare to Fig. A.10 of this work). This suggests that changes in buoyancy forcing are more important in these models. For example, the CCSM3 model used in Otto-Bliesner et al. (2007) predicts a weakening of the AMOC in the LGM, even though the transport of the Gulf Stream increases due to wind effects, indicating that changes in buoyancy fluxes decrease the AMOC and dominate wind stress effects. The strong effect of buoyancy in these models is also demonstrated in their bottom salinity values, with a salty SO water, indicating high production of AABW (Fig. 2.2).

Our results are consistent with results from ocean-atmosphere models, which show a stronger AMOC as a response to increases in ice sheet height (Otto-Bliesner et al., 2006; Ullman et al., 2014; Zhang et al., 2014). Our simulations suggest that enhanced wind driven salt transport may, at least partly, explain this response.

Because of the similarity between PMIP3 models' outputs and our wind stress experiments with the UVic model, our results suggest that in the PMIP3 case, wind stress plays a fundamental part in the LGM-PIC AMOC differences, and that changes in buoyancy fluxes play a smaller role. This is in contrast to the response in CCSM3 and UVic model, where changes in buoyancy fluxes, which

tend to decrease the AMOC (Fig. B.1.6), are similar but slightly larger than the effects of the PMIP3 wind stress (Fig. 2.3).

## 2.6 Conclusions

UVic Model responds very consistently with a strengthening and deepening of the AMOC when forced with LGM wind stress anomalies from PMIP models. Our analysis suggests that stronger wind stress over the NA due to the effects of the Laurentide Ice Sheet on atmospheric circulation causes enhanced northward salt transport in an intensified gyre circulation. This is an important process explaining the LGM-PIC differences predicted by these models. The result represents an improvement in our understanding of the mechanics governing the LGM AMOC in climate models. The fact that the results are robust across all models examined suggests that this process may also play an important role in the real world, confirming the speculation by Wunsch (2003).

It will be an important task for future work to resolve the apparent inconsistency between PMIP models' LGM circulation and reconstructions. This inconsistency casts doubt on future AMOC projections with these models (e.g. Weaver et al., 2012). One possible explanation may be that not all PMIP3 models were in equilibrium (Zhang et al., 2013).

Since LGM wind stress, closure of Bering Strait (Hu et al., 2010), and increased tidal mixing (Schmittner et al., 2015) all tend to increase the strength and depth of the AMOC, a countering effect has to be invoked to reproduce observations of

a weaker and shallower overturning during the LGM.

Changes in buoyancy fluxes, as suggested by CCSM3 and the UVic model are a good candidate. A detailed analysis of the PMIP3 models' buoyancy fluxes and their effects on the AMOC remains to be performed. Ferrari et al. (2014) have recently hypothesized that the expansion of Antarctic sea ice explains the shoaling of the AMOC. However, since the PMIP models do simulate more extensive sea ice, this process appears to be not very important in these models. We conclude that the specific mechanism for the required buoyancy flux changes remains elusive.

Finally, due to the high consistency between model results, we do not rule out the possibility that some proxies may need reinterpretation. To study the implications of the modelled LGM circulation on isotope distributions will be useful for a more direct comparison.

# Chapter 3: Combined effects of atmospheric and seafloor iron fluxes to the glacial ocean

Juan Muglia[1], Christopher J. Somes[2], Levin Nickelsen[2], and Andreas Schmittner[1]

[1]College of Earth, Ocean and Atmospheric Sciences, Oregon State University, Corvallis, USA

[2]GEOMAR Helmholtz Centre for Ocean Research Kiel, Kiel, Germany

## 3.1 Abstract

Changes in the ocean iron cycle could help explain the low atmospheric $CO_2$ during the Last Glacial Maximum (LGM). Previous modeling studies have mostly considered changes in aeolian iron fluxes, although it is known that sedimentary and hydrothermal fluxes are important iron sources for today's ocean. Here we evaluate effects of preindustrial-to-LGM changes in atmospheric dust, sedimentary, and hydrothermal fluxes on the ocean's iron and carbon cycles in a global coupled biogeochemical circulation model. Considering variable atmospheric iron

solubility decreases LGM soluble iron fluxes compared with assuming constant solubility, which limits potential increases in productivity and an enhanced biological pump, thereby sequestering enough carbon in deep waters to lower $CO_2$ by only 4 ppm. The effect is strongly countered by a decrease in sedimentary flux due to lower sea level, which increases $CO_2$ by 15 ppm. In an upper-limit estimation of Southern Ocean surface iron fertilization, assuming a 10 times higher solubility for this region, combined with changes in sedimentary flux, we obtain an atmospheric $CO_2$ reduction of 13 ppm. A five-fold increase in hydrothermal sources of iron decreases atmospheric $CO_2$ by an additional 6 ppm. Our model does not account for changes to iron-binding ligand concentrations that could modify the results. We conclude that when evaluating glacial-interglacial changes in the ocean iron cycle, not only surface but also seafloor fluxes must be taken into account.

## 3.2 Introduction

During the Last Glacial Maximum (LGM, $\sim$ 21 kyears before present) the concentration of atmospheric $CO_2$ was about 100 ppm lower than its pre-industrial (PI) value (Marcott et al., 2014). It has been suggested that changes in the ocean circulation and biogeochemistry, as well as sea ice cover, could be responsible for this difference (Sigman and Boyle, 2000).

An increase in biological production and export of organic matter could have transferred $CO_2$ from the atmosphere to deep waters in the LGM. Martin (1990) hypothesized that higher surface iron concentrations in the Southern Ocean (SO)

could have intensified this region's primary productivity, playing an important role in the sequestration of atmospheric carbon. In the present, most of the surface SO has high levels of nutrient species nitrate ($NO_3$) and phosphate ($PO_4$) (Levitus et al., 2013), but low concentrations of dissolved iron (DFe), resulting in low primary productivity and the largest high nutrient low chlorophyll (HNLC) region in the global ocean.

DFe surface concentrations in regions far away from continents depend largely on dust sources (Jickells et al., 2005). Observations and models indicate that LGM atmospheric dust fluxes to the east of Patagonia and into the SO were orders of magnitude higher than in PI times (Lambert et al., 2015; Albani et al., 2014; Maher et al., 2010). Measurements of soluble iron content in LGM dust of Antarctic ice cores also indicate a much higher input than in modern times (Conway et al., 2015). Along with higher dust flux, $^{15}N/^{14}N$ ratios from planktonic foraminifera in sediment cores of the SO have been interpreted as higher productivity and more efficient nutrient utilization in the LGM compared to the PI (Martínez-García et al., 2014). Meanwhile, Middleton et al. (2016); Lund et al. (2016) proposed that hydrothermal flux may have been higher during the LGM due to lower water column pressure on hydrothermal vents, adding a new possible source for iron fertilization.

Numerous modeling efforts have studied effects of iron fertilization on the LGM carbon cycle. SO experiments in a one-dimensional (vertical) ecological model with increased iron concentrations produce a doubling in export production (Fennel et al., 2003; Mongin et al., 2007). Three dimensional global ocean models have

shown increased export production and atmospheric $CO_2$ drawdown when applying LGM atmospheric dust fluxes: Bopp et al. (2003) reported an atmospheric $CO_2$ decrease of up to 30 ppm. Brovkin et al. (2007) obtained a higher number 35 ppm, but their model lacks an iron cycle and they assumed full $PO_4$ utilization in the Atlantic and Indian sectors of the SO instead. Models that use more realistic interactive iron cycles predict a weaker effect, lower than 15 ppm (Lambert et al., 2015; Tagliabue et al., 2009; Parekh et al., 2008). These models include a representation of iron-binding ligands, which buffer effects of changes in external sources on DFe concentrations (Parekh et al., 2004).

Most modeling studies that have simulated the LGM iron cycle have focused on atmospheric flux changes. They have assumed constant iron solubility in dust, which could result in overestimations of glacial soluble iron fertilization, since dust concentrations are thought to be inversely proportional to iron solubility (Sholkovitz et al., 2012; Luo et al., 2008). Sedimentary and hydrothermal iron fluxes have also been proven to affect DFe concentrations in the modern ocean and could drive changes in atmospheric $CO_2$ (Tagliabue et al., 2010).

Here we study the response of the ocean's coupled iron-biogeochemical system to changes in external iron fluxes from different LGM estimates and possible impacts on the carbon cycle. We use a three dimensional global circulation model, coupled with a biogeochemical model that includes a prognostic iron cycle. Changes in the iron inputs to the ocean include dust deposition considering variable iron solubility, sedimentary release and hydrothermal flux. Our knowledge of these fluxes has high levels of uncertainty: Atmospheric flux depends on the solu-

bility of iron in dust (Sholkovitz et al., 2012), sedimentary release measurements are limited to a few locations at continental shelves (Elrod et al., 2004), and hydrothermal fluxes are parametrized from $^3$He fluxes (Tagliabue et al., 2010). This makes past estimates even more uncertain, although the direction of changes from modern values can be estimated.

## 3.3 Methods

### 3.3.1 Physical model

We use the global ocean circulation model from the University of Victoria (UVic) (Weaver et al., 2001), version 2.9. It consists on a three-dimensional dynamical ocean with 19 vertical levels at $3.6^\circ \times 1.8^\circ$ horizontal resolution governed by the primitive equations, coupled to a two-dimensional single-level atmosphere, with moisture and heat balances and fluxes between the two mediums, and a dynamical sea ice model. It is coupled to a dynamic land vegetation model (Meissner et al., 2003). Winds and clouds are prescribed from present-day monthly climatologies (Kalnay et al., 1996). Background vertical diffusivity was set to $3.5 \times 10^{-5}$ m$^2$/s. Our diapycnal mixing scheme includes a three-dimensional parametrization of tide effects (Schmittner and Egbert, 2013). Isopycnal eddy diffusivity was set to $1.2 \times 10^3$ m$^2$/s. Higher values are applied in the tropics, as recommended by Getzlaff and Dietze (2013).

LGM runs use an atmospheric $CO_2$ value of 185 ppm, and orbital parameters

from 21 kyr. For continental ice sheets, we use the reconstruction from the Paleoclimate Model Intercomparison Project Phase 3 (PMIP3) set up (Abe-Ouchi et al., 2015). We apply a global 1 PSU addition to salinity to account for sea level drop. A multi-model mean of LGM-PI wind stress anomalies from PMIP3 models was added to the PI wind stress fields. We use PI river routings.

Our model's circulation with this LGM configuration is described in Muglia and Schmittner (2015). It has a strong, deep upper cell of the Atlantic Meridional Overturning Circulation (AMOC), similar to most PMIP3 models. This type of circulation is a result of strong wind stress on the North Atlantic, which strengthens surface northward salt transport, increasing North Atlantic Deep Water (NADW) production.

### 3.3.2 Model of Ocean Biogeochemistry

UVic is coupled with the Model of Ocean Biogeochemistry and Isotopes (MOBI), version 1.8, based on Somes and Oschlies (2015), with the implementation of an interactive iron cycle from Nickelsen et al. (2015). It includes prognostic equations for $PO_4$, $NO_3$, DFe, $O_2$, DIC, dissolved organic matter (DOM), particulate organic matter (detritus), PFe, phytoplankton, zooplankton and diazotrophs (Fig. 3.1). It is embedded within the circulation model, so tracers depend on ocean physics as well as biogeochemical interactions. The phosphorous content of the ocean is assumed constant, but the N cycle includes $N_2$ fixation by diazotrophs (source of $NO_3$), and water column and benthic denitrification (sinks of $NO_3$).

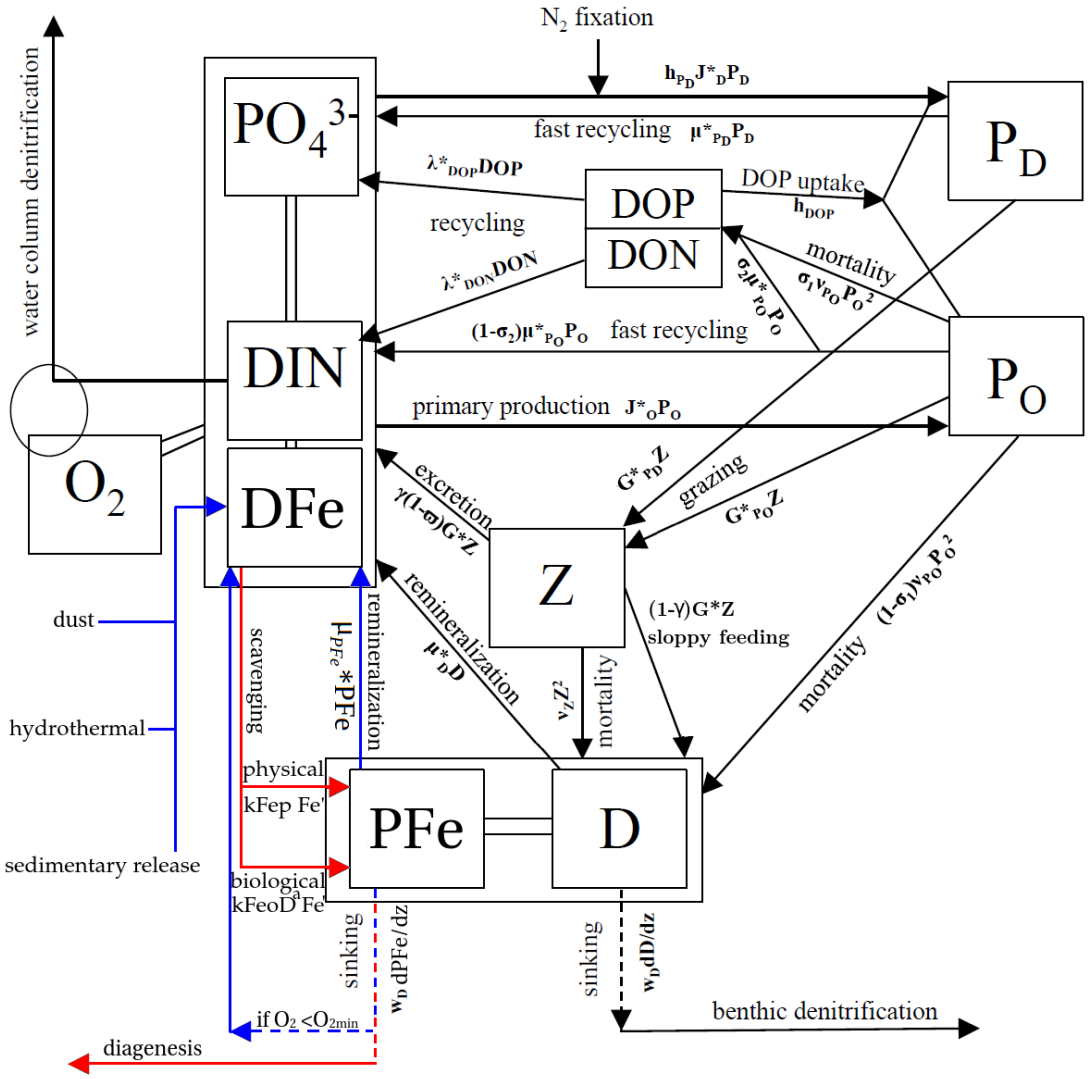


Figure 3.1: Diagram of our NPZD model. DFe sinks (sources) are highlighted in red (blue).

The iron cycle includes external inputs from atmospheric dust, sedimentary, and hydrothermal fluxes. Atmospheric deposition is calculated from a prescribed dust flux climatology and added to DFe at the surface. Sedimentary release is proportional to the flux of organic matter reaching the ocean floor. Bulk hydrothermal iron fluxes at mid-ocean ridges were obtained from Tagliabue et al. (2014), regridded to the UVic's grid and multiplied by a factor to preserve the globally integrated flux of the original reconstruction. They are added locally to DFe concentrations at the corresponding grid boxes.

DFe can be scavenged to PFe in the water column, and be exported to the sediments where it is either lost, or re-released if the environment is reducing. A step function of $O_2$ with limit at $O_2 = 5\,\mu$M controls the latter process. Biological and physical scavenging are represented, and depend on a constant iron-binding ligand concentration. Scavenging is proportional to unbound iron. Because ligands reduce unbound iron concentrations, scavenging is lower with higher ligand concentrations. The global constant ligand concentration is 1.5 $\mu$mol/m$^3$, in line with recent simulations with a model that includes ligands as an interactive variable (Völker and Tagliabue, 2015).

Biological and inorganic scavenging rates have been increased from 0.45 (m$^3$/(gC d))$^{0.58}$ and 0.005 d$^{-1}$ in Nickelsen et al. (2015) to 1.0 (m$^3$/(gC d))$^{0.58}$ and 0.016 d$^{-1}$, respectively, to equilibrate at observed iron concentrations due to the addition of hydrothermal flux to the model. The iron maximum half saturation constant for phytoplankton growth has been decreased, from 0.4 $\mu$mol Fe/m$^3$ in Nickelsen et al. (2015) to 0.2 $\mu$mol Fe/m$^3$, to better represent surface SO $PO_4$ and $NO_3$

concentrations. All other biogeochemical parameters have been kept as in Nickelsen et al. (2015) (for iron variables) and Somes and Oschlies (2015) (for other biogeochemical variables).

Due to the scarcity and variability of observations (Tagliabue et al., 2012), the dynamism of its fluxes (Tagliabue et al., 2014), and the complex interactions among its components, current model representations of the iron cycle, including this one, have high uncertainties and biases (Tagliabue et al., 2016). Although our model includes a constant parameter to represent iron-binding ligands, an interactive cycle could be a more realistic approach. However, the high complexity of ligand chemistry and distributions, with different species in different sectors of the ocean (Gledhill and Buck, 2012), could bring additional uncertainties to our LGM estimates. Here we focus on direct effects of changes in the iron fluxes, without mediation of ligand concentrations.

### 3.3.3 Iron from dust flux

PI and LGM surface soluble iron fluxes were generated from dust flux monthly climatologies calculated by Lambert et al. (2015), who interpolated observations from these two time periods. We assume a 3.5 % iron content in dust (Mahowald et al., 2009).

Luo et al. (2008) used an atmospheric model to generate fields of modern dust flux, soluble iron flux and solubility of iron in dust. They predicted higher solubility with lower dust concentration. To calculate iron solubility for our dust fields, we

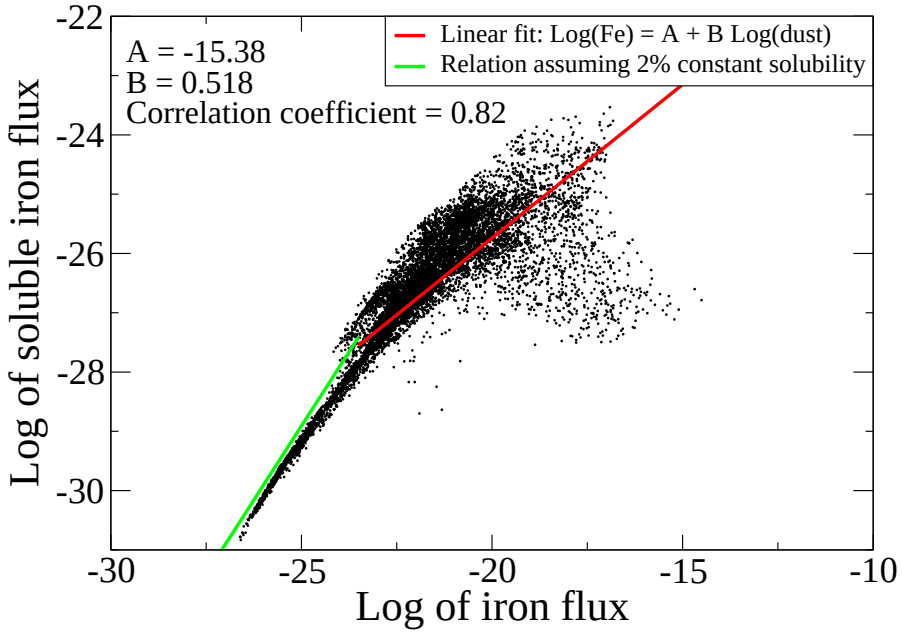


Figure 3.2: Plot of logarithm of atmospheric iron flux vs logarithm of soluble iron flux in gFe/($m^2$s) units, calculated by an atmospheric model (Luo et al., 2008). The functional form between the two variables represents iron solubility. High values of iron flux are fitted by a power law (red line). For low values we use a constant 2% solubility (green line).

created a scatter plot of soluble iron versus iron in dust from Luo et al. (2008), and fitted a curve to it (Fig. 3.2). A constant 2 % (as assumed in Lambert et al. (2015)) solubility provides a good fit for low dust concentrations, but a power law is more accurate at higher values. Our solubility fit is a piecewise function of these two curves, and it was applied to dust fluxes from Lambert et al. (2015), transforming them into monthly climatologies of soluble iron flux. Solubilities range between 0.02 % and 2.0 %, with PI and LGM global means of 0.8 % and 0.4 %, respectively. Due to the lower solubility, surface iron flux must be more than twice its PI value in order to have glacial iron fertilization. Dust deposited above sea ice cannot reach surface waters, so in grid boxes with sea ice fraction we decreased iron flux by a percentage equal to that fraction. Iron is accumulated in these ice covered grid boxes, and released when sea ice melts.

Our estimated LGM surface soluble iron fluxes are higher than PI in parts of the SO, to the east of the Patagonian region and around continents (Fig. 3). Modern measurements of atmospheric dust concentrations and solubility have high uncertainties (Winton et al., 2016; Sholkovitz et al., 2012), so the real LGM surface soluble iron fluxes may have been very different from what we estimate. In order to consider this uncertainty we perform an additional sensitivity experiment where LGM soluble flux is multiplied by 10 south of 35° S. We consider this an upper end estimation, but in line with measurements of Antarctic ice cores, where LGM soluble iron fluxes were found to be of the order of $\geq 10$ times larger than PI values (Conway et al., 2015).

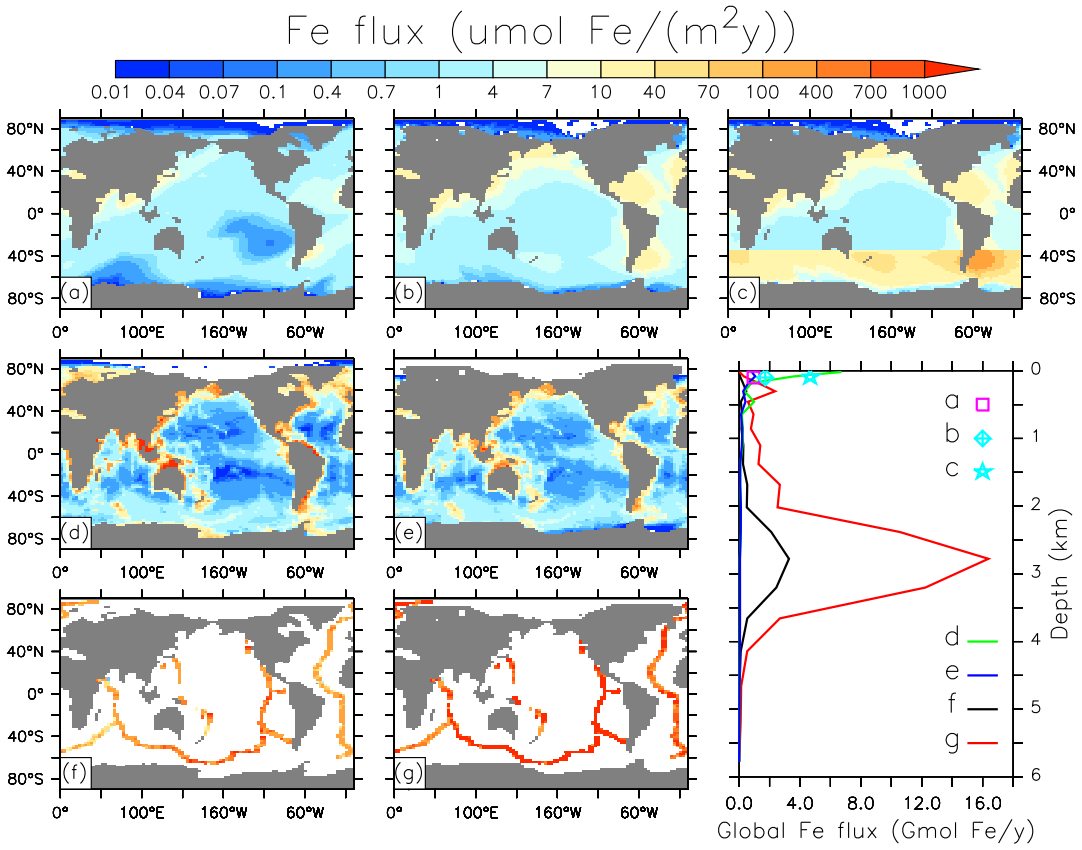


Figure 3.3: Soluble iron fluxes used in the model. Top surface maps are surface atmospheric fluxes corresponding to (a) PI, (b) LGM, and (c) LGM with 10× deposition in the SO. Middle surface maps are sedimentary fluxes for (d) PI, and (e) LGM (LGM_Fe simulation). Bottom maps are hydrothermal fluxes, corresponding to (f) PI, and (g) 5×PI. The color scale is logarithmic. The depth profile plot shows the same fluxes, as indicated by the letter codes, integrated horizontally and over the thickness of each of the model's vertical levels. Atmospheric fluxes only have values at the surface.

### 3.3.4 Iron from sedimentary release

Sedimentary DFe release is proportional to the flux of organic carbon reaching the bottom of the ocean, with an exponential temperature dependence, to account for temperature-dependent remineralization (Nickelsen et al., 2015). In the real ocean this process is especially relevant over continental shelves (Elrod et al., 2004), but UVic's coarse resolution bathymetry is not able to resolve shallow bottom features. Therefore we use a sub-grid bathymetry function that specifies the fraction of ocean bottom at each ocean grid box, and is multiplied to the sedimentary release. For each grid box at position $i, j, k$, the sub-grid bathymetry parameter $sgb(i, j, k)$ is defined as

$$sgb(i,j,k) = \begin{cases} f(i,j,k) & \text{if } k = 1 \text{ (surface)} \\ \\ \frac{f(i,j,k)}{1-\sum_{n=1}^{k-1} f(i,j,n)} & \text{otherwise,} \end{cases} \tag{3.1}$$

where $f(i, j, k)$ is the fraction (from 0 to 1) of ocean bottom at each grid box. Fractions were calculated using the ETOPO 2-minute resolution bathymetry (National Geophysical Data Center, 2006).

Vertical fluxes such as exported detritus are modified by $sgb(i, j, k)$. At each grid box, imported detritus is remineralized into $PO_4$ and $NO_3$ in a fraction equal to $sgb(i, j, k)$. Benthic denitrification is also proportional to $sgb(i, j, k)$ (Somes and Oschlies, 2015). $sgb(i, j, k)$ is defined so that no vertical fluxes penetrate the sub-grid defined ocean bottom, and no benthic denitrification or DFe sedimentary

release occur beyond this depth.

LGM sedimentary fluxes were calculated taking into account sea level changes.

We considered a 125 m lower sea level (Lambeck et al., 2014) when calculating the sub-grid bathymetry (ocean volume remained unchanged), obtaining lower or zero ocean bottom fractions over continental shelves and higher values in deeper, off-shore grid boxes. This results in lower sedimentary fluxes around continents, and higher fluxes in deep waters (Fig. 3.3).

### 3.3.5 Iron from hydrothermal fluxes

As we mentioned in 3.3.2, PI hydrothermal fluxes were obtained from Tagliabue et al. (2014). Recently, a sediment core from the Mid-Atlantic Ridge provided evidence that due to lower sea level and bottom pressure, LGM hydrothermal iron fluxes may have been up to eight times higher than today (Middleton et al., 2016). We thus produce an LGM simulation where hydrothermal iron fluxes are increased five-fold from their PI values (Fig. 3.3).

### 3.3.6 Experiments

In Table 3.1 we describe our full array of experiments. By combining different results we can isolate the effect of each of the LGM-PI variations that we apply. PI_control is used to compare LGM experiments to. LGM_default uses LGM boundary conditions as described in section 3.3.1, but uses PI iron in-

Table 3.1: Experiments carried out in this work. Boundary conditions, surface iron deposition, sub-grid bathymetry, and multiplying factor of hydrothermal iron input are specified. LGM high refers to LGM surface iron deposition with 10× factor in the SO.

| Experiment name | B.C. | Surf. Fe dep. | Sub-grid bathy. | Hydrothermal Fe |
|---|---|---|---|---|
| PI_control | PI | PI | PI | ×1 |
| LGM_default | LGM | PI | PI | ×1 |
| LGM_sed | LGM | PI | LGM | ×1 |
| LGM_dust | LGM | LGM | PI | ×1 |
| LGM_Fe | LGM | LGM | LGM | ×1 |
| LGM_hydro | LGM | LGM | LGM | ×5 |
| LGM_highFe | LGM | LGM high | LGM | ×1 |

puts. LGM_sed and LGM_dust are like LGM_default but with LGM sediment and surface soluble iron fluxes, respectively. LGM_Fe combines both modifications. LGM_hydro is like LGM_Fe but with the addition of extra hydrothermal iron. LGM_highFe uses higher LGM surface iron fluxes in the SO as described in section 3.3.3. Each experiment was run for 6 ky from PI conditions, and results from the last 500 years are shown, when drift in global tracers is lower than 0.1 %.

## 3.4 Results

### 3.4.1 Modern biogeochemistry

Distributions of DIC, $PO_4$ and $NO_3$ are generally well represented in our PI control simulations, with correlations to modern observations higher than 0.9, similar to previous versions (Somes and Oschlies, 2015).

PI DFe fields fail to reproduce the high variability in the deep ocean of observations compiled by GEOTRACES (Tagliabue et al., 2012, updated to its 2015 version). Our model result produces smooth fields, and its standard deviation is one order of magnitude smaller than that of the observations, which appear noisy (Fig. 3.4). This produces low correlation coefficients in most depth sections when compared to observations (Table 3.2). The GEOTRACES iron data has a temporal sampling bias, with more measurements taken in summer months in each hemisphere, and a time span of 20 years that includes high inter-annual differences (Tagliabue et al., 2012). Our equilibrium simulation does not capture other temporal variability than the seasonal cycle, and we compare the data to the annual mean of model results, which contributes to model-data mismatches. If we only include data points inside the $\pm$ two standard deviations from the mean (DFe $\leq$ 3.11 nM, data points decrease from 18440 to 18196) the correlations are improved, illustrating that data outliers are a significant cause for the disagreement. RMSE and model-data biases are higher in this case, due to an overestimation in the model's ocean's interior DFe concentrations, which produces modeled means to be closer to observations when higher values are not removed from the data set.

The model overestimates the deep DFe global mean by up to 25 %, probably due to too little scavenging to counter the high DFe additions from hydrothermal sources. It is possible that the stability constant that we use for the chemical equilibrium of ligand-bound iron, free ligands and free iron is too high for deep waters, since our value has been reported for the upper ocean, while lower values exist elsewhere. This would shift the equilibrium too much towards the ligand-

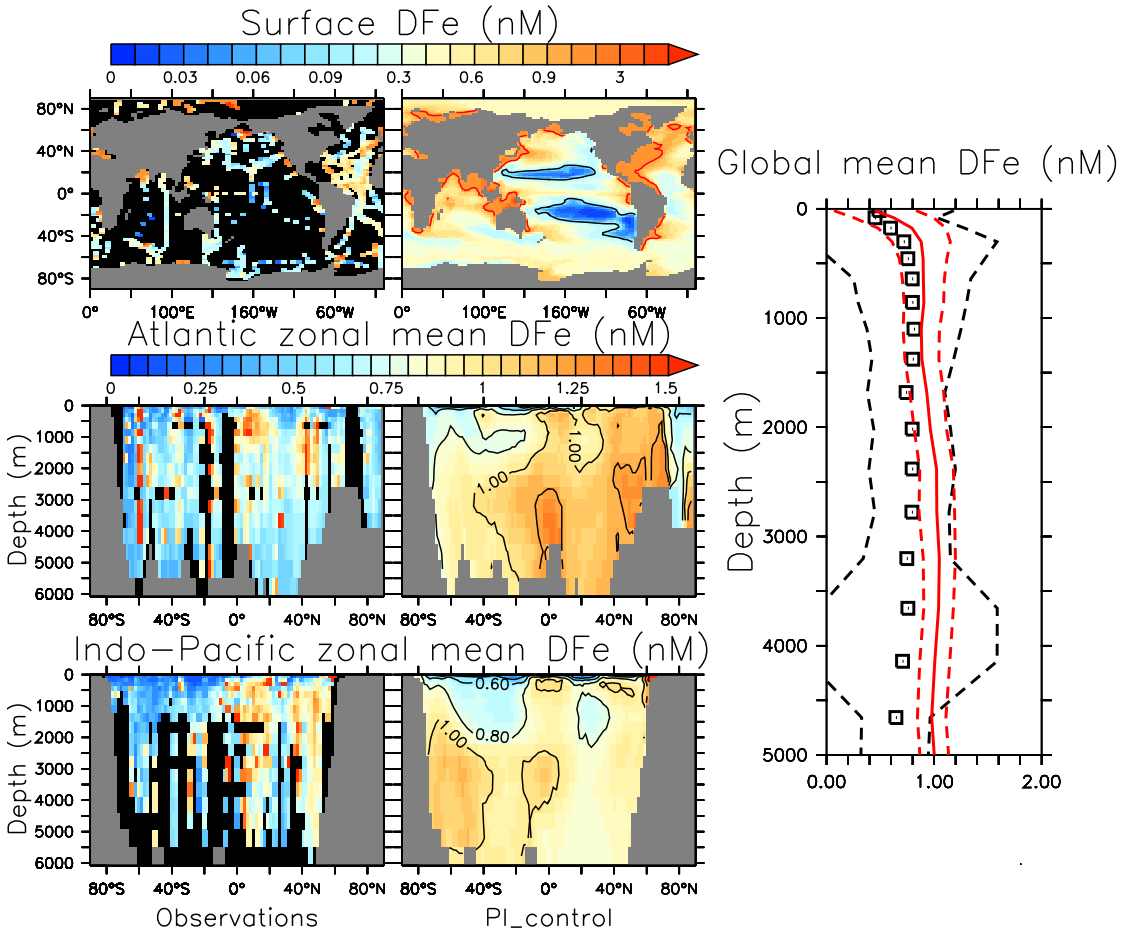


Figure 3.4: Top left: Surface DFe from modern GEOTRACES observations and PI_control. Black (red) contours are the 0.1 (1) nM isolines. Color scale is logarithmic. Center and bottom left: Zonally-averaged DFe concentrations versus latitude from modern GEOTRACES observations and PI_control, for the Atlantic and Indo-Pacific oceans. Far right: Global mean DFe vs depth, (black squares) from observations and (red line) PI_control, averaged over locations where observations exist. Black (red) dashed lines show the ± standard deviations of the observations (model).

Table 3.2: DFe correlation coefficient, standard deviation-normalized root mean square error (unitless), and model-observation bias of PI_control versus observations from GEOTRACES (Tagliabue et al., 2012), for the same depth sections of Tagliabue et al. (2016). Values obtained comparing to all GEOTRACES data points/only data inside the $\pm 2\sigma$ confidence bar.

| Parameter | Global | 0-100 | 100-500 | 500-1000 | 2000-5000 |
|---|---|---|---|---|---|
| R | 0.25/0.36 | 0.22/0.25 | 0.23/0.39 | 0.33/0.44 | 0.17/0.25 |
| RMSE | 1.05/1.14 | 1.09/1.24 | 1.03/1.13 | 0.97/0.98 | 1.16/1.43 |
| Bias (nM) | 0.26/0.29 | 0.07/0.12 | 0.17/0.23 | 0.11/0.14 | 0.28/0.31 |

bound iron state, resulting in too little scavenging in deep waters (Gledhill and Buck, 2012).

GEOTRACES zonally-averaged sections of DFe show deep localized maxima, that are not well reproduced in the ocean biochemistry model (Fig. 3.4). Some mid-depth maxima are associated with geothermal iron release, which according to recent observations has a very distinguishable signal, like in the South Pacific where DFe is transported for longer distances than previously thought, and a far-reaching plume is observed (Resing et al., 2015). Our model at that location exhibits a lower DFe zonal gradient, with values away from the geothermal plume higher than the observations. This is probably caused by too low deep scavenging that imposes that too much geothermal iron is mixed in the water column before being transformed into PFe, resulting in a more homogeneous distribution and higher background values than the observations.

The model surface mean has a lower bias with respect to observations than other sectors (Table 3.2, Fig. 3.4). At the surface, modeled DFe is overestimated in HNLC regions and in continental margins, similar to Nickelsen et al. (2015).

These differences could be due to biases in the fluxes of DFe, or the absence of diatoms as a separate type of phytoplankton in the model, that would increase iron consumption at high concentrations. Low DFe concentrations are well reproduced in the Pacific Ocean, as well as high values in some parts of the Atlantic.

Compared to the set of ocean iron models presented in Tagliabue et al. (2016), MOBI has lower correlation coefficient to observations than most of them, especially at the surface. Its global mean bias is similar to the other models', and in the surface ocean it is lower than in most of them. Some of the differences between other iron models and ours may lie in the sources included in them. Our total deep iron flux (sedimentary + hydrothermal, Table 3.3) is higher than in all but two of the models from Tagliabue et al. (2016). This, together with the lack of enough scavenging, probably results in the positive bias that we obtain through most of the water column. The poor knowledge that we have of the modern iron fluxes hinders our ability to properly constrain them, although we acknowledge that MOBI has room for improvement.

### 3.4.2 The LGM iron cycle

Colder water temperatures in LGM_default with respect to PI_control produce a 34 % decrease in DFe sedimentary release due to its temperature dependence (eq. 25 in Nickelsen et al. (2015)), and 19 % decrease in detrital remineralization rate (Table 3.3), resulting in lower ocean DFe.

Lower sea level has a negative effect on surface DFe, especially where continental

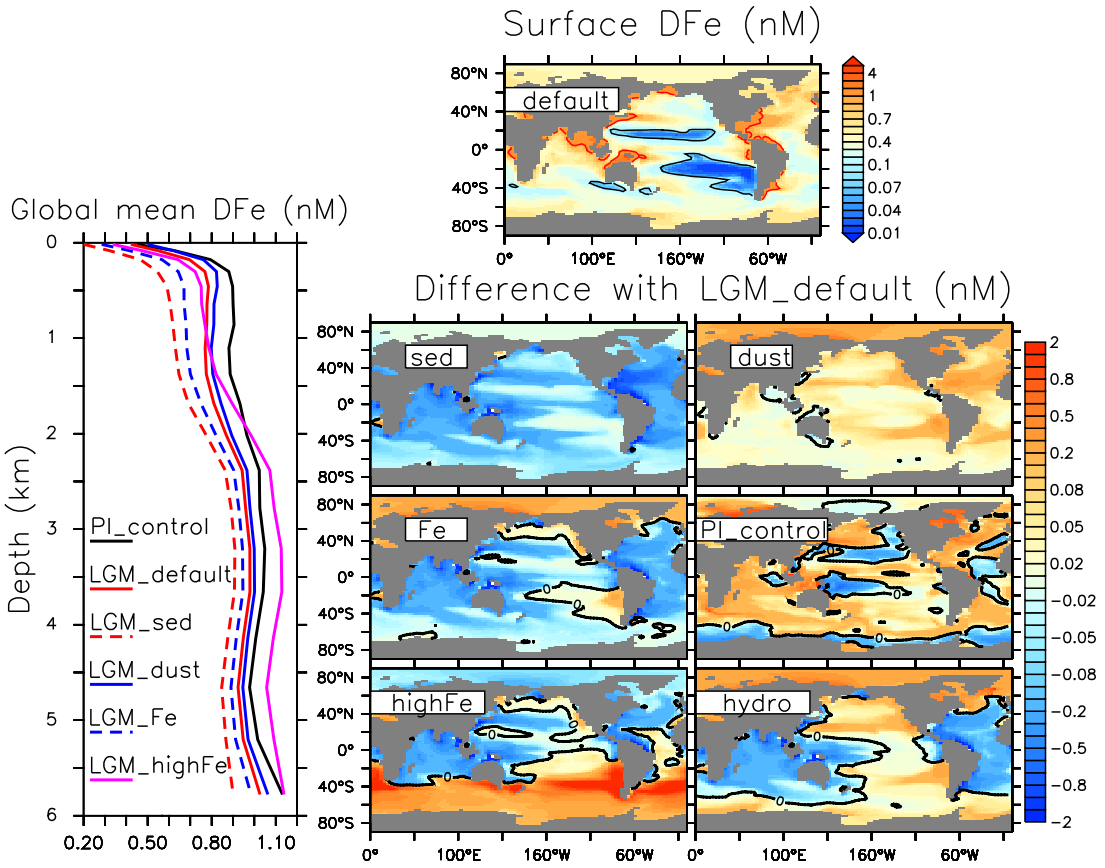


Figure 3.5: Upper panel: Surface DFe from LGM_default. Isolines as in Fig. 3.4. Lower-right six panels: Surface DFe differences between our experiments and LGM_default. xxx labels refer to the LGM_xxx experiment listed in Table 1, except for PI_control. Color scales are logarithmic. Left panel: Global mean DFe vs depth for some of our experiments. LGM_hydro values lay beyond the scale of the plot.

Table 3.3: DFe global and surface ($0 - 120$ m) contents (in Tg Fe units), and surface, hydrothermal, sedimentary, PFe remineralization, and scavenging fluxes (in Tg Fe/y units) from our model simulations.

| | Global DFe | Surf. DFe | Surf. | Hydr. | Sed. | Remi. | Scav. |
|---|---|---|---|---|---|---|---|
| PI_control | 68.920 | 1.050 | 0.05 | 0.63 | 0.77 | 5.60 | 5.14 |
| LGM_default | 63.760 | 0.915 | 0.05 | 0.63 | 0.51 | 4.00 | 3.76 |
| LGM_sed | 56.980 | 0.542 | 0.05 | 0.63 | 0.22 | 2.52 | 2.47 |
| LGM_dust | 65.400 | 1.046 | 0.10 | 0.63 | 0.45 | 4.10 | 3.94 |
| LGM_Fe | 59.820 | 0.686 | 0.10 | 0.63 | 0.24 | 2.80 | 2.72 |
| LGM_hydro | 71.34 | 0.795 | 0.10 | 3.20 | 0.25 | 5.90 | 8.00 |
| LGM_highFe | 67.340 | 1.078 | 0.26 | 0.63 | 0.23 | 3.40 | 3.48 |

shelves become exposed and no longer contribute to sedimentary flux. A glacial simulation with LGM sub-grid bathymetry (LGM_sed) produces surface DFe values lower than those obtained in LGM_default almost everywhere (Fig. 3.5). DFe sedimentary flux decreases by 57 % globally and surface concentrations by 41 % compared with LGM_default, and by 71 % and 48 %, respectively, compared with PI_control.(Table 3.3).

Using LGM atmospheric soluble iron deposition (LGM_dust) has the opposite effect, and leads to a modest increase in global surface DFe. Most of the increase occurs in the subtropics, in the North Atlantic and in the Arctic, whereas the impact is minimal in the SO, southern Indian and tropical Pacific. The differences in surface DFe among experiments are persistent throughout the water column, illustrating efficient downward transport through scavenging (Fig. 3.5).

Adding both effects together (LGM_Fe), we obtain higher surface DFe values in some regions, but the effect of lower sedimentary release dominates in most of the

ocean. The extra increase in SO LGM surface flux of LGM_highFe surpasses the sea level effect in that region and produces high DFe, especially in the $30° - 50°$ S band, where surface values are up to 20 times higher than in LGM_default (Fig. 3.5).

Multiplying the hydrothermal source of DFe by 5 (LGM_hydro), although globally a much larger addition than LGM_highFe, produces a relatively smaller effect on surface concentrations. However, the 15 % increase in SO export production between LGM_hydro and LGM_Fe (Table 3.4) shows that there is some amount of control of hydrothermal DFe on primary productivity, as suggested by recent measurements and simulations by Resing et al. (2015).

High concentrations of DFe are always accompanied by high scavenging and water column PFe remineralizarion (Table 3.3). If the extra iron input comes from deep sources then DFe scavenging prevents it from producing surface iron fertilization. The increase in scavenging due to the addition of extra atmospheric dust is more modest, allowing surface values to increase more.

### 3.4.3 Effects on the LGM carbon cycle

Our modeled LGM ocean has lower mean DIC than PI_control (Table 3.4). The reasons are the constant atmospheric $CO_2$ boundary condition that we use, which in the LGM forces the ocean to equilibrate to a lower value than in the PI, and the lack of a sediment model that would enable changes in ocean alkalinity (Schmittner and Somes, 2016).

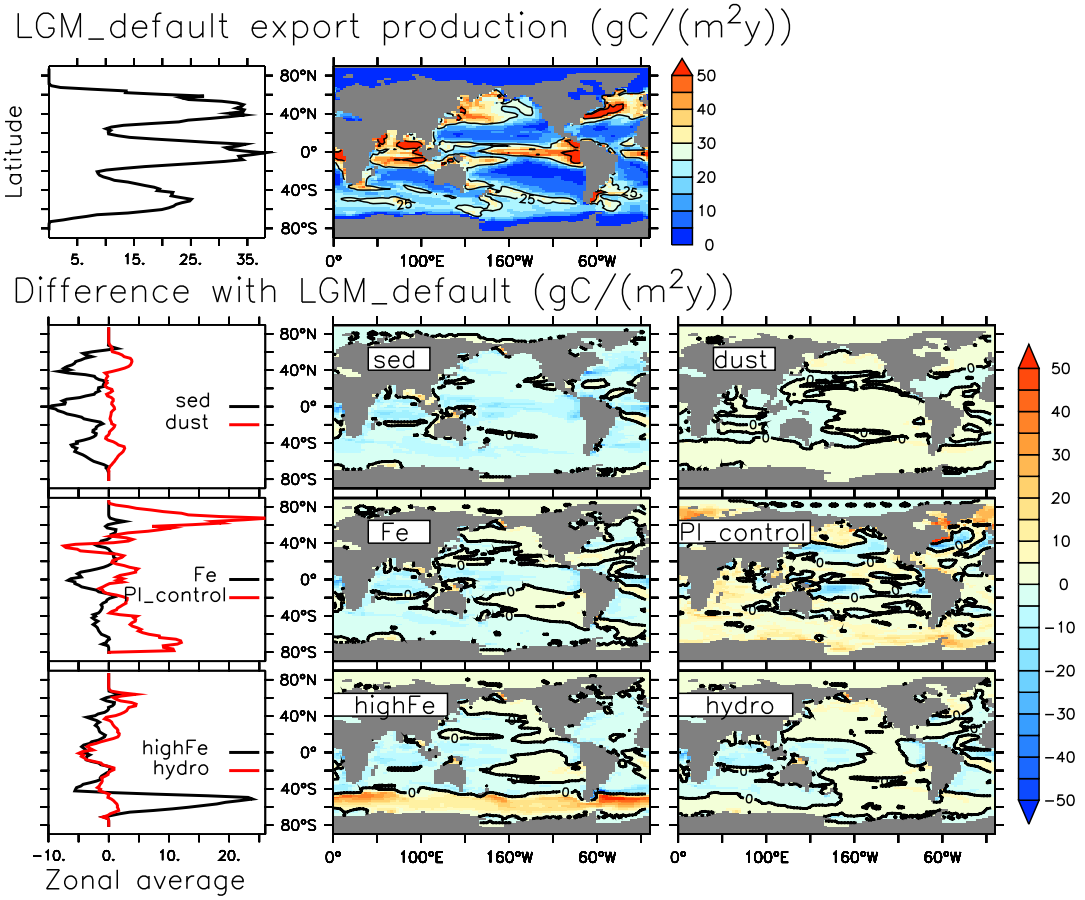


Figure 3.6: Upper panel: LGM_default export production. Lower panels: Differences between LGM experiments and LGM_default. Left side plots are zonal averages versus latitude (with transposed axes) for the experiments shown at each row. Labels as in Fig. 3.5.

Table 3.4: Simulations' SO (90°-40° S)/global phytoplankton content (in Pg C) and export production (in Pg C/y) out of the euphotic zone (calculated as the downward export of detritus at 120 m), global detritus remineralization below 2000 m (in Pg C/y), and global content of DIC (in Pg C). Parentheses standard deviations in the last digit from seasonal amplitude.

| | Phyto. | Exp. prod. | Detr. remi. | DIC |
|---|---|---|---|---|
| PI_control | 0.14(11)/0.66(6) | 1.9(2)/8.36(8) | 0.33(8) | 8333(1) |
| LGM_default | 0.11(8)/0.56(5) | 1.5(1)/7.42(6) | 0.39(7) | 8131(1) |
| LGM_sed | 0.09(7)/0.46(4) | 1.17(9)/6.00(5) | 0.31(6) | 8061(1) |
| LGM_dust | 0.12(9)/0.58(5) | 1.6(1)/7.67(6) | 0.41(7) | 8152(1) |
| LGM_Fe | 0.10(8)/0.51(4) | 1.3(1)/6.85(5) | 0.36(6) | 8106(1) |
| LGM_hydro | 0.11(9)/0.54(5) | 1.5(1)/7.24(6) | 0.39(7) | 8136(1) |
| LGM_highFe | 0.16(13)/0.58(9) | 2.2(2)/7.63(10) | 0.44(12) | 8251(1) |

The ocean carbon cycle is affected by changes in iron inputs via primary productivity and export of organic matter to deep waters. Experiments with higher phytoplankton concentrations have higher export production and DIC, indicating an increased efficiency of the biological pump. On the other hand, the decrease in sedimentary flux results in less organic carbon export out of the surface ocean (Fig. 3.6). Isolating the global effects of extra DFe in LGM_dust and LGM_hydro by comparing them to LGM_default and LGM_Fe, respectively, shows modest effects on global phytoplankton concentrations and export production (Table 3.4).

In the SO between Antarctica and 60° S, export production is lower in LGM simulations compared to PI_control because of the larger extension of sea ice. North of that, because of the prescribed ten-fold increase in SO atmospheric soluble iron flux, LGM_highFe exhibits a conspicuous increase in the band between 60° and 40° S. The maximum increase is from 30 to 70 g C/($m^2$y), between 45° and 55° S,

east of Patagonia (Fig. 3.6) coincidental with high atmospheric iron fertilization. LGM_highFe gives a result in agreement with Kohfeld et al. (2005), whose analysis indicated that LGM export production must have increased north of the Antarctic Polar Front but decreased south of it.

Sections of LGM-PI DIC (Fig. 3.7) show that waters with relatively higher carbon content originate in the upper SO, and propagate northward as deep and intermediate waters. As a consequence of atmospheric iron fertilization, LGM_dust and LGM_highFe exhibit the highest organic carbon remineralization rates and global DIC contents (Table 3.4). In other experiments, the decrease in sedimentary iron release inhibits surface fertilization effects.

The very high hydrothermal deep iron flux in LGM_hydro does not produce a considerable change in DIC compared to LGM_Fe, which has the same set-up except for hydrothermal sources (Fig. 3.7). The extra DFe in LGM_hydro is quickly scavenged, and contributes less to export production than the higher surface flux of LGM_highFe.

The effect of high SO iron fertilization in LGM_highFe is important for the carbon cycle. SO export production out of the euphotic zone is higher than in PI_control (Table 3.4) and appears to be in better agreement with reconstructions (Martínez-García et al., 2014; Kohfeld et al., 2005). Its global DIC content is considerably higher than in other LGM experiments, as a result of more accumulation of remineralized organic carbon ($C_{remi}$), the amount of DIC formed by the respiration of organic matter.

For situations where there is no change in the physical characteristics of the

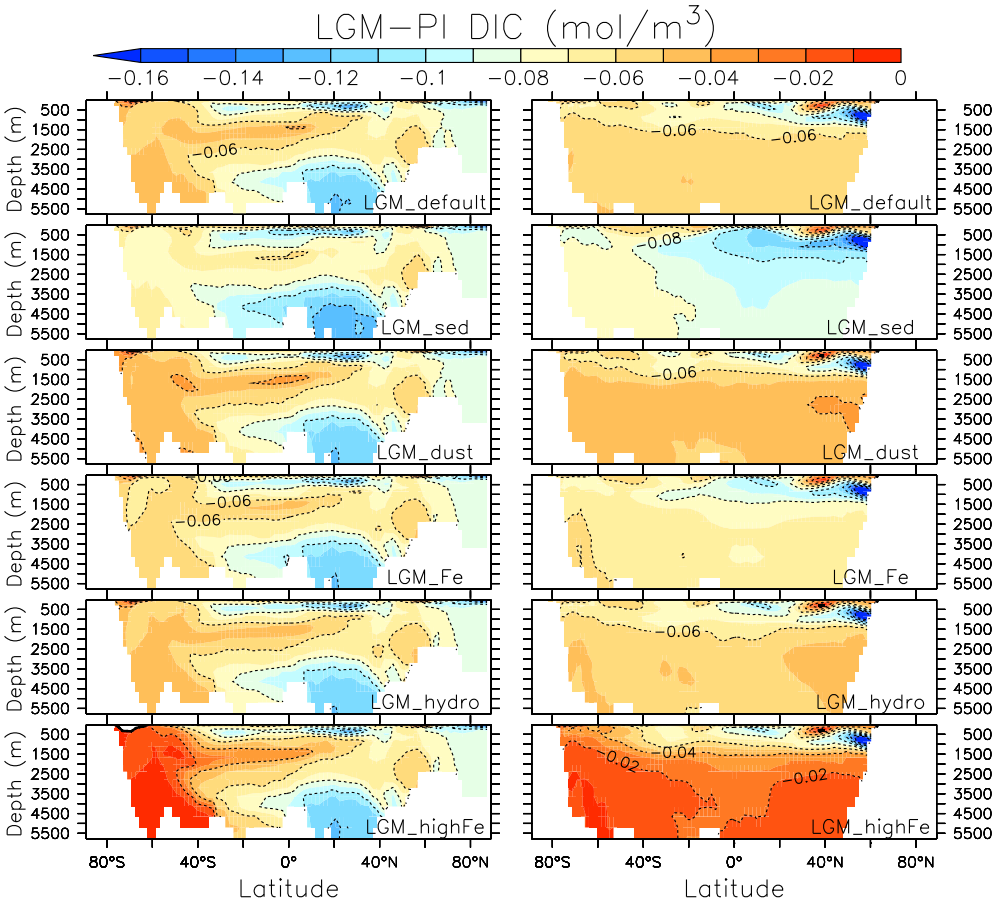


Figure 3.7: Zonally-averaged sections of DIC difference between LGM experiments and PI_control. Left (right) plots correspond to the Atlantic (Indo-Pacific) ocean basin.

ocean, like our LGM experiments, changes in $C_{remi}$ can be calculated from the formula $\Delta C_{remi} = R_{C:O} \times \Delta AOU$, where $R_{C:O}$ is the carbon to oxygen Redfield ratio and AOU is the apparent oxygen utilization. From $\Delta C_{remi}$ we can determine an associated change in atmospheric $CO_2$ (Ito and Follows, 2005):

$$\Delta pCO_2^{atm} = -\frac{V}{M\gamma}\Delta C_{remi}, \tag{3.2}$$

where $V = 1.358 \times 10^{18}$ m$^3$ is the volume ocean in our model grid, $M = 1.77 \times 10^{20}$ is the atmosphere's combined gas moles, and

$$\gamma = 1 + \frac{V\bar{C}_{sat}}{BMpCO_2^{atm}}. \tag{3.3}$$

$\gamma$ depends on $B = 10$, the buffer factor for sea-air equilibrium of carbon (Ito and Follows, 2005), $\bar{C}_{sat}$, the mean preformed carbon concentration at equilibrium with the atmosphere, and $pCO_2^{atm}$, which was set to 185 ppm in our LGM set up. For LGM_default, $\gamma = 8.98$. The uncertainty in our calculation of $\Delta pCO_2^{atm}$ is given by the assumption of an equilibrium state and air-sea equilibrium between preformed carbon and atmospheric $CO_2$. We calculated the uncertainty associated with the first assumption, obtaining a value of 3.6 %.

Isolating the surface iron fertilization effect by comparing LGM_dust to LGM_default, we obtain a decrease in $pCO_2^{atm}$ of 4 ppm (Table 3.5), about half of what Lambert et al. (2015) obtain from the same dust fields (with constant solubility parametrization, which results in higher SO fertilization than with our variable solubility method). The higher iron fertilization used in LGM_highFe raises this number

Table 3.5: Change in global remineralized carbon (in Pg C) and potential effect on $p\mathrm{CO}_2^{atm}$ (in ppm) corresponding to the different LGM-PI changes in DFe inputs that we analyze. Parentheses specify which experiments we compare to obtain each estimate. Results depends not only on the input changed, but also on the pair of experiments that are compared, thus the repetition of dust and sedimentary cases.

| Input changed | $\Delta \mathrm{C}_{remi}$ | $\Delta \mathrm{CO}_2$ |
|---|---|---|
| Dust (LGM_dust - LGM_default) | 78 | -4 |
| Dust (LGM_Fe - LGM_sed) | 174 | -9 |
| Sed. (LGM_sed - LGM_default) | -279 | 15 |
| Sed. (LGM_Fe - LGM_dust) | -182 | 10 |
| Sed. + dust (LGM_Fe - LGM_default) | -104 | 5 |
| Hydrothermal (LGM_hydro - LGM_Fe) | 118 | -6 |
| High SO dust (LGM_highFe - LGM_sed) | 537 | -28 |
| High SO dust + sed. (LGM_highFe - LGM_default) | 248 | -13 |

to 28 ppm, which is close to 25 ppm, from a PI experiment that included a dust flux increase of comparable magnitude to LGM_highFe (Nickelsen and Oschlies, 2015). By comparing LGM_sed with LGM_default we can isolate the effect of changes in LGM sedimentary DFe release on $p\mathrm{CO}_2^{atm}$. In this case, a decrease in global $\mathrm{C}_{remi}$ produces a raise of 15 ppm. Increasing DFe hydrothermal flux has a 6 ppm negative effect on $p\mathrm{CO}_2^{atm}$, a value similar to changes produced by the default dust case but smaller than the effects of the high dust and sediment cases.

The non-linearity of the iron cycle brings additional uncertainties to $p\mathrm{CO}_2^{atm}$ estimates. Calculating the effect of increased dust and reduced sedimentary release from LGM_Fe-LGM_sed and LGM_Fe-LGM_dust, respectively, gives different values than the ones presented above, with a reduction (amplification) of the sedimentary (atmospheric) effect (Table 3.5).

Another source of uncertainty is the assumed constant ligand concentration.

A PI simulation where the global ligand concentration was decreased from 1.5 to 1 $\mu$mol/m$^3$ (not shown) exhibits higher scavenging and lower DFe, resulting in a potential $p\mathrm{CO}_2^{atm}$ increase of 5 ppm, of the order of magnitude of $\Delta p\mathrm{CO}_2^{atm}$ from the LGM experiments. For instance, our predictions of LGM-PI changes in ocean biogeochemistry and $p\mathrm{CO}_2^{atm}$ due to variations in iron fluxes may have been dampened or amplified by the effect of ligands, but our model configuration does not take this effect into account.

## 3.5 Discussion

SO surface iron fertilization has been hypothesized as one of the drivers of atmospheric $\mathrm{CO}_2$ sequestration and higher deep ocean DIC during the LGM (e.g., Sigman and Boyle, 2000), which some of our results support. However, because of the possibly lower sedimentary flux and the high uncertainties of our estimations, a negative effect on DIC from changes in the iron cycle, which translates into a potential increase in $p\mathrm{CO}_2^{atm}$, cannot be ruled out. In LGM_highFe the surface iron fertilization surpasses the sedimentary release effect, resulting in a potential 13 ppm lower $p\mathrm{CO}_2^{atm}$ (Table 3.5), which would be a significant contribution to glacial-interglacial $\mathrm{CO}_2$ changes. Given the uncertainty of LGM dust reconstructions, which results in mismatches of up to one order of magnitude between (Lambert et al., 2015) and (Albani et al., 2014), and the uncertainties in solubility estimates, this remains as a plausible scenario.

Our parametrization of sedimentary release is taken from Galbraith et al.

(2010), and is proportional to the organic carbon flux reaching the ocean floor. Dale et al. (2015) proposed a parametrization with DFe release as a function of organic carbon flux and bottom oxygen levels. They obtained surface iron fields more dependent on sediment fluxes, so their parametrization would presumably have a higher impact on LGM DFe changes.

Rivers have been pointed out to proportionate reactive iron to continental margins, balancing sources and sinks of sedimentary iron. A more realistic representation should include riverine DFe flux independently or as a part of the sedimentary flux (Nickelsen, 2015).

For the LGM-PI change in sedimentary release we decreased sea level by 125 m in the calculation of the model's sub-grid bathymetry. Conversely, glacial sea level changes were not spatially homogeneous, as isostatic adjustment produces local inhomogeneities in sea level in the presence of ice sheets (Clark et al., 2002). We performed an extra simulation using spatially inhomogeneous sub-grid bathymetry calculated from the ICE-6G LGM bottom topography (Peltier et al., 2015) to test the significance of spatially variable sea level changes, finding very little difference compared to when spatially constant effects were accounted.

Our biogeochemical model only includes diazotrophs and general phytoplankton as primary producers. The lack of diatoms and/or a silicate cycle means that we cannot simulate species shifts due to changes in DFe. We have parametrized this effect by using a variable iron half saturation constant that increases proportionally with phytoplankton concentrations. This assumes that at higher iron concentrations we get bigger phytoplankton cells, which in turn require more iron

uptake for their metabolism (Nickelsen et al., 2015). We have not included the increase in ballasting associated with such shifts from light to heavier cells, so we might be underestimating changes in SO export production.

Another possible limitation of our model is its coarse resolution. In the modern ocean iron fertilization can cause primary productivity to increase considerably in continental margins and around islands (Moore et al., 2000a). Such meso-scale features are not captured in our simulations, and instead we have an open ocean, less intensified effect. The coarse resolution may also cause underestimations of sedimentary flux over narrow shelves, or other steep but otherwise small features that are not well defined by our sub-grid bathymetry parameter (Somes et al., 2017).

Iron-binding ligands are an important component of the ocean iron cycle and limit DFe scavenging. Their concentration was kept constant, so we do not address effects of variations in ligand concentrations due to changes in iron fluxes or from glacial/interglacial conditions. Our choice of leaving ligand concentrations constant is based on the uncertainty in the LGM-PI direction of change of the numerous factors affecting them (Völker and Tagliabue, 2015). Changes in ligands could be as important as iron fluxes, and should be taken into account in future studies, especially if a better understanding of their processing is achieved (Parekh et al., 2008).

Our work does not explicitly consider other processes that could have produced glacial-interglacial changes in the carbon cycle. Changes in ocean circulation (Brovkin et al., 2007), stratification (Franois et al., 1997), phosphorous

burial (Palastanga et al., 2013) and nitrate fluxes (Somes et al., 2017) have been pointed out to affect the LGM's ocean biogeochemistry and carbon. Our analysis suggests that when evaluating the effect of changes in the ocean iron cycle on glacial-interglacial atmospheric $CO_2$ variations, it is necessary to take into account sedimentary and hydrothermal fluxes, as well as surface fluxes. This result is in line with the recent realization of the importance of iron sources other than dust (Tagliabue et al., 2017).

## 3.6 Conclusions

We have performed sensitivity experiments with an ocean biogeochemical model that includes iron as one of its interactive nutrients, to test the significance of iron changes in glacial-interglacial variations of the carbon cycle. Our results show that in the LGM, increased dust deposition decreases atmospheric $CO_2$, but a reduction of sedimentary flux has the opposite tendency in a similar magnitude, resulting in a small net effect on atmospheric $CO_2$ sequestration. Most of the additional iron from enhanced hydrothermal fluxes were scavenged before reaching the surface limiting its effect in our model. Note that changes in ligand concentrations are not addressed in this work. Only with highly increased SO soluble iron deposition, of $\geq 10$ times PI values, can the decrease in sedimentary release be overcompensated, and atmospheric $CO_2$ be reduced by up to 13 ppm, as suggested by Martin's [1990] hypothesis. Our study suggests that all important iron flux processes should be considered to accurately quantify the global iron effect on glacial-interglacial

atmospheric $CO_2$ variations.

# Chapter 4: Weak overturning circulation and increased iron fertilization maximized carbon storage in the glacial ocean

Juan Muglia[1], Luke C. Skinner[2], and Andreas Schmittner[1]

[1]College of Earth, Ocean and Atmospheric Sciences, Oregon State University, Corvallis, USA

[2]Godwin Laboratory for Palaeoclimate Research, Department of Earth Sciences, Univ. of Cambridge, Cambridge, UK

## 4.1 Abstract

Circulation changes have been suggested to play an important role in the sequestration of atmospheric $CO_2$ in the glacial ocean. However, previous studies have resulted in contradictory results regarding the strength of the Atlantic Meridional Overturning Circulation (AMOC) and three-dimensional, quantitative reconstructions of the glacial ocean constrained by multiple proxies remain lacking. Here we simulate the modern and glacial ocean using a coupled, global, three-dimensional,

physical-biogeochemical model constrained simultaneously by $\delta^{13}$C, radiocarbon, and $\delta^{15}$N to explore the effects of AMOC differences and Southern Ocean iron fertilization on the distributions of these isotopes and ocean carbon storage. We show that $\delta^{13}$C and radiocarbon data sparsely sampled at the locations of existing glacial sediment cores can be used to reconstruct the modern AMOC accurately. Applying this method to the glacial ocean we find that a surprisingly weak ($6-9$ Sv or about half of today's) and shallow AMOC maximizes carbon storage and best reproduces the sediment data. Increasing the atmospheric soluble iron flux in the modeled Southern Ocean by up to 20 preindustrial values intensifies export production, carbon storage, and improves agreement with $\delta^{13}$C and $\delta^{15}$N reconstructions, whereas further increases have less of an effect. The best fitting model, which is a significant improvement compared with previous studies, suggests that a weak and shallow AMOC and enhanced iron fertilization conspired to maximize carbon storage in the glacial ocean.

## 4.2 Introduction

During the Last Glacial Maximum (LGM, $\sim$ 21 ka before present) the atmospheric $pCO_2$ was about 100 ppm lower than its pre-industrial (PI) value (Marcott et al., 2014). Changes in circulation, sea ice cover, and/or biogeochemistry, have been suggested to enhance carbon storage in the ocean, but quantitative, three-dimensional, data-constrained estimates of these effects remain scarce (Sarnthein et al., 2013; Goodwin and Lauderdale, 2013; Skinner et al., 2017).

Reconstructions of stable carbon isotope ($\delta^{13}$C) distributions from LGM sediments indicate that glacial North Atlantic Deep Water (NADW) was shallower, and more remineralized nutrients were accumulated in the deep Atlantic (Gebbie, 2014), but changes in biogeochemistry would have also affected $\delta^{13}$C (Schmittner and Somes, 2016). However, no consensus on the glacial AMOC strength currently exists, with studies inferring weaker (Lynch-Stieglitz et al., 2007), similar (Böhm et al., 2015), or stronger (Kurahashi-Nakamura et al., 2017) overturning rates than today. Increased radiocarbon ($^{14}$C) ages reconstructed from deep sea sediments have been interpreted as a more sluggish circulation and more carbon storage (Sarnthein et al., 2013; Freeman et al., 2016) although it is known that increased sea ice cover (Schmittner, 2003) and lower $pCO_2$ (Bard, 1988; Galbraith et al., 2015) could have also modulated the $\Delta^{14}$C observations to some extent and radiocarbon ages are not equivalent to ideal ventilation ages (Khatiwala et al., 2012). Moreover, modeling studies simulating an AMOC shutdown show large differences in its effects on ocean carbon storage (Brovkin et al., 2007; Schmittner and Galbraith, 2008; Tagliabue et al., 2009; Menviel et al., 2015) and a quantitative analysis on the effects of gradual AMOC changes on ocean carbon storage remains unexplored.

An increase in biological production and export of organic matter could have transferred carbon from the surface to deep waters during the LGM, causing atmospheric $pCO_2$ to decrease. In most of the present Southern Ocean (SO) productivity is limited by low concentrations of dissolved iron (DFe). Higher SO DFe due to increased dust deposition could have made this region a more efficient carbon sink

during the LGM (Martin, 1990). Observations indicate that LGM atmospheric dust fluxes into the SO were orders of magnitude higher (Maher et al., 2010; Lambert et al., 2015) and that the soluble iron content in LGM dust (Conway et al., 2015) was also increased compared to today. Nitrogen isotopes ($\delta^{15}$N) measured in SO sediment cores have been interpreted as more efficient nutrient utilization in the LGM (Martínez-García et al., 2014), supporting the idea of enhanced iron fertilization. However, $\delta^{15}$N distributions are affected by other processes too (e.g. (Somes, Schmittner, Galbraith, Lehmann, Altabet, Montoya, Letelier, Mix, Bourbonnais, and Eby, 2010)), complicating attributions.

Here we use a three-dimensional global climate/circulation/biogeochemistry model (see Chapter 3), that includes, for the first time, three key isotopes ($^{14}$C, $^{13}$C, $^{15}$N) simultaneously and interactive iron cycling. Previous studies (Brovkin et al., 2007; Tagliabue et al., 2009; Bouttes et al., 2011; Menviel et al., 2017) only used individual isotopes (mostly $\delta^{13}$C), which did not allow separation between circulation and iron fertilization effects. Our comparisons of multiple simulated isotopes with sedimentary reconstructions exploit complementary constraints provided by these isotopes (Schmittner and Somes, 2016) and offer novel insights into the glacial ocean. We expand substantially on Schmittner and Somes (2016) by including interactive iron cycling and by examining effects of circulation changes. We calculate the effect on deep ocean carbon accumulation of the configurations studied.

## 4.3 Methods

### 4.3.1 Physical model

We use the global ocean circulation model from the University of Victoria (UVic) (Weaver et al., 2001), version 2.9. It consists on a three-dimensional dynamical ocean with 19 vertical levels at $3.6° \times 1.8°$ horizontal resolution governed by the primitive equations, coupled to a two-dimensional single-level atmosphere, with moisture and heat balances and fluxes between the two mediums, and a dynamical sea ice model. The model is coupled to a dynamic land vegetation model (Meissner et al., 2003). Wind stress, wind used in moisture and heat advection, and air-sea fluxes as well as clouds are prescribed from a present-day monthly climatology (Kalnay et al., 1996). Background vertical diffusivity was set to $3.5 \times 10^{-5}$ $m^2/s$. Our diapycnal mixing scheme includes a three-dimensional parametrization of tide effects (Schmittner and Egbert, 2013), but it does not consider changes in tidal energy dissipation. Isopycnal eddy diffusivity was set to $1.2 \times 10^3$ $m^2/s$. Higher values are applied in the tropics, to include effects of the Equatorial Intermediate Current System on temperature, salinity and dissolved oxygen (Getzlaff and Dietze, 2013).

LGM runs use an atmospheric $CO_2$ value of 185 ppm, and orbital parameters corresponding to 21 kyr. The wind stress fields are preindustrial (Kalnay et al., 1996) plus a multi-model mean LGM anomaly from the Paleoclimate Model Intercomparison Project Phase 3 (PMIP3) (Muglia and Schmittner, 2015). For the LGM continental ice sheets, we use the reconstruction from the PMIP3 set up

(Abe-Ouchi et al., 2015). It includes a $\sim$ 100 m height increase to all global land masses, accounting for the lower sea level of the LGM. We also applied a global 1 PSU addition to salinity to account for sea level drop. Changes in river routings were not included.

### 4.3.2 Moisture transport and circulation

Various processes and model parameters can affect the meridional overturning circulation (MOC). Here we modify the southern hemisphere moisture transport, which has been proven to be an efficient way to affect Antarctic Bottom Water (AABW) production and AMOC strength, producing different MOC states (Saenko et al., 2003). Sigman et al. (2007) suggested that changes in atmospheric water vapor transport played a role in glacial-interglacial changes in SO stratification and $CO_2$, but estimates of this transport in the LGM are uncertain.

Specific humidity in the UVic model is controlled by the equation

$$\rho_a H \left( \frac{\partial q}{\partial t} + \boldsymbol{\nabla}(\mathbf{u}q) - \boldsymbol{\nabla}(\mu \boldsymbol{\nabla} q) \right) = \rho_0 (E - P), \tag{4.1}$$

where $\rho_a$ and $\rho_o$ are the density of air and water, respectively, $H = 1.8$ km is a scale height, $\mathbf{u}$ is the mean wind velocity for the advection of moisture, $E$ and $P$ are evaporation and precipitation fluxes, respectively, $q$ is the specific humidity, and $\mu$ is the moisture eddy diffusivity. $\mu$ accounts for the transport of moisture due to any process that cannot be explained by the resolved advection. It has a

trigonometric dependence on latitude (Fig. B.1), with higher values at mid latitudes, where eddy processes are important features of atmospheric circulation. Larger diffusivities in the southern hemisphere compared with the northern hemisphere improve agreement with modern observations (Saenko et al., 2003). Thus, an anomaly $\mu_{SH}$ is added to the moisture diffusivity in the southern hemisphere.

Variations of $\mu_{SH}$ produce changes in the meridional transport of humidity from the equator to the SO (see Fig. B.1), and control the buoyancy of Antarctic Circumpolar waters. By decreasing $\mu_{SH}$ AABW becomes more saline, denser, and more dominant with respect to North Atlantic Deep Water (NADW) in their competition to occupy the deep ocean. As a consequence the interface between the two water masses shoals. If we use any negative value for $\mu_{SH}$, the AMOC collapses. Hence we can vary $\mu_{SH}$ among experiments and test the effect of different deep circulations and water mass distributions on biogeochemistry, isotopes, radiocarbon ages and carbon storage. We do this by multiplying $\mu_{SH}$ by a factor $\epsilon_q$ that goes from 1 (default $\mu_{SH}$) to $-0.5$.

### 4.3.3 Model of Ocean Biogeochemistry and Isotopes

UVic is coupled with the Model of Ocean Biogeochemistry and Isotopes (MOBI), version 1.8. It includes prognostic equations for $PO_4$, $NO_3$, DFe, $O_2$, DIC, dissolved organic matter (DOM), particulate organic matter (detritus), PFe, phytoplankton, zooplankton and diazotrophs (Chapter 3, Fig. 1). It is equipped with an advection-diffusion scheme, so tracers depend on ocean physics as well as biogeochemical

interactions. The P content of the ocean is assumed constant, but the N cycle includes $N_2$ fixation by diazotrophs (source of $NO_3$), and water column and benthic denitrification (sinks of $NO_3$).

The iron cycle includes external inputs from atmospheric dust deposition, sedimentary release and hydrothermal fluxes. Atmospheric deposition is calculated from a prescribed surface field and added to DFe at the surface. Sedimentary release is proportional to the flux of organic matter reaching the ocean floor, and to a sub-grid bathymetry parameter used to account for unresolved bottom features. Bulk hydrothermal iron fluxes at mid-ocean ridges are added locally to DFe concentrations at the corresponding grid boxes. The iron fluxes were described in detail in a previous chapter.

### 4.3.4 Iron fluxes

PI and LGM surface soluble iron fluxes were calculated from dust flux monthly climatologies (Lambert et al., 2015). We assume a 3.5 % iron content in dust (Mahowald et al., 2009), and variable iron solubility, obtained by parameterizing an atmospheric model's dust concentration-solubility relationship (Luo et al., 2008). In this parametrization, atmospheric iron solubilities are inversely proportional to dust fluxes, and range between 0.02 % to 2.0 %. Please see Chapter 3 for more details.

Compared to the PI, our calculated LGM surface soluble iron fluxes exhibit an increase in parts of the SO, to the east of the Patagonian region and around

continents (Chapter 3, Fig. 3). Yearly atmospheric surface fluxes to the ocean south of 35° S are 0.009 Tg/y for the PI and 0.018 Tg Fe/y for the LGM.

A recent estimation from two Antarctic ice cores suggests that surface soluble iron fluxes into the SO may have been more than 10 times higher during the LGM (Conway et al., 2015). As an upper end estimation of the effect of iron fertilization in the SO, we perform an experiment using an LGM surface iron flux field where solubilities are multiplied by 10 south of 35° S (Chapter 3, Fig. 3). In this case, the yearly atmospheric surface flux to the SO is of 0.18 Tg/y.

Sedimentary DFe flux in our model is proportional to the flux of organic carbon reaching the bottom of the ocean, with an exponential dependence on temperature, to account for temperature-dependent remineralization. In the real ocean sedimentary fluxes are especially relevant over continental shelves (Elrod et al., 2004), but UVic's coarse resolution bathymetry is not able to resolve these shallow bottom features. Therefore we use a sub-grid bathymetry function that specifies the fraction of ocean bottom at each ocean grid box, and is multiplied to the sedimentary release (see Chapter 3).

Lower sea level in the LGM exposed a fraction of present day continental shelves, so for LGM runs we lowered sea level by 125 m (Lambeck et al., 2014) in the topography map used to calculate the sub-grid bathymetry. This results in lower sedimentary fluxes around continents (Fig. S3).

### 4.3.5 Isotope and radiocarbon records

Sedimentary reconstructions of isotope ratios ${}^{13}R_C = {}^{13}\mathrm{C}/{}^{12}\mathrm{C}$ and ${}^{15}R_N = {}^{15}\mathrm{N}/{}^{14}\mathrm{N}$ from recent syntheses are used as described in (Schmittner and Somes, 2016). We express isotope ratios with respect to standard ratios with $\delta$ notations, where $\delta^{13/15}\mathrm{C/N} = ({}^{13/15}R_{C/N}/{}^{13/15}R_{C/N;std} - 1) \times 1000$. LGM $\delta^{13}$C data were obtained from 434 cibicides foraminiferal data published by Peterson et al. (2014), and are assumed to represent $\delta^{13}$C of DIC (Duplessy et al., 1984). We have added nine recently published data points, from south Pacific locations (Molina-Kescher et al., 2016; Sikes et al., 2016), and one from the equatorial Atlantic (Burckel et al., 2016).

Data of LGM-PI changes in $\delta^{15}$N of organic matter were compiled by Schmittner and Somes (2016), and add up to 51 observational values. We have added 54 more data points from the SO, compiled by Franois et al. (1997). They are compared here to simulated LGM-PI changes in detrital $\delta^{15}$N, averaged over the top 120 m of the water column.

LGM benthic-atmospheric radiocarbon ages were compiled from a combination of sediment data by Skinner et al. (2017). They include 256 points, distributed throughout the global ocean at different depths, although we only include 247 points in our analysis, after the removal of outliers (measurements that are higher than 6000 ${}^{14}$Cyr, following Skinner et al. (2017)). The mean LGM-PI radiocarbon age difference (calculated after regridding to the model's grid) of this data set is 784 ${}^{14}$Cyr if we include only data below 6000 ${}^{14}$Cyr, or 936 ${}^{14}$Cyr if we include all data. Radiocarbon age estimates from Skinner et al. (2017) depend on assumed

LGM surface reservoir ages. We recognize that this is a source of uncertainty, so we re-calculated the radiocarbon age differences using observed benthic minus planktonic LGM radiocarbon ages from (Skinner et al., 2017) plus surface reservoir ages from our best LGM circulation estimate (LGM_8), obtaining 673 $^{14}$Cyr. We consider 673 $^{14}$Cyr and 936 $^{14}$Cyr to be the upper and lower levels of uncertainty in the reconstructed estimate, and they are plotted as dashed lines in Fig. 4.3, although the real uncertainty may be larger.

We use $\Delta^{14}C_{atm} = 0$ for the applied atmospheric $^{14}C/^{12}C$ ratio, so in equilibrium simulations radiocarbon ages can be simply calculated as

$$\text{age} = -1/\lambda \, ln(\Delta^{14}C/1000 + 1), \tag{4.2}$$

where $1/\lambda$ is $5730/ln(2)$ y, the radiocarbon half-life (Godwin, 1962). Applying $\Delta^{14}C_{atm} = 0$ to LGM simulations may not be realistic, since during this period $\Delta^{14}C_{atm}$ was variable, decreasing from 600 to 400 permil (Ramsey et al., 2012), and this change could have an effect on radiocarbon ages. To test the magnitude of the effect of using constant $\Delta^{14}C_{atm}$ instead of a realistic timeseries, we performed a simulation where the ocean radiocarbon was equilibrated to $\Delta^{14}C_{atm}$ corresponding to 25 kyr, and then let $\Delta^{14}C_{atm}$ drift from 25 to 19 kyr, following the IntCal09 curve (Reimer et al., 2009). In this case, ocean radiocarbon follows the trend of $\Delta^{14}C_{atm}$, and radiocarbon ages were calculated for the year 20 kyr of the simulation. Obtaining radiocarbon ages when a variable $\Delta^{14}C_{atm}$ is applied is not as straightforward as eq. 4.2. We first have to determine the deep minus

surface apparent ventilation age (which in measurements corresponds to benthic minus planktonic age),

$$t_{B-P} = -1/\lambda \, ln(R(x,y,z)/R_s(x,y)), \tag{4.3}$$

where $R(x,y,z)$ is the $^{14}C/^{12}C$ ratio at a grid box, and $R_s(x,y)$ is the surface $^{14}C/^{12}C$ for the same horizontal position. The surface minus atmospheric radiocarbon age is the reservoir age $t_R(x,y)$, which we defined as the surface radiocarbon age from our constant $\Delta^{14}C_{atm}$ simulations. From $t_{B-P}$ and $t_R$ we can obtain the radiocarbon age as

$$\text{age} = t_{B-P} + t_R. \tag{4.4}$$

Our two methods for calculating deep radiocarbon ages, i.e., with a constant and with a variable $\Delta^{14}C_{atm}$, give very similar results (Fig. B.2). Radiocarbon ages calculated with each method are very similar for deep waters, although in the upper levels the ones with a variable $\Delta^{14}C_{atm}$ produce higher values. This provides evidence that assuming a constant $\Delta^{14}C_{atm}$ in LGM simulations does not yield considerable biases for radiocarbon age calculations.

### 4.3.6 Experiments

Although changes in the atmospheric meridional moisture flux in the southern hemisphere $F_{qSH}$ have been suggested to be important in glacial-interglacial cycles (Sigman et al., 2007), current estimates remain uncertain. Here we modify $F_{qSH}$

(Fig. B.1), which is an efficient way to change the MOC in the model, as lower $F_{qSH}$ leads to saltier AABW and a decreased AMOC (Saenko et al., 2003).

First, we seek to answer the following question. Can the modern AMOC be reconstructed by fitting the model to observed $\delta^{13}$C and radiocarbon ages sub-sampled on the relatively sparse sediment core locations available for the LGM ocean? For this purpose, we have produced different PI simulations with AMOC's ranging between 11 and 19 Sv. The best fit, considering both correlation coefficient $R$ and root mean square error ($RMSE$) as metrics, to both top-core $\delta^{13}$C and natural radiocarbon age, sampling only where LGM observations are available, is the model with an AMOC strength of 17.8 Sv, consistent with independent estimates ($17.2 \pm 0.9$ Sv (McCarthy et al., 2015)) from modern observations (Fig. 4.1). This result indicates that the $\delta^{13}$C and radiocarbon reconstructions given at the relatively sparse sampling of the LGM can be used to reconstruct the AMOC.

Table 4.1 lists all LGM experiments that include biogeochemistry and isotopes. Each was run for 6 ky, and results from the last 500 years are shown. LGM simulations use standard glacial boundary conditions (including wind stress as in Chapter 3), and they include changes in atmospheric and sedimentary iron fluxes (see Chapter 3 for more details). The experiments differ in their ocean circulation and in additional SO soluble iron fluxes.

Glacial atmospheric and sedimentary iron flux estimates are applied to all LGM simulations (Fig. 3.3). The atmospheric flux is prescribed from a glacial dust flux reconstruction (Lambert et al., 2015). A set of simulations is generated where the LGM atmospheric soluble iron flux to the SO is multiplied by 10 between 35° S

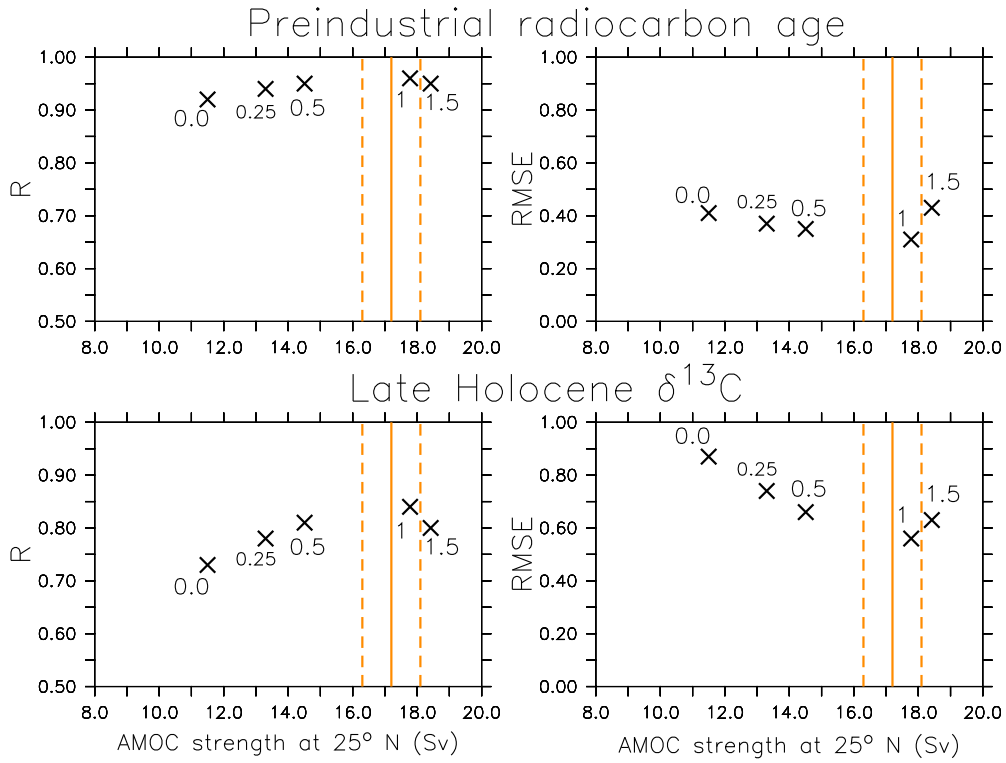


Figure 4.1: Comparison of different PI runs with measurements of water column natural radiocarbon ages (Key et al., 2004) and top-core sedimentary $\delta^{13}$C from the late Holocene (Peterson et al., 2014). Correlation coefficient $R$, and unit-less, standard deviation-normalized $RMSE$ are shown. Each cross corresponds to a different simulation, generated by varying the meridional moisture diffusivity with a scale factor $\epsilon_q$, indicated in the numbers next to each symbol. The simulations have AMOC strengths that range between 11.5 and 18.4 Sv. The orange full and dashed lines correspond to $17.2 \pm 0.9$ Sv, a modern estimate of AMOC strength at 26° N, using the RAPID mooring array (McCarthy et al., 2015). The simulation with lowest $RMSE$ and highest $R$ when compared to both radiocarbon age and $\delta^{13}$C, is also the run that is closest to observations, with an AMOC strength at 25° N of 17.78 Sv. This indicates that both isotopes are sensitive to and can be used to reconstruct the AMOC.

Table 4.1: Experiments. AMOC strength at 25° N (in Sv), which defines the experiments' labels, and global/SO atmospheric iron fluxes (in Tg Fe/y) are specified. Runs with the SOFe label include 10× LGM soluble iron deposition in the SO. We also include differences with PI_control in global DIC and remineralized organic carbon ($C_{org}$, both in Pg C units), which is assumed proportional to changes in apparent oxygen utilization. For the iron fluxes, the numbers in parentheses indicate the seasonal variability in the last significant digit. For the AMOC strengths, they indicate standard deviations in the last significant digit, taken from the last 500 y of the simulations. PI_control uses preindustrial boundary conditions. All other experiments use LGM boundary conditions.

| Experiment | AMOC | Atm. Fe flux | $\Delta$DIC | $\Delta C_{org}$ |
|---|---|---|---|---|
| PI_control | 17.79(2) | 0.053(5)/0.009(2) | - | - |
| LGM_13 | 13.51(1) | 0.096(7)/0.018(4) | -1153 | 30 |
| LGM_11 | 11.27(2) | 0.096(7)/0.018(4) | -936 | 135 |
| LGM_9 | 9.323(3) | 0.096(7)/0.018(4) | -805 | 193 |
| LGM_8 | 7.791(3) | 0.096(7)/0.018(4) | -738 | 221 |
| LGM_6 | 6.19(2) | 0.096(7)/0.018(4) | -706 | 227 |
| LGM_0 | 0.245(3) | 0.096(7)/0.018(4) | -791 | 195 |
| LGM_13_SOFe | 13.51(1) | 0.26(3)/0.18(4) | -656 | 383 |
| LGM_9_SOFe | 9.323(3) | 0.26(3)/0.18(4) | -270 | 585 |
| LGM_8_SOFe | 7.791(3) | 0.26(3)/0.18(4) | -205 | 602 |
| LGM_6_SOFe | 6.19(2) | 0.26(3)/0.18(4) | -164 | 605 |

and Antarctica, motivated by observations of increased solubility in the LGM SO (Conway et al., 2015). For a detailed analysis of the iron cycle see Chapter 3.

## 4.4 Results

### 4.4.1 Physics

The model's LGM AMOC decreases continuously with decreasing $F_{qSH}$ until about 6 Sv (Fig. 4.2; Table B.1), at which point it collapses. States with an AMOC between 0 and 6 Sv are unstable in this model version. They exhibit hysteresis behavior that is impacted by North Atlantic wind stress changes by decreasing the width of the hysteresis curve and stabilizing weak AMOC states (see Chapter 2). The resulting LGM circulation states range from a deep and vigorous AMOC in LGM_13 to a collapsed AMOC in LGM_0 (Fig. 4.2). Lower meridional moisture fluxes decrease (increase) precipitation south (north) of 45° S. As a result, surface salinities increase around Antarctica and decrease in sub-polar regions (Fig. B.3) relative to LGM_13. The surface SO cools, sea ice extent is increased, and net SO buoyancy flux decreases, enhancing Antarctic Bottom Water (AABW) production. In LGM_8 e.g., AABW reaches far into the deep north Atlantic (NA), and the interface with NADW becomes shallower (Fig. 4.2). The AMOC is very weak and shallow compared to LGM_13 and PI_control.

Circumpolar deep water inflow into the Indian and Pacific oceans and the associated MOC (IPMOC) is also weakened due to reduced NADW inflow into the

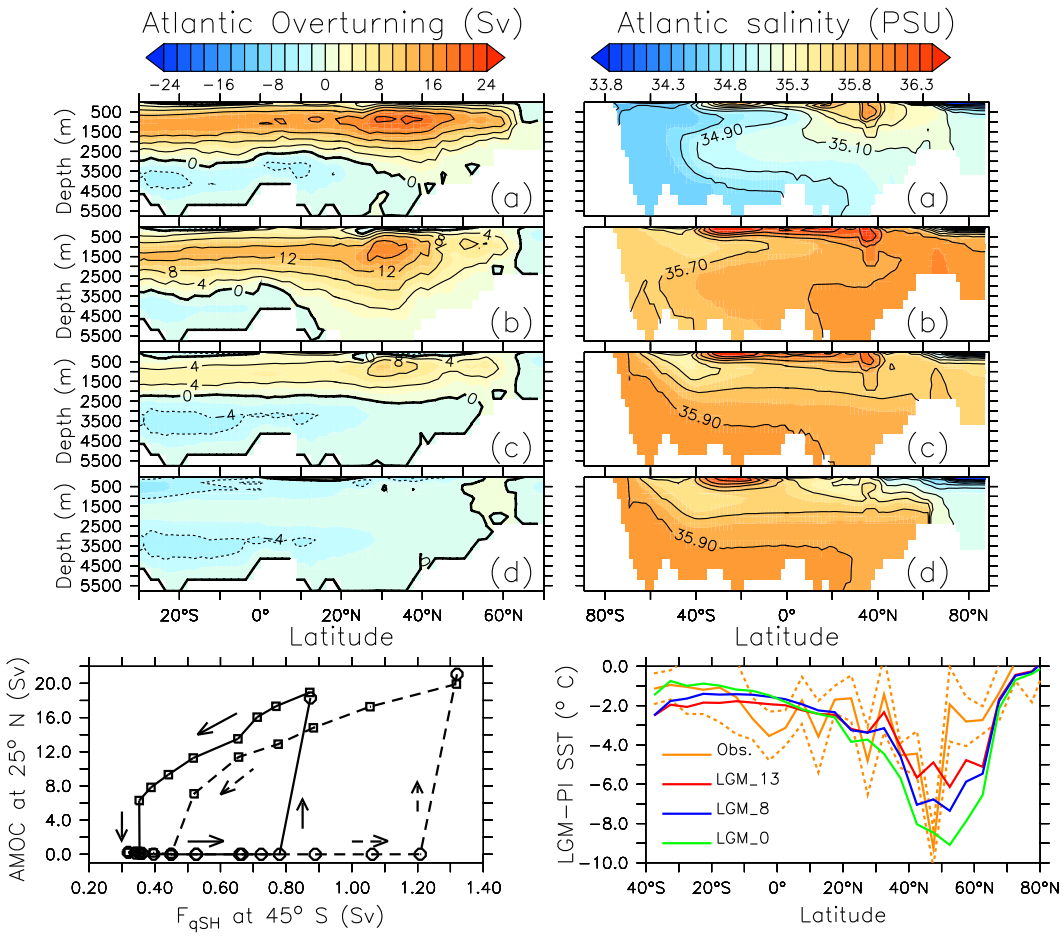


Figure 4.2: Top: Atlantic (left) meridional overturning and (right) zonally-averaged salinity for different simulated physical states; (a) PI_control, (b) LGM_13, (c) LGM_8, and (d) LGM_0. LGM salinities include a +1 addition due to lower sea level. Bottom left: Response of AMOC strength to (squares) decreases in southern hemisphere's meridional moisture transport ($F_{qSH}$); (circles) increases in $F_{qSH}$ from a collapsed state. Full line curve uses PI + LGM anomalies for wind stress fields; dashed line curve uses PI wind stress fields. Bottom right: Atlantic, zonally averaged LGM-PI sea surface temperature changes versus latitude for the same experiments, as indicated. Reconstructions (full orange line) from (Waelbroeck et al., 2009) ± propagated errors (dashed orange lines). Model means calculated using only grid boxes from which there exist LGM reconstructions.

Southern Ocean (Fig. B.4, Table B.1). Higher meridional pressure gradients increase Antarctic Circumpolar Current (ACC) transport by 40 % between LGM_8 and LGM_13 (Table B.1). In LGM_8, the ACC is also increased with respect to PI_control consistent with recent reconstructions (Lynch-Stieglitz et al., 2016). AABW is saltier than NADW in LGM_8 (Fig. 4.2), in agreement with sedimentary pore-water reconstructions (Insua et al., 2014; Adkins et al., 2002). LGM_13 has salinity distributions more similar to PI_control, but since pore-water reconstructions remain relatively sparse and have high uncertainties (Miller et al., 2015; Wunsch, 2016), salinity fields alone are insufficient to rule it out as a possible LGM scenario.

LGM-PI sea surface temperature (SST) changes are in the range of reconstructions from MARGO (Waelbroeck et al., 2009) for the Atlantic (Fig. 4.2) and Indo-Pacific (Fig. B.4) oceans, with some overestimations in the latter. Compared to MARGO, all experiments are in similarly good agreement, with a range of correlation coefficients $R$ of $0.93 - 0.95$ and $RMSE$ of $0.36 - 0.38$, which show the skill of our model to reproduce LGM SST's, but at the same time the uselessness of these data to constrain the LGM MOC.

### 4.4.2 Radiocarbon

Our LGM experiments predict older (in $^{14}$Cyrears) waters than PI_control in most of the deep ocean (Fig. 4.3). Even LGM_13, which has a similar although slightly reduced MOC as compared to PI_control, results in $\sim$ 300 y older radiocarbon

ages due to increased sea ice cover and lower $pCO_2$ (Table B.2). However, old LGM radiocarbon ages in the deep NA and Pacific predicted by reconstructions (Skinner et al., 2017) are only reproduced with a weak (or collapsed) AMOC and increased AABW. In the Atlantic, LGM_8 exhibits a clear separation between AABW with ages higher than 2000 y and NADW with ages younger than 1000 y at approximately 2500 m of water depth. Compared to PI_control, the depth of the interface shoals by about 1000 m and vertical gradients are much enhanced. The younger water mass disappears in LGM_0, and waters as old as in the North Pacific occupy the deep NA, inconsistent with most reconstructions.

Models LGM_9, LGM_8 and LGM_6 fit the sediment data best, as indicated by their higher $R$ and lower $RMSE$ (Fig. 4.3, Table B.2). This provides evidence that the LGM AMOC was active, but much weaker than in modern times.

Reconstructions of LGM radiocarbon ages from sediment cores are much noisier than modern water column measurements, indicating errors in the reconstructions. Reconstructions from (Skinner et al., 2017) regridded to our model's grid suggest a global LGM-PI difference of $670 - 900$ y. The global age differences between our LGM experiments and PI_control, calculated over grid boxes for which LGM data exist, vary between 283 and 635 y (Fig. 4.3, Table B.2), with LGM_6 producing the highest estimate. If we consider all grid boxes, the, LGM_6 produces a maximum aging among models of 630 $^{14}$Cyr, close to the interpolated estimate of $689 \pm 53$ $^{14}$Cyr from Skinner et al. (2017). Considering only depths below 2000 m, the simulations result in 281 to 828 y older waters, and model LGM_9 would fit best sedimentary reconstructions of 600 y (Sarnthein et al., 2013).

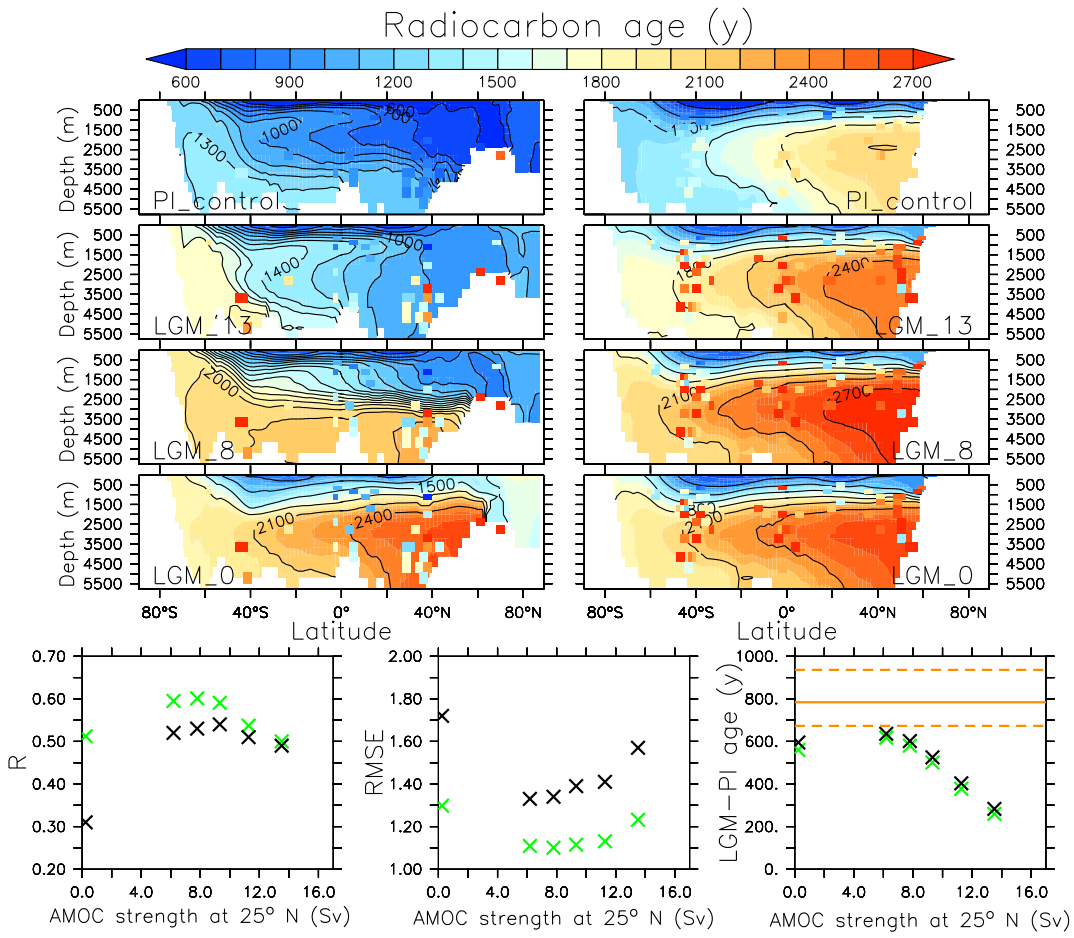


Figure 4.3: Top: Zonally averaged radiocarbon age sections from four representative experiments, as indicated. Left (right) corresponds to the Atlantic (Pacific) Ocean. Overlaid on the plots are data from the Global Data Analysis Project (Key et al., 2004) for PI_control, and from a combination of sediment data (Skinner et al., 2017) for the rest. Bottom: Correlation coefficient $R$, dimensionless, standard deviation-normalized root mean square error ($RMSE$) and global LGM-PI relative age difference for all of our LGM experiments compared to the reconstructions, as functions of AMOC strength. Black symbols correspond to modeled radiocarbon ages relative to the atmosphere; green symbols correspond to modeled radiocarbon ages relative to the surface ocean, plus surface reservoir ages estimated by Skinner et al. (2017). The orange line indicates the LGM-PI age difference from sediment reconstructions. Observation uncertainties (dashed lines) are given by their variability and the uncertainty of surface reservoir ages.

Discrepancies between our model and reconstructions could be related to the high variability of the reconstructions, e.g. in the deep NA (Fig. 4.3). Surface reservoir ages, which in the reconstructions were calculated either as modern reservoir ages plus 250 y (due to $pCO_2$ effects) or from independent dating (Freeman et al., 2016), have higher variability than our estimates but a similar mean value. Using the reservoir ages from reconstructions (Skinner et al., 2017) to recalculate the modeled ventilation ages improves the agreement with observations (green crosses in Fig. 4.3). This suggests that surface reservoir ages are a significant cause of difference between modeled and reconstructed ventilation age distributions.

### 4.4.3 Stable isotopes

A strong presence of high $\delta^{13}C$ NADW in the Atlantic as exhibited by LGM_13 is inconsistent with LGM reconstructions (Fig. 4.4). This model also produces too high Pacific $\delta^{13}C$, especially in the southern hemisphere.

In LGM_8 low $\delta^{13}C$ AABW penetrates into the northern hemisphere (NH). High $\delta^{13}C$ waters are confined to the upper 1500 m of the NA, consistent with observations (Peterson et al., 2014). A vertical profile of global $\delta^{13}C$ means from LGM_8 reproduces the decrease in reconstructed $\delta^{13}C$ with depth, in contrast to LGM_13, which results in a mid-depth maximum, and LGM_0, which results in a mid-depth minimum (Fig. 4.4). LGM_8 is in better agreement with observations than the strong and collapsed AMOC cases (Table B.2). The strong AMOC and deep NADW of LGM_13 fill the ocean with newly-formed waters, resulting in too

high $\delta^{13}$C below 2000 m. The collapsed AMOC of LGM_0 produces too low values in the upper 3500 m of the water column, and too high values below that.

Higher SO atmospheric iron flux increases phytoplankton productivity, carbon export, and deep DIC (see Chapter 3), intensifying $\delta^{13}$C depletion in the AABW of the deep Atlantic (LGM_13_SOFe and LGM_8_SOFe in Fig. 4.4) It also produces too low $\delta^{13}$C in the deep Pacific compared to observations, probably because most of the LGM's extra dust originated in Patagonia and delivered to the south Atlantic primarily (Lambert et al., 2015), such that fluxes over the south Pacific may have been less than those used in our SOFe models.

The representation of $\delta^{13}$C compared to observations improves in all LGM cases when the higher atmospheric soluble iron fluxes are applied. LGM_8_SOFe exhibits the highest $R$ (0.79) and lowest normalized $RMSE$ of anomalies from the mean ($RMSE' = 0.63$, Table B.2). and is the only simulation whose global mean falls inside the $\pm$ standard deviation of the observations' mean for all depths.

Experiments with increased SO atmospheric soluble iron flux have higher nutrient utilization and organic matter $\delta^{15}$N in the SO, improving considerably the agreement with LGM-PI reconstructions (Fig. 4.4). The model/observation $R$ is more than 50 % higher in the SOFe experiments than in the rest of LGM experiments (Fig. 4.5, Table B.2). Part of the extra iron is transported and upwelled to the east equatorial Pacific, increasing that region's primary productivity, nitrate utilization and water column denitrification (Fig. B.5), in agreement with some observations from sediment cores (Winckler et al., 2016), although other observations suggest that higher nutrients in the SO should cause lower productivity in

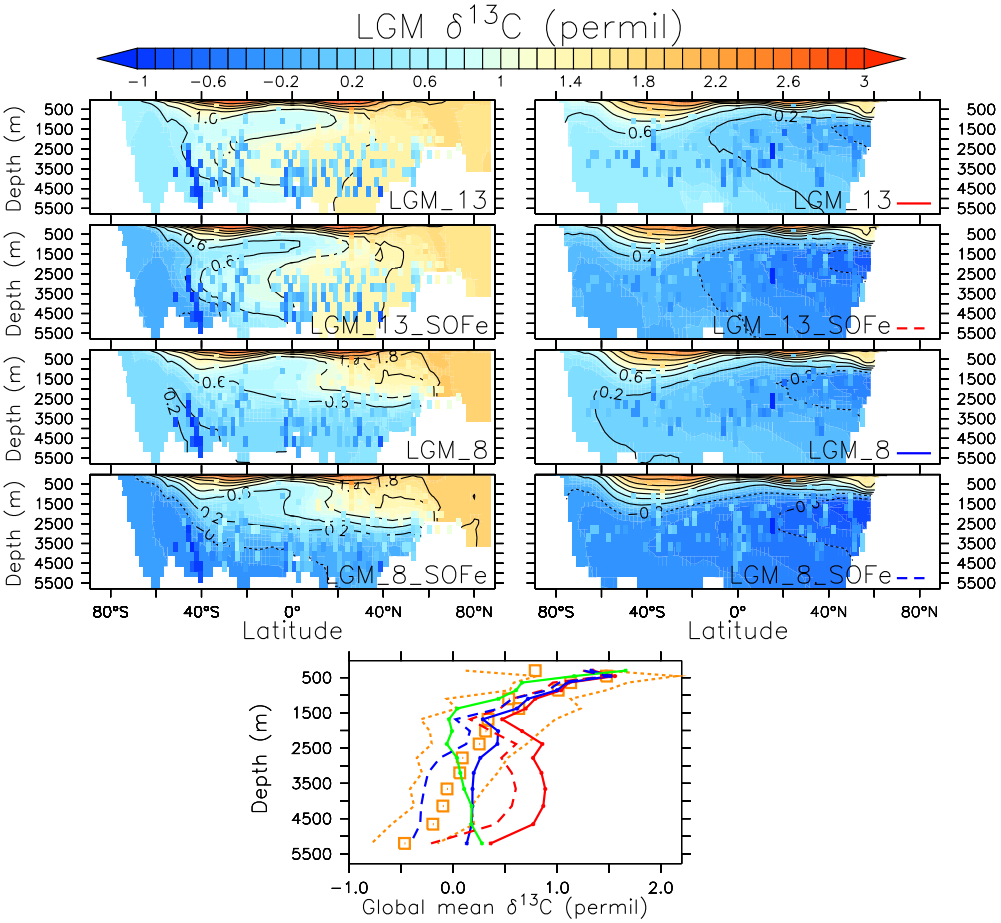


Figure 4.4: Top: Zonally averaged $\delta^{13}$C of DIC sections from four of our LGM experiments, as indicated. Left (right) corresponds to the Atlantic (Pacific) Ocean. Overlaid on the plots are zonally-averaged LGM data from foraminifera (see SM). Bottom: Depth profiles of global mean $\delta^{13}$C from our experiments, calculated using only grid boxes for which there exists LGM data. Red and blue: Experiments plotted in the meridional sections above, with line codes as indicated in the Pacific plots; green: LGM_0; orange squares: Observations' global mean; orange dotted lines: Observations $\pm$ standard deviations of the mean.

the equatorial Pacific (Costa et al., 2016). The effect increases $\delta^{15}$N locally, giving a better agreement with observed LGM-PI changes.

Circulation changes have a smaller effect on $\delta^{15}$N than iron fertilization (Fig. 4.5). Among the SO fertilization experiments, the ones with weaker circulation provide a slightly better fit to the data, due to a better estimation of SO $\delta^{15}$N increase and the reproduction of positive anomalies in the tropical Atlantic.

## 4.5 Discussion and Conclusion

Our experiments show that a remarkably weak, shallow AMOC with increased AABW entrainment to the Atlantic Ocean provides the best representation of LGM reconstructions of radiocarbon age and $\delta^{13}$C of DIC. We conclude that LGM AMOC strength at 25° N was between 6 and 9 Sv (Table 4.1), with a NADW shallowing of $1000 - 1500$ m with respect to PI. These model solutions suggest that the export of NADW into the SO was lower by about two thirds from 15 Sv in PI to 5 Sv in LGM_8 (Fig. 4.2). They represent a weaker AMOC than suggested by previous studies (Brovkin et al., 2007; Bouttes et al., 2011; Menviel et al., 2017) but qualitatively consistent with interpretations of LGM proxy data (Lynch-Stieglitz et al., 2007). A recent data assimilation study (Kurahashi-Nakamura et al., 2017) inferred a shallow and strong LGM AMOC (22 Sv), which resulted in a global LGM $\delta^{13}$C $RMSE$ of 0.50 permil compared to 0.40 permil in our best estimate. Moreover, our results suggest that a stronger LGM AMOC would have caused lower radiocarbon age differences than observed (Fig. 4.3), but

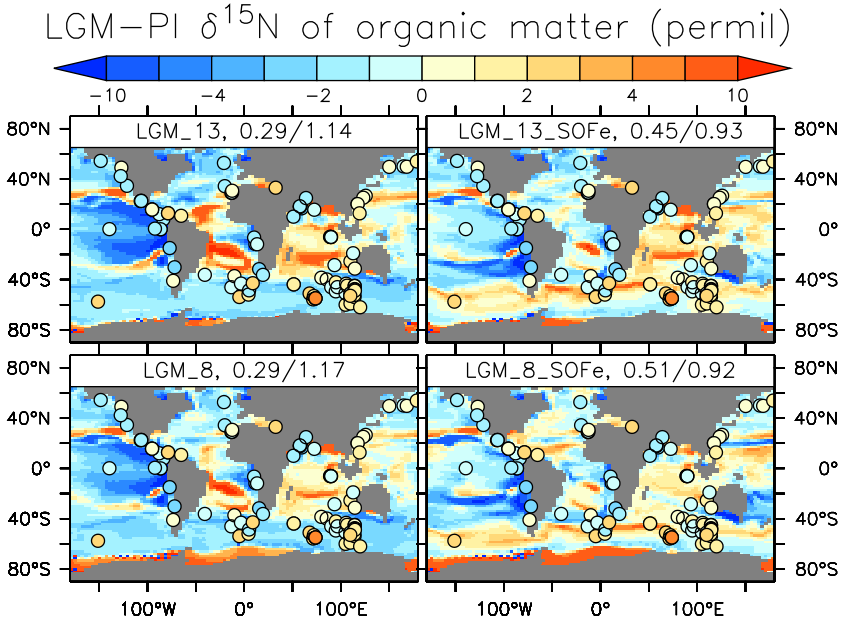


Figure 4.5: LGM-PI changes in $\delta^{15}$N of detrital (particulate organic) matter, averaged over the top 120 m of the water column. Labels above each map indicate the experiment names, and also include the $R/RMSE$ parameters of the simulations compared to observations. Models on the left use LGM atmospheric iron fluxes calculated from an LGM dust flux reconstruction (see Materials and Methods section in the SM); models on the right use the same LGM fluxes, but multiplied by 10 in the SO, between Antarctica and 35° S. Overlaid on the plots are LGM-PI values from observations, compiled by Schmittner and Somes (2016); Franois et al. (1997).

Kurahashi-Nakamura et al. (2017) did not use radiocarbon data as a constrain. We conclude that a shallow and strong AMOC is less likely in agreement with existing observations than a shallow and weak AMOC. Another recent work (Menviel et al., 2017) found the best match to LGM-PI $\Delta\delta^{13}$C to be a simulation with stronger AMOC than LGM_8 ($10 - 15$ versus 7.8 Sv) but weaker global AABW transport ($\leq 10$ versus 17 Sv, Table B.1). LGM_8 produces a slightly better fit to the same $\Delta\delta^{13}$C reconstruction ($R = 0.63$ and $RMSE = 0.31$ permil versus 0.6 and 0.33 permil in Menviel et al. (2017)), but also includes iron fertilization effects, and the additional constrain of $\delta^{15}$N isotopes. Since the AMOC in our model is not stable for values lower than 6 Sv, we cannot evaluate even weaker but non-collapsed states. However, the poor agreement between a collapsed state and reconstructions rules out that possibility.

The stronger wind stress over the North Atlantic that existed during the LGM as a consequence of the Laurentide Ice Sheet (Ullman et al., 2014; Muglia and Schmittner, 2015) stabilizes the AMOC despite a decrease in $F_{qSH}$ by increasing the gyre circulation and maintaining relatively high salinities in the North Atlantic (Fig. 4.2). However, it also decreases the width of the hysteresis curve indicating transitions between on and off states are more likely for a given perturbation of $F_{qSH}$.

A tenfold increase in the LGM atmospheric soluble iron flux produces an increase in export production (Table B.3), and improves the distribution of LGM $\delta^{13}$C and LGM-PI $\delta^{15}$N compared to observations. Although an increase from 0.053 to 0.26 Tg Fe/y atmospheric iron deposition may seem high, it is of the or-

der of magnitude of recent estimates of LGM soluble iron content in Antarctic ice cores (Conway et al., 2015). The real iron fertilization during the LGM may have been lower, but it must have been high enough to produce the observed LGM-PI changes in $\delta^{15}$N, although it is also possible that the real iron cycle has higher sensitivity to increases in dust flux than our model or that another mechanism such as species shifts due to increased dust fluxes (Moore et al., 2000b) caused the enhanced SO nutrient utilization. A recent work using the same model but without an interactive iron cycle suggested that global primary productivity must have been at least 17 % higher during the LGM to reproduce $\delta^{15}$N and $\delta^{13}$C isotope reconstructions (Schmittner and Somes, 2016). In our best simulation the increase is only 4 %, but by including circulation changes we obtain a better fit to reconstructions.

We tested iron fertilizations higher than the 10×LGM experiment presented here, finding little additional effect on the biogoechemistry and $\delta^{15}$N, and a slightly worse fit to $\delta^{13}$C observations (Fig. 4.6, circles). Scavenging acts to remove the extra DFe in these cases, preventing a higher increase in nutrient uptake by phytoplankton, indicating a saturation effect. A more realistic iron cycle that includes interactive ligands (Völker and Tagliabue, 2015) and/or phytoplankton species shifts could potentially further improve the agreement with $\delta^{15}$N reconstructions.

An additional simulation generated with a tenfold increase in LGM atmospheric soluble iron deposition over the whole ocean, instead of just the SO, produces 60 % lower $R$, indicating that the enhanced iron fertilization must have been restricted to the SO (Fig. B.6). This global iron-fertilization simulation overestimates LGM-

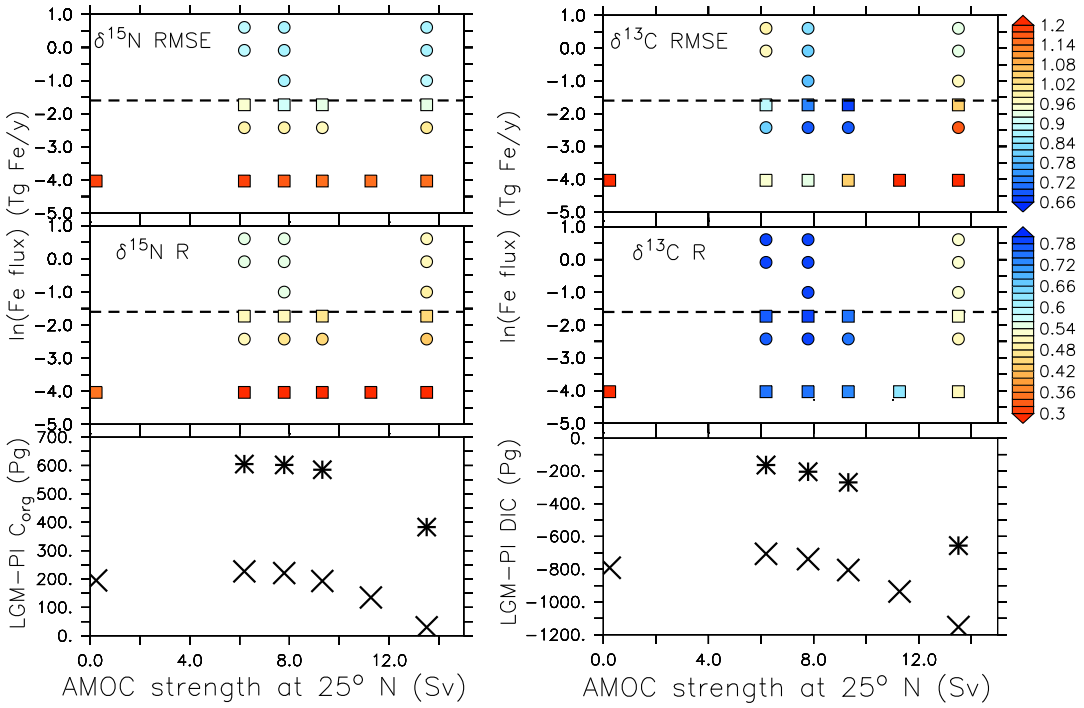


Figure 4.6: Top: $RMSE$ of modeled (left) $\delta^{15}$N and (right) $\delta^{13}$C compared to reconstructions, mapped over AMOC strength - logarithm of SO atmospheric soluble iron flux spaces. Squares correspond to the models described in the Experiments section. Circles are additional simulations performed with various increasing SO atmospheric soluble iron fluxes. Cold colors indicate better model-data agreement. The dashed line is the upper boundary estimate of LGM surface soluble iron fertilization from Conway et al. (2015). Center: Same as top, but for correlation coefficient $R$. Bottom: LGM-PI global (left) $C_{org}$ and (right) DIC versus AMOC strength from our described LGM simulations. Stars (crosses) represent models with (without) increased atmospheric soluble iron flux in the SO.

PI $\delta^{15}$N changes in the SO and elsewhere due to too much suboxia, water-column denitrification and nitrogen fixation, similar to experiments of (Schmittner and Somes, 2016) with globally increased phytoplankton growth rates.

In conclusion, our simulations suggest that in order to reproduce the combination of reconstructed LGM radiocarbon ages, $\delta^{13}$C of DIC and $\delta^{15}$N of organic matter, a weak, shallow NADW and a voluminous AABW, together with increased atmospheric iron fertilization in the SO, are needed. To our knowledge, this is the first time that these three properties are generated by a coupled physical-biogeochemical global ocean model that includes a prognostic iron cycle, and directly compared to LGM reconstructions. The estimated AMOC strength at 25° N is $6 - 9$ Sv and the IPMOC at 30° S is $12 - 13$ Sv

What implications did such a state have on the DIC pool of the glacial ocean? A weaker AMOC and far-reaching AABW produce higher accumulation of respired organic carbon ($C_{org}$) than a collapsed or strong circulation (Fig. 4.6), presumably maximizing during glacial states the amount of carbon stored in the deep ocean. Increasing export production through SO iron fertilization also raises $C_{org}$, in a larger magnitude than changing circulation, as previously shown by Brovkin et al. (2007); Tagliabue et al. (2009), and in contrast to recent suggestions that circulation changes can explain the whole glacial-interglacial change (Sarnthein et al., 2013).

Global mean LGM-PI $\Delta$DIC from our simulations are mostly negative (Table 4.1), because of the fixed 185 ppm atmospheric $CO_2$ applied to our ocean model, which forces it to equilibrate at lower carbon concentrations, and the lack

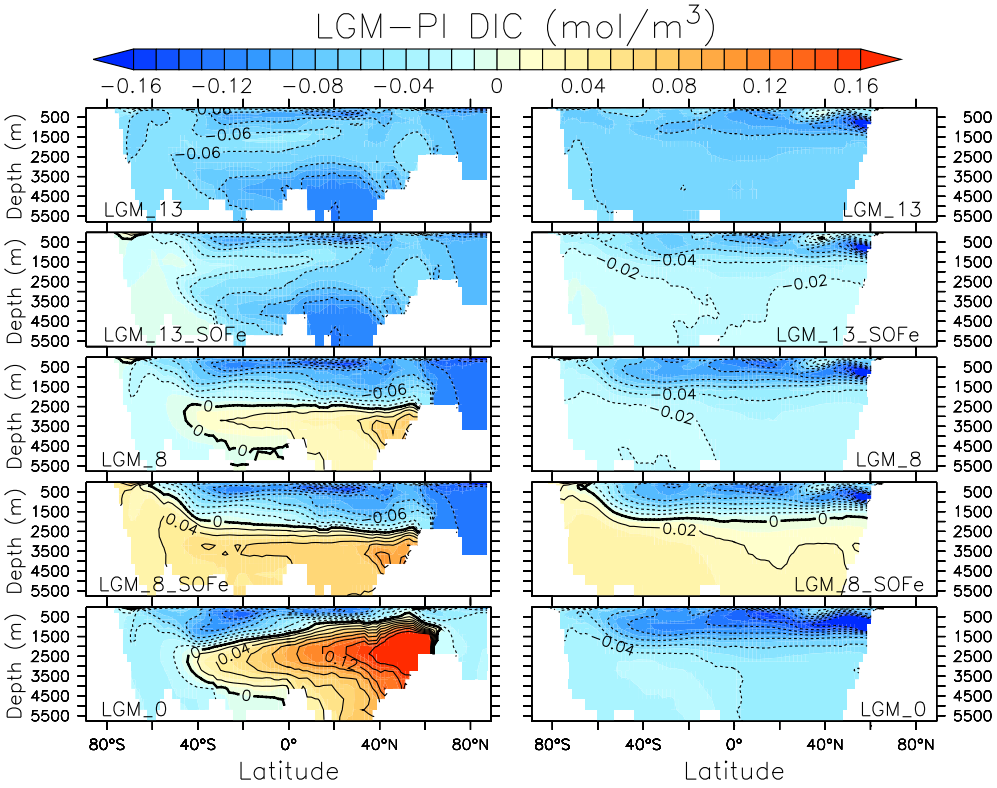


Figure 4.7: Zonal mean sections of LGM-PI DIC changes from some of our experiments, as indicated. Left(right) plots correspond to the Atlantic(Pacific) Ocean.

of changes in global alkalinity (Schmittner and Somes, 2016). A weak but stable AMOC and high SO iron fertilization produce higher global $\Delta$DIC than other configurations (Figs. 4.6, 4.7). LGM_8_SOFe and LGM_6_SOFe exhibit the highest ocean carbon content, and are also among the models that best reproduce isotope and radiocarbon fields. This provides strong evidence that a state of weak and shallow AMOC, together with increased SO export production, were both responsible of atmospheric $CO_2$ trapping in the deep ocean during glacial periods.

# Chapter 5: Conclusions

This thesis was focused on the understanding of the ocean circulation and biogeochemistry of the Last Glacial Maximum (LGM), and the roles they played in the sequestration of atmospheric carbon and its preservation in deep waters during that period. A work of such broad scope has to be approached in steps, so in each of the three chapters we focussed on different processes, with the goal of understanding them separately and then combining them.

In Chapter 2 we started our analysis by studying the LGM ocean circulation of models from the Paleoclimate Model Intercomparison Project 3 (PMIP3). These models exhibit an LGM Atlantic Meridional Overturning Circulation (AMOC) that is stronger, and generally deeper, that its preindustrial counterpart. Applying LGM wind stress anomalies from the PMIP3 models to the ocean component of the UVic model we find that stronger wind stress over the North Atlantic due to the effects of the Laurentide Ice Sheet on atmospheric circulation causes enhanced northward salt transport in an intensified gyre circulation. This produces a strengthening and deepening of the AMOC, consistent with PMIP3 model results. Wind stress over the North Atlantic is identified as a mechanism that delivers salt northward, and strengthens the LGM AMOC.

In Chapter 3 we focussed on the biogeochemistry of the LGM ocean, more precisely in the effects of changes in iron fluxes on the glacial carbon cycle. Our

results show that in LGM simulations, higher dust deposition and hydrothermanl flux increase dissolved iron (DFe) concentrations. On the other hand, lower sea level exposed a fraction of present day continental shelves in the LGM, reducing sedimentary DFe flux, and countering the other two processes. The changes in iron fluxes produce effects in global primary productivity, export production and deep remineralized organic carbon concentrations. However, the opposing effects of a sedimentary flux decrease and an atmospheric flux increase result in uncertainties in the magnitude and direction of changes to the carbon cycle. Only with an atmospheric DFe flux in the Southern Ocean of the order of 10 times its preindustrial value could the lower sedimentary flux be overcompensated and glacial export production increase, accumulating organic carbon in the deep ocean, triggering the sequestration of atmospheric $CO_2$.

In Chapter 4 we studied the effects of different circulations on ocean radiocarbon ages and stable isotope distributions in the LGM. We compared our model results to reconstructions of the same variables, in order to constrain the characteristics of the LGM ocean. Our simulations suggest that in order to reproduce the combination of reconstructed LGM radiocarbon ages and isotopes from sediment cores, a weak and shallow AMOC and a voluminous Antarctic Bottom Water (AABW) are needed. The weak AMOC is stabilized by the increased wind stress over the North Atlantic studied in Chapter 2. The agreement is improved when Southern Ocean atmospheric iron fertilization ($\sim$ 10 times its preindustrial value, as found in Chapter 3) is included. The weaker AMOC and far-reaching AABW, together with Southern Ocean iron fertilization, maximize accumulation of rem-

ineralized organic carbon in the deep ocean. Our results give evidence that a strong and deep AMOC, as PMIP3 models predict for the LGM, is infeasible to constrain isotope and radiocarbon reconstructions. A state of weak and shallow AMOC, together with increased Southern Ocean export production, must have been responsible of atmospheric $CO_2$ transfer to the deep ocean during glacial periods.

# APPENDICES

# Appendix A: Supplementary tables and figures for Chapter 2

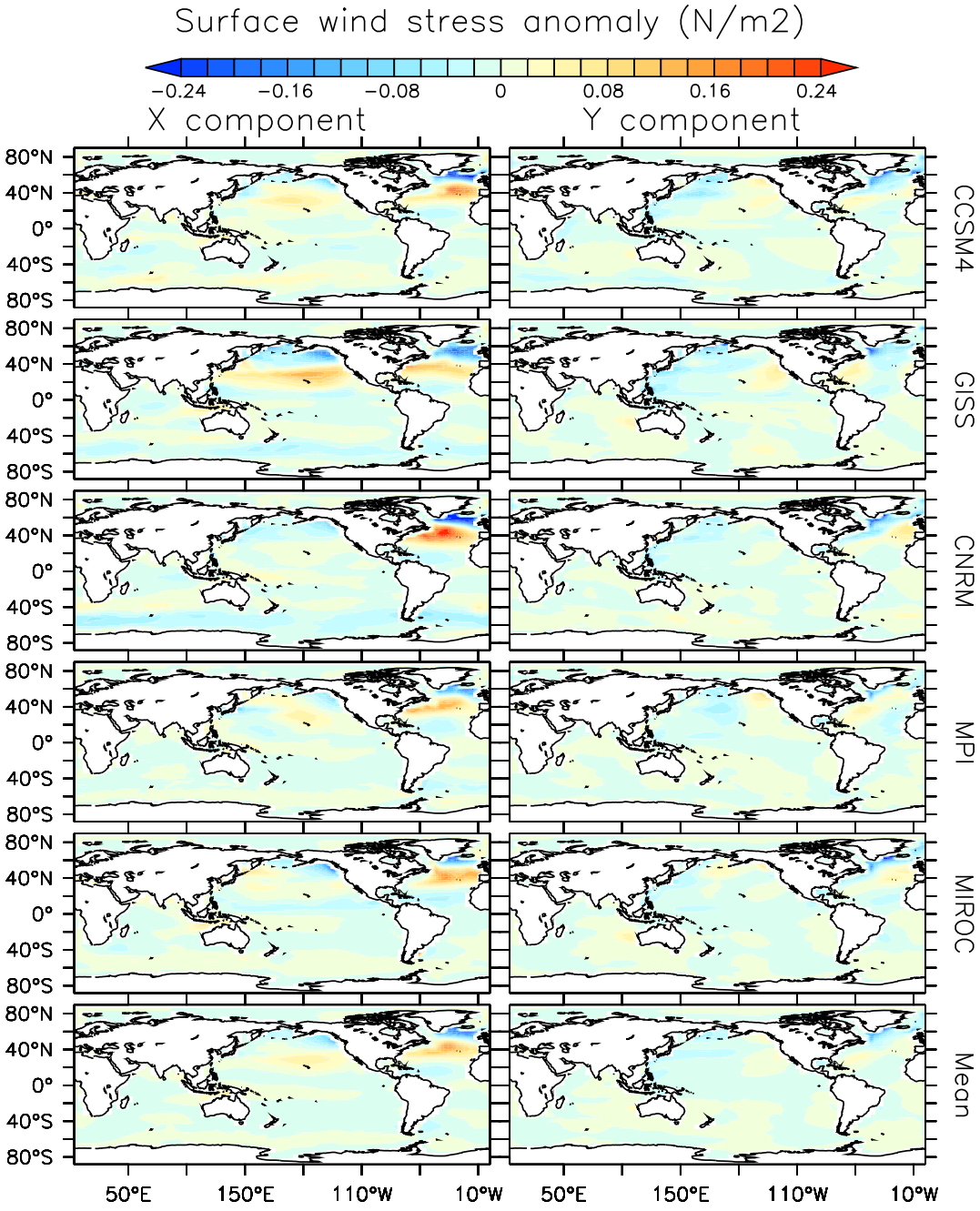


Figure A.1: Zonal and meridional wind stress LGM anomaly for some PMIP3 models, and the multi-model average.

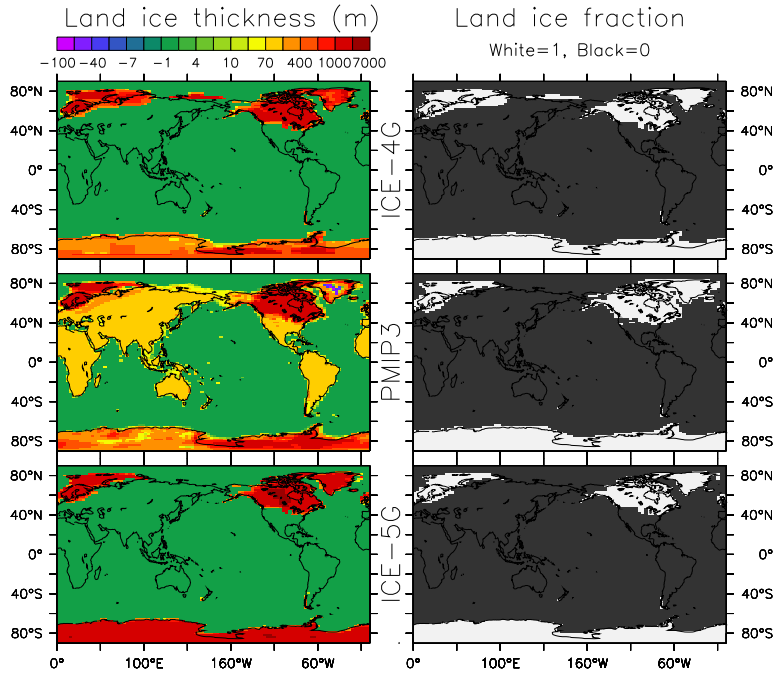


Figure A.2: Change in land ice thickness and fraction for each LGM reconstruction used in this work, as indicated. The reconstructions were re-gridded to the UVic model grid. Note that in the PMIP3 case, an addition of $20 - 70$ m is made to the topography across all continents, to account for the lower sea level during the LGM.

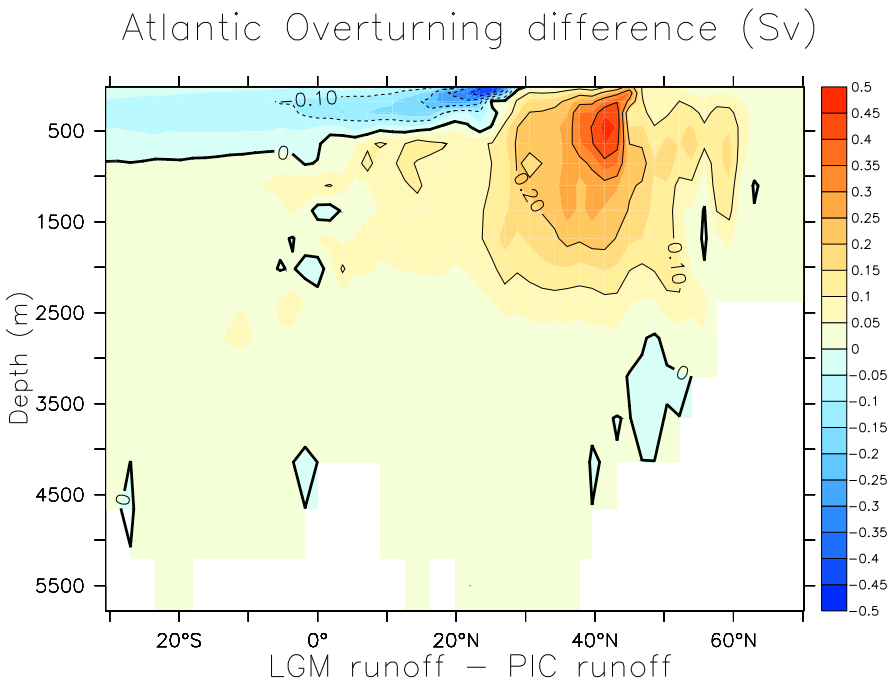


Figure A.3: Change in Atlantic meridional streamfunction $\psi(y, z)$ in the UVic model, between an LGM simulation with LGM river routing in North America, and an LGM simulation with modern river routing.

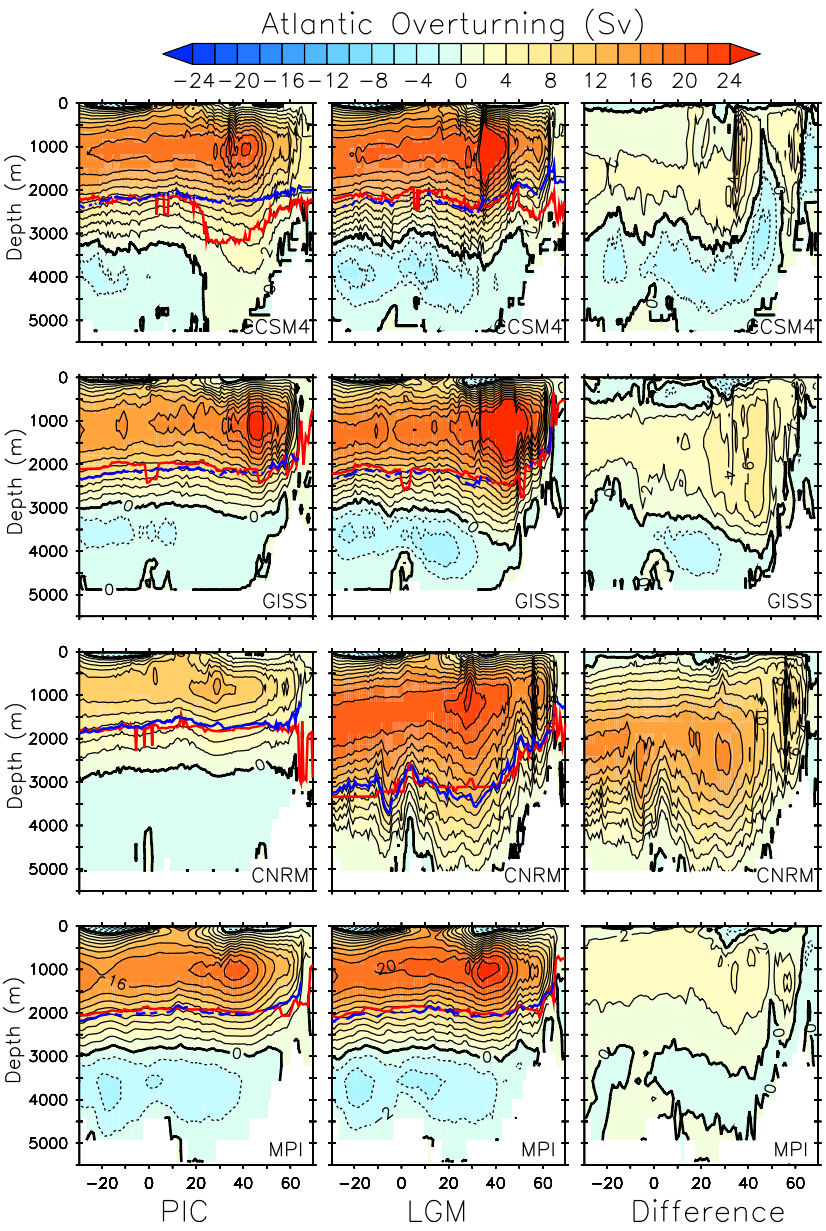


Figure A.4: Atlantic meridional streamfunction $\psi(y, z)$ calculated by PMIP3 models. Abscissa axes are in °N. First column corresponds to PIC simulations, middle to LGM, and third to the difference between them. Each row corresponds to a different PMIP3 model. Isoline difference is 4 Sv. Positive (negative) values correspond to clockwise (anti-clockwise) circulation. Red and blue lines are as in Fig. 1.1 of the main text.

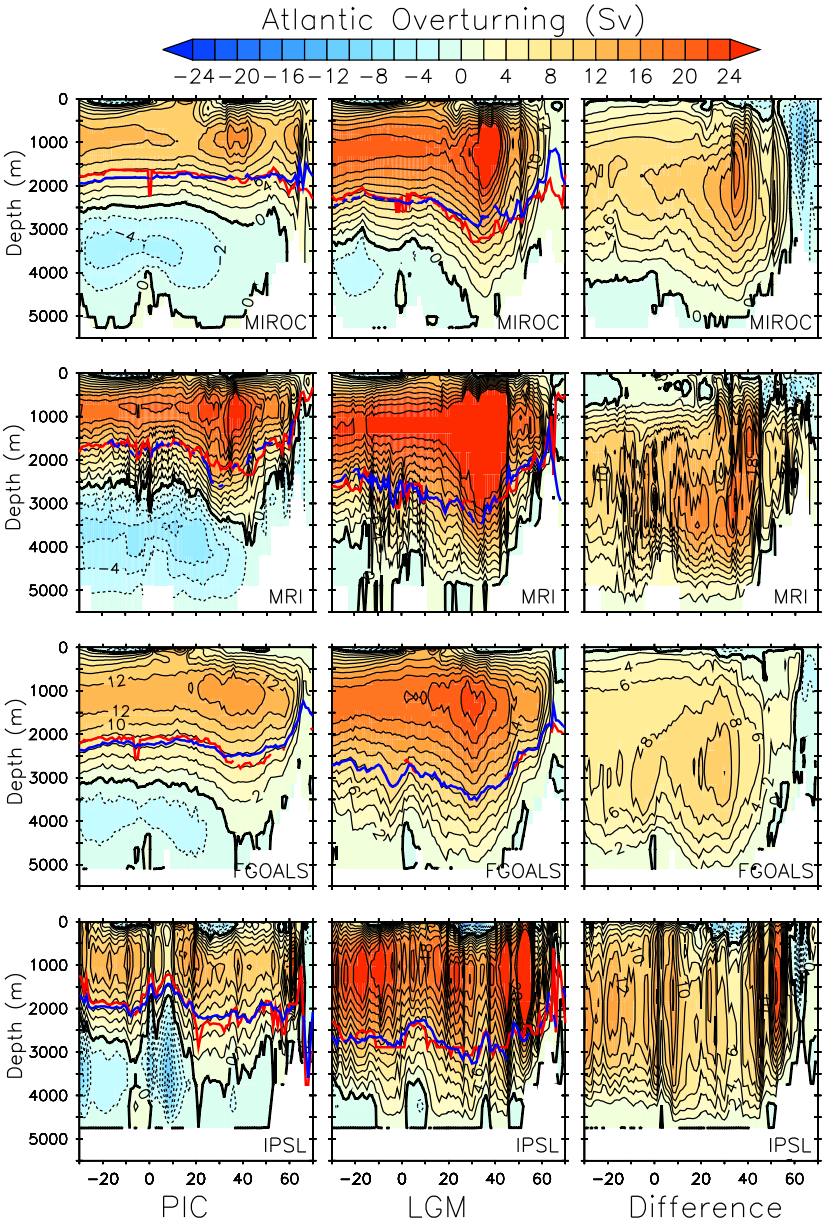


Figure A.5: Continuation of Fig. A.4

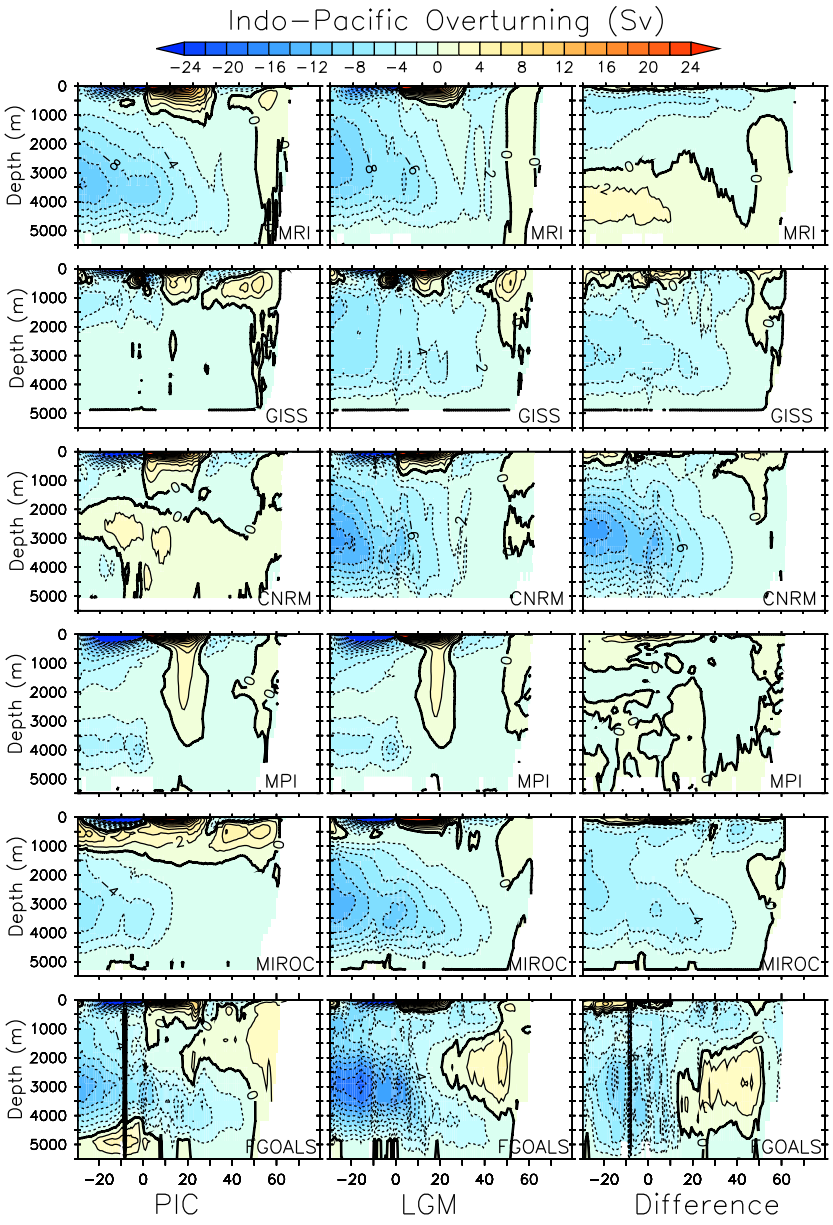


Figure A.6: Like Fig. A.3, but for the Indo-Pacific Ocean. CCSM4 and IPSL do not provide $\psi$ data for this basin.

Table A.1: Maximum meridional overturning, percentage of increment between wind stress experiments and the default run, and salt flux $F_{salt}$ in the Atlantic Ocean at 25°N in the UVic model experiments. Each row corresponds to wind stress anomalies from a different PMIP2 model, as indicated. The top row corresponds to the default case, where no anomalies were added to the background field.

| Model | AMOC (Sv) | Change (%) | $F_{salt}$ ($10^6$ kg/s) |
|---|---|---|---|
| Default | 11.27 | - | 51.32 |
| CCSM3 | 15.45 | 37 | 54.38 |
| MIROC | 12.19 | 08 | 62.17 |
| CNRM | 11.23 | 00 | 50.96 |
| FGOALS | 13.18 | 17 | 67.42 |

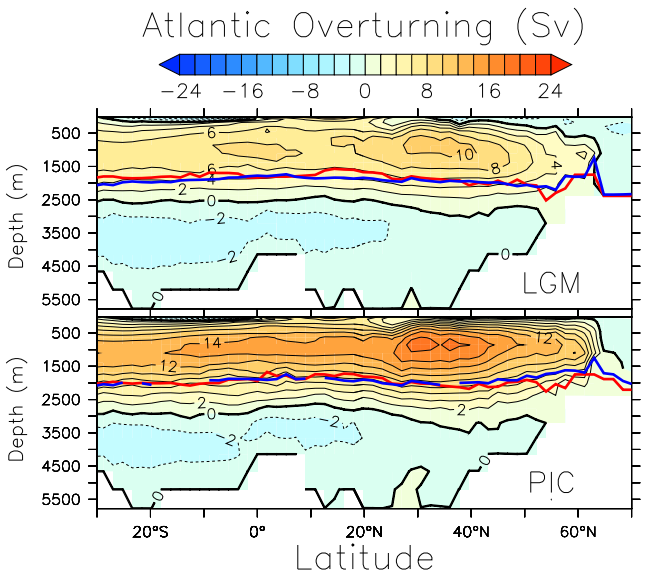


Figure A.7: Comparison between the default LGM and PIC Atlantic circulation in the UVic model. Top panel is Atltantic $\psi(y, z)$ for an equilibrium LGM simulation, and bottom panel is for a PIC simulation. The difference in the boundary conditions between the runs are atmospheric $CO_2$ levels, orbital parameters and continental ice sheets. Red and blue lines as in Fig. A.4.

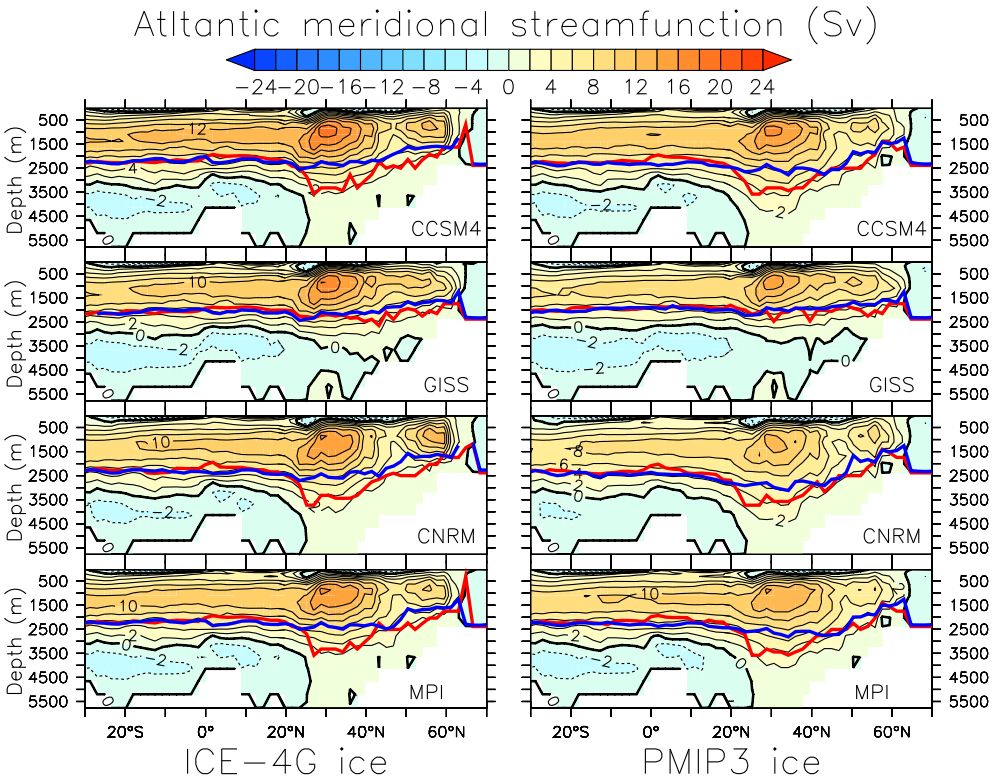


Figure A.8: LGM Atlantic meridional streamfunction calculated by the UVic Model. Left (right) column corresponds to runs made using the ICE-4G (PMIP3) LGM land ice reconstruction. Each case uses wind stress from NCEP reanalysis plus an LGM anomaly calculated from a different PMIP3 model, as indicated. Red and blue lines as in Fig. A.4.

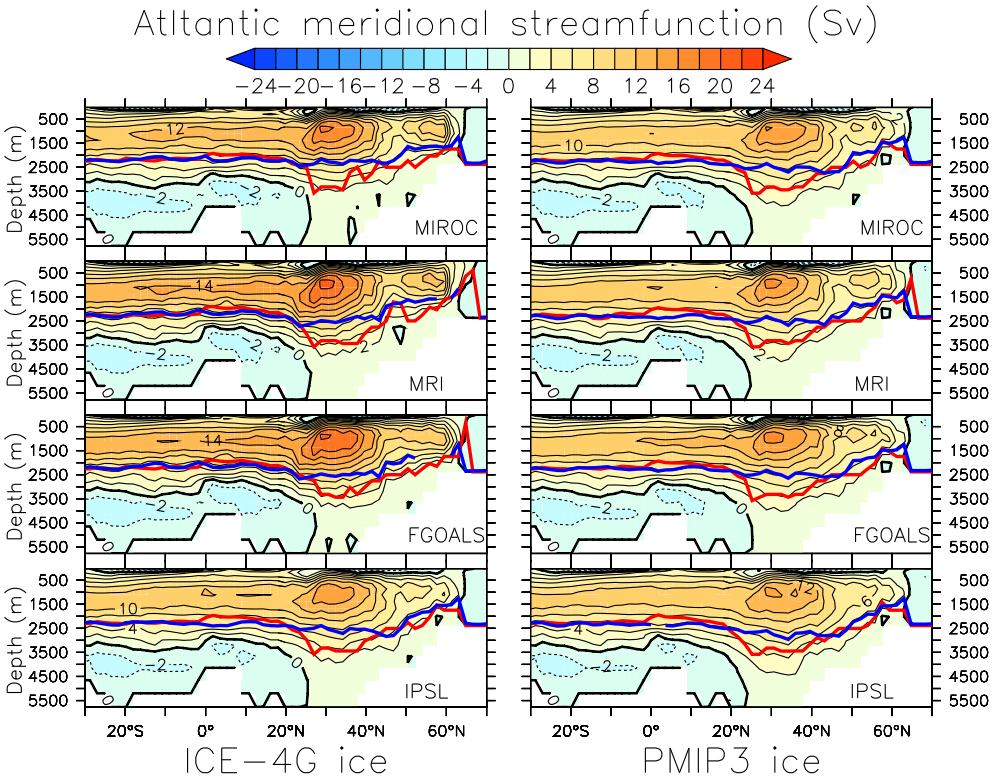


Figure A.9: Continuation of Figure A.8.

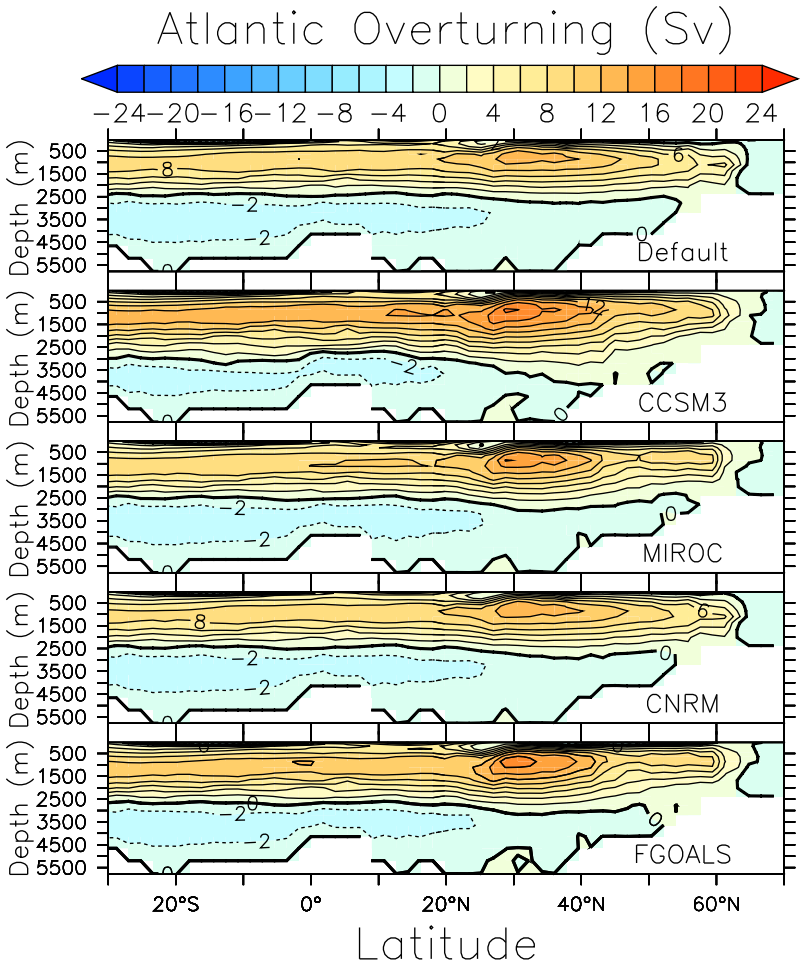


Figure A.10: LGM Atlantic meridional streamfunction calculated by the UVic model. The default case (top panel) uses a present-day wind stress pattern obtained from the NCEP reanalysis. The other cases use wind stress from NCEP reanalysis plus an LGM anomaly calculated from different PMIP2 models, as indicated.

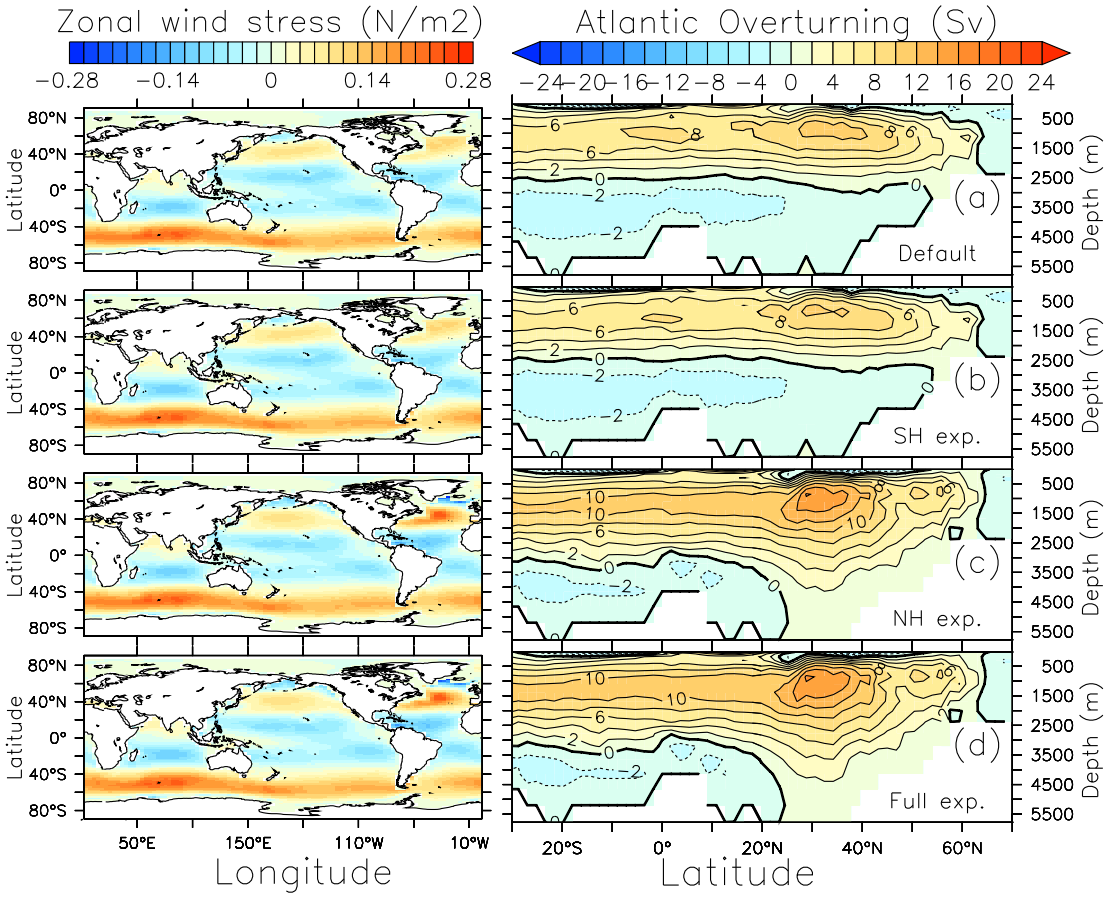


Figure A.11: Atlantic meridional streamfunction (left) and zonal surface wind stress fields (right) using a multi-model average of the wind stress anomalies in (a) neither of the hemispheres, (b) only in the Southern Hemisphere, (c) only in the Northern Hemisphere, and (d) in both hemispheres.

# Appendix B: Supplementary tables and figures for Chapter 4

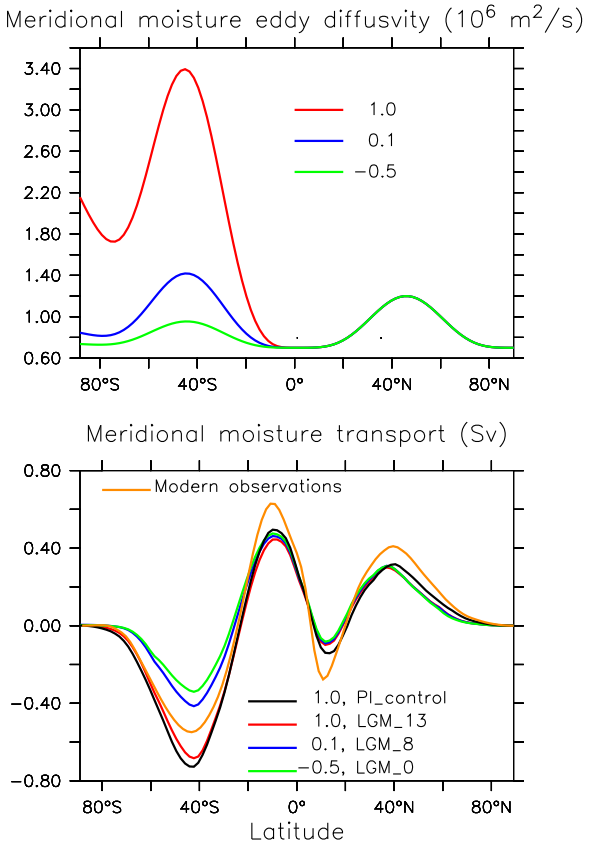


Figure B.1: Top: Meridional moisture eddy diffusivities used in some of our experiments. Each curve corresponds to a different $\epsilon_q$, the multiplying factor of the southern hemisphere anomaly $\mu_{SH}$. PI_control and LGM_13 use $\epsilon_q = 1$; LGM_8 uses $\epsilon_q = 0.1$; LGM_dqy-0.5 uses $\epsilon_q = -0.5$. We also have three intermediate experiments, LGM_11, LGM_9, and LGM_6, that use $\epsilon_q = 0.5$, $\epsilon_q = 0.25$, and $\epsilon_q = 0.0$, respectively, and were not included in the plot for the sake of simplicity. Bottom: Meridional moisture transports predicted by our experiments, indicated by their corresponding $\epsilon_q$ and the experiments' names. Using a lower moisture diffusivity in the southern hemisphere decreases the transport to almost half. The orange line is the ERA-Interim reanalysis modern prediction (Dee et al., 2011).

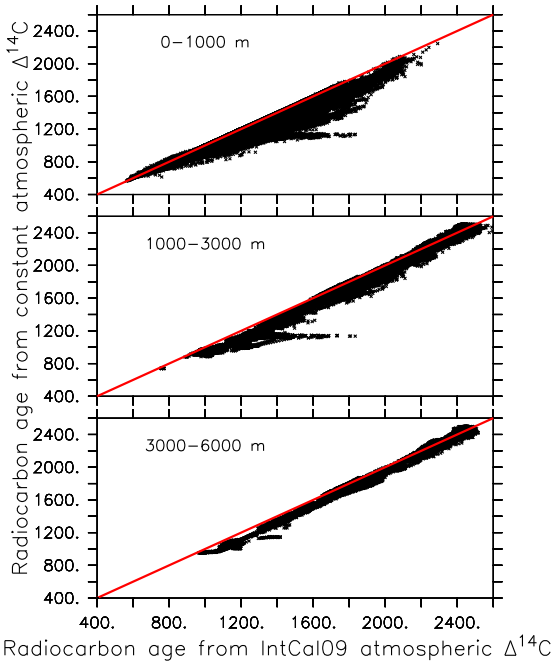


Figure B.2: Scatter plots of deep minus atmosphere radiocarbon ages, calculated from simulations using (x-axis) the variable IntCal09 $\Delta^{14}C_{atm}$ (Reimer et al., 2009) time series, and (y-axis) constant $\Delta^{14}C_{atm} = 0$. Three depth sections are shown, as indicated. The red lines correspond to the one to one line.

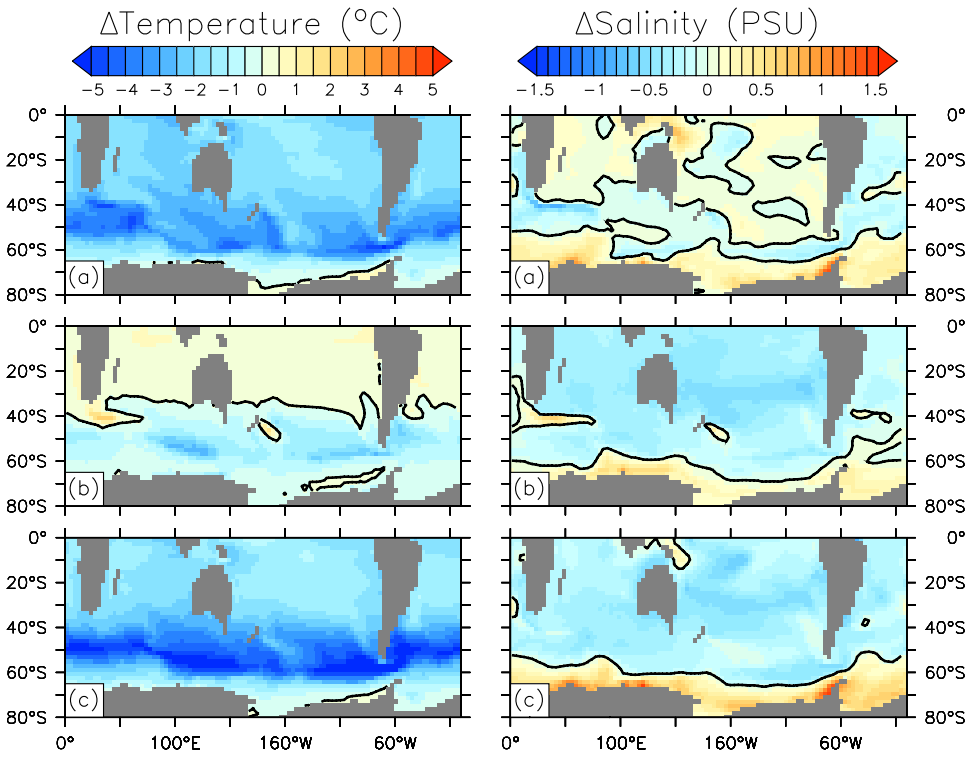


Figure B.3: Southern Hemisphere changes in surface (left) temperature and (right) salinity between different experiments. (a) LGM_13 - PI_control, (b) LGM_dqy8 - LGM_13, and (c) LGM_dqy8 - PI_control. The extra 1 PSU added in the LGM simulations has been subtracted from the plots.

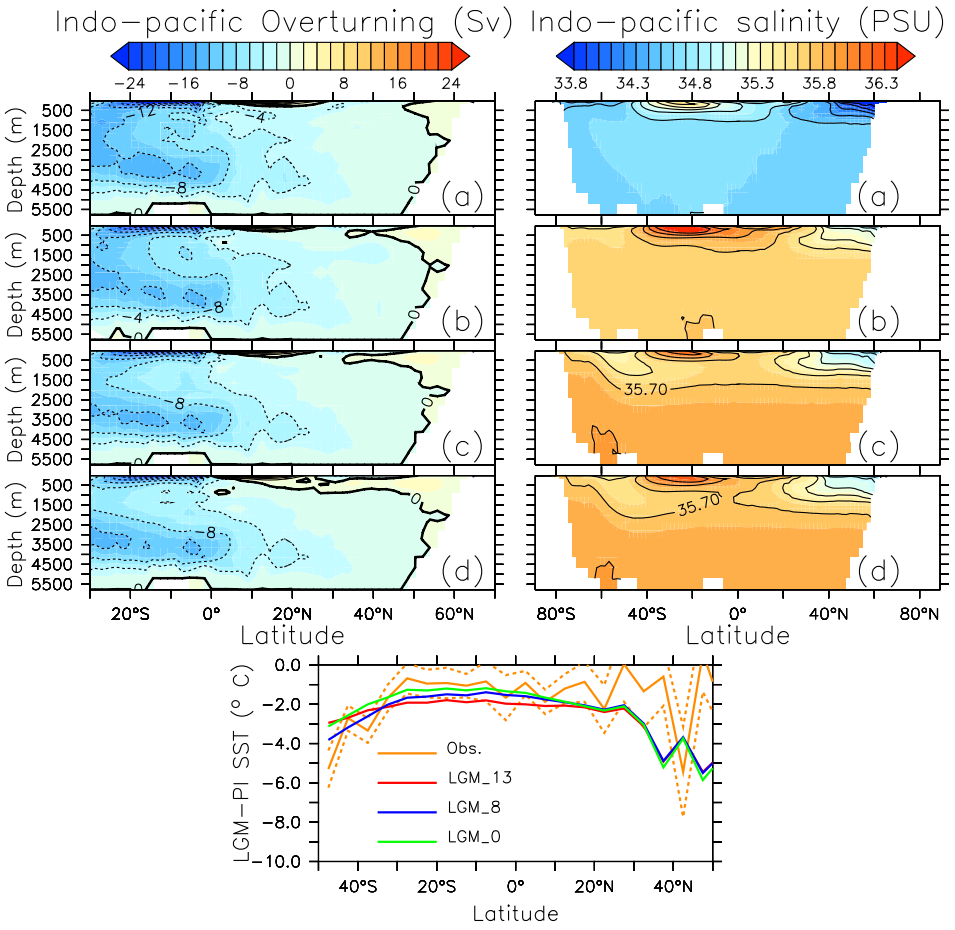


Figure B.4: Like Fig. 4.2 of the main text, but for the Indo-Pacific Ocean.

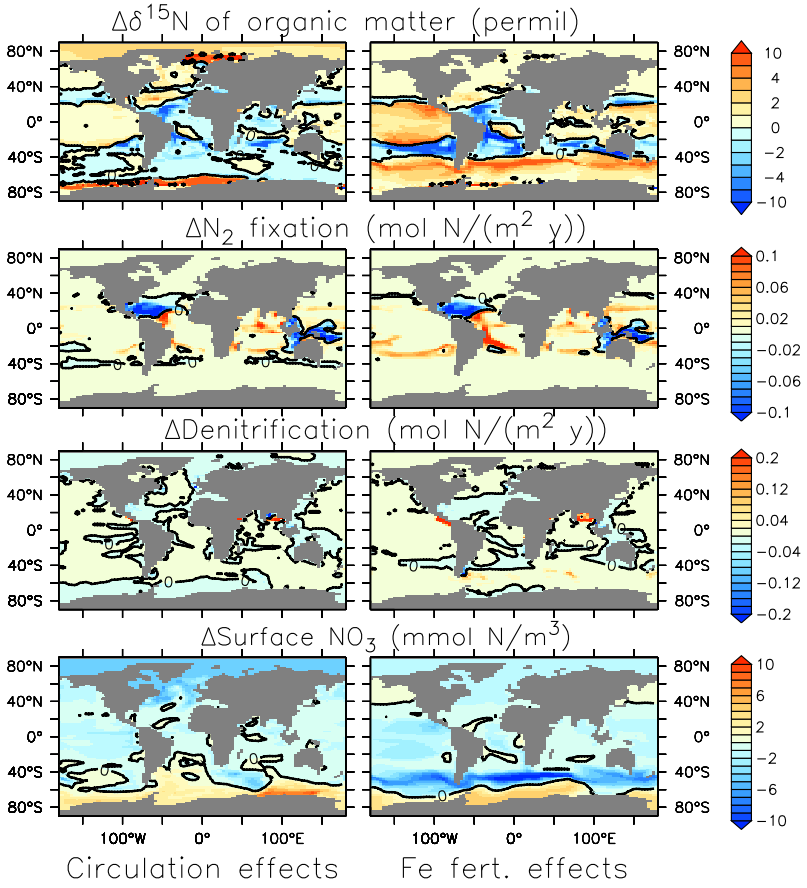


Figure B.5: Differences in top 120 m-averaged $\delta^{15}$N, top 120 m-integrated nitrogen fixation, whole water column-integrated denitrification, and top 120 m-averaged nitrate concentrations, as indicated, between (left) LGM_8 and LGM_13, and (right) LGM_13_SOFe and LGM_13. The plots isolate the circulation and SO Fe fertilization effects on the different nitrate variables and $\delta^{15}$N of organic matter. See Table 3 for global values of each experiment.

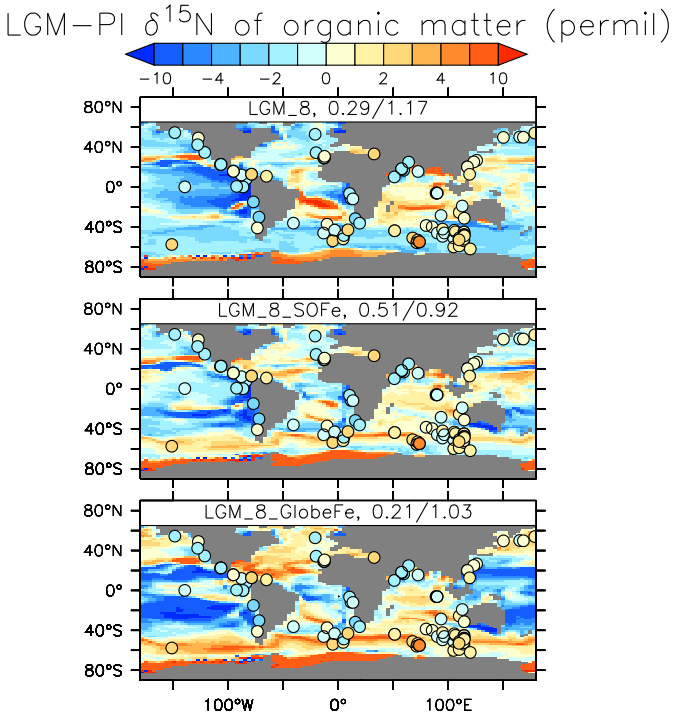


Figure B.6: LGM-PI changes in $\delta^{15}$N of detritus for experiments with different LGM atmospheric iron fluxes, as indicated by the labels above each map, which also contain the $R/RMSE$ parameters of the simulations compared to observations. LGM_8 uses an LGM atmospheric flux calculated from an LGM dust flux reconstruction (see Materials and Methods section and (Lambert et al., 2015)); LGM_8_SOFe uses the same LGM flux but multiplied by 10 in the SO, between Antarctica and 35° S; LGM_8_GlobeFe uses the LGM flux multiplied by 10 in the whole ocean. Overlaid on the plots are LGM-PI values from observations, from (Schmittner and Somes, 2016; Franois et al., 1997).

Table B.1: Multiplying factor of southern hemisphere moisture eddy diffusivity $\epsilon_q$, maximum transport (in Sv) of the AMOC at 25° N, of the Circumpolar Deep Water inflow into the Indian and Pacific Oceans at 35° S (IPMOC), global AABW, and ACC transport between Australia and Antarctica for our simulated physical states, as indicated. Numbers in parentheses indicate standard deviations in the last significant digit, taken from the last 500 y of the simulations. Using $\epsilon_q = -0.1$ or $\epsilon_q = -0.25$ produces the same circulation than using $\epsilon_q = -0.5$, and were not included in this paper to avoid redundancies.

| Experiment | $\epsilon_q$ | AMOC | IPMOC | AABW | ACC |
|---|---|---|---|---|---|
| PI_control | 1.0 | 17.8 | -15.5 | -16.2 | 120 |
| LGM_13 | 1.0 | 13.5 | -14.4 | -14.1 | 105 |
| LGM_11 | 0.5 | 11.3 | -12.9 | -15.8 | 125 |
| LGM_9 | 0.25 | 9.3 | -12.4 | -16.1 | 138 |
| LGM_8 | 0.1 | 7.8 | -12.4 | -16.8 | 148 |
| LGM_6 | 0.0 | 6.2 | -12.3 | -17.2 | 153 |
| LGM_0 | -0.5 | 0.2 | -12.7 | -17.9 | 152 |

Table B.2: Modeled global/deep (below 2000 m) mean LGM-PI radiocarbon ages (calculated over data locations only), and statistics $R/RMSE/RMSE'$ of modeled radiocarbon age, $\delta^{13}$C of DIC and LGM-PI $\Delta\delta^{15}$N of organic matter, compared to observational data. $R$ is the correlation coefficient, $RMSE$ is the root mean square error normalized by the models' standard deviations, and $RMSE'$ is the $RMSE$ of the anomalies from the mean. Observations of PI radiocarbon age and $\delta^{13}$C taken from Key et al. (2004) and Schmittner et al. (2013), respectively. LGM radiocarbon ages, $\delta^{13}$C, and $\Delta\delta^{15}$N data taken from Skinner et al. (2017), Peterson et al. (2014) and Schmittner and Somes (2016); Franois et al. (1997), respectively. Numbers in boldface represent best agreements with observations. Results were obtained after 5000 y of simulations, averaging over the last 500 y.

| Experiment | $^{14}$C age (y) | Age stats. | $\delta^{13}$C stats. | $\Delta\delta^{15}$N stats. |
|---|---|---|---|---|
| PI_control | - | 0.95/0.37/0.35 | 0.78/0.62/0.62 | - |
| LGM_13 | 283/281 | 0.49/1.57/1.39 | 0.50/1.64/1.00 | 0.29/1.14/0.96 |
| LGM_11 | 403/449 | 0.51/1.41/1.32 | 0.63/1.28/0.87 | 0.28/1.14/0.97 |
| LGM_9 | 525/658 | **0.54**/1.39/1.36 | 0.72/1.05/0.81 | 0.29/1.15/0.96 |
| LGM_8 | 602/790 | 0.53/1.34/1.33 | 0.76/0.93/0.83 | 0.29/1.17/0.96 |
| LGM_6 | 636/855 | 0.52/**1.33**/**1.33** | 0.74/0.94/0.91 | 0.29/1.20/0.96 |
| LGM_0 | 595/828 | 0.31/1.72/1.71 | -0.13/1.99/2.00 | 0.36/1.20/0.93 |
| LGM_13_SOFe | 283/281 | 0.49/1.57/1.39 | 0.52/1.05/0.88 | 0.45/0.93/0.89 |
| LGM_9_SOFe | 525/658 | **0.54**/1.39/1.36 | 0.75/**0.67**/0.66 | 0.48/**0.92**/0.88 |
| LGM_8_SOFe | 602/790 | 0.53/1.34/1.33 | **0.79**/0.73/**0.63** | **0.51**/**0.92**/0.91 |
| LGM_6_SOFe | 636/855 | 0.52/**1.33**/**1.33** | 0.78/0.89/0.68 | **0.51**/0.94/**0.86** |

Table B.3: Global mean nitrate concentration (in mmol/$m^3$), integrated nitrogen fixation, benthic and water column denitrification (all in Tg N/y), and global/SO export production out of the euphotic zone at 120 m (in Pg C/y) from our experiments.

| Experiment | $NO_3$ | $N_2$ fix. | B. deni. | W.C. deni. | Exp. prod. |
|---|---|---|---|---|---|
| PI_control | 29.2 | 242.90 | 99.75 | 146.2 | 8.37/2.23 |
| LGM_13 | 28.4 | 73.27 | 63.83 | 10.41 | 6.84/1.61 |
| LGM_11 | 29.4 | 76.42 | 63.22 | 14.71 | 6.65/1.55 |
| LGM_9 | 29.9 | 76.26 | 61.82 | 16.30 | 6.50/1.53 |
| LGM_8 | 30.3 | 74.56 | 59.96 | 16.47 | 6.37/1.52 |
| LGM_6 | 30.6 | 72.27 | 58.65 | 16.11 | 6.28/1.52 |
| LGM_0 | 30.7 | 65.26 | 60.73 | 10.01 | 6.46/1.57 |
| LGM_13_SOFe | 30.2 | 94.78 | 69.06 | 27.78 | 7.62/2.46 |
| LGM_9_SOFe | 30.5 | 93.56 | 65.29 | 34.03 | 6.96/2.27 |
| LGM_8_SOFe | 30.6 | 87.54 | 63.07 | 30.80 | 6.74/2.23 |
| LGM_6_SOFe | 30.8 | 81.93 | 61.62 | 27.30 | 6.61/2.23 |

# Bibliography

Abe-Ouchi, A., Saito, F., Kageyama, M., Braconnot, P., Harrison, S., Lambeck, K., Otto-Bliesner, B., Peltier, W., Tarasov, L., Peterschmitt, J.-Y., et al. (2015). Ice-sheet configuration in the CMIP5/PMIP3 Last Glacial Maximum experiments. *Geoscientfic Model Development*, *8*(6).

Adams, J. M., Faure, H., Faure-Denard, L., McGlade, J., and Woodward, F. (1990). Increases in terrestrial carbon storage from the last glacial maximum to the present. *Nature*, *348*(6303), 711–714.

Adkins, J. F., McIntyre, K., and Schrag, D. P. (2002). The salinity, temperature, and $\delta$18O of the glacial deep ocean. *Science*, *298*(5599), 1769–1773.

Albani, S., Mahowald, N., Perry, A., Scanza, R., Zender, C., Heavens, N., Maggi, V., Kok, J., and Otto-Bliesner, B. (2014). Improved dust representation in the community atmosphere model. *J. Adv. Model. Earth Sy.*, *6*(3), 541–570.

Archer, D., Winguth, A., Lea, D., and Mahowald, N. (2000). What caused the glacial/interglacial atmospheric pco2 cycles? *Reviews of Geophysics*, *38*(2), 159–189.

Bard, E. (1988). Correction of accelerator mass spectrometry 14c ages measured in planktonic foraminifera: paleoceanographic implications. *Paleoceanography*, *3*(6), 635–645.

Böhm, E., Lippold, J., Gutjahr, M., Frank, M., Blaser, P., Antz, B., Fohlmeister, J., Frank, N., Andersen, M., and Deininger, M. (2015). Strong and deep atlantic meridional overturning circulation during the last glacial cycle. *Nature*, *517*(7532), 73–76.

Bopp, L., Kohfeld, K. E., Le Quéré, C., and Aumont, O. (2003). Dust impact on marine biota and atmospheric CO2 during glacial periods. *Paleoceanography*, *18*(2).

Bouttes, N., Paillard, D., Roche, D. M., Brovkin, V., and Bopp, L. (2011). Last glacial maximum co2 and $\delta$13c successfully reconciled. *Geophysical Research Letters*, *38*(2).

Braconnot, P., Harrison, S. P., Kageyama, M., Bartlein, P. J., Masson-Delmotte, V., Abe-Ouchi, A., Otto-Bliesner, B., and Zhao, Y. (2012). Evaluation of climate models using palaeoclimatic data. *Nature Clim. Change*, *2*(6), 417–424.

Braconnot, P., Otto-Bliesner, B., Kageyama, M., Kitoh, A., Laîné, A., Loutre, M.-F., Marti, O., Merkel, U., Ramstein, G., Valdes, P., et al. (2007). Results of pmip2 coupled simulations of the mid-holocene and last glacial maximum–part 1: experiments and large-scale features. *Climate of the Past*, *3*, 261–277.

Broecker, W. S. (1982). Glacial to interglacial changes in ocean chemistry. *Progress in Oceanography*, *11*(2), 151–197.

Brovkin, V., Ganopolski, A., Archer, D., and Rahmstorf, S. (2007). Lowering of glacial atmospheric CO2 in response to changes in oceanic circulation and marine biogeochemistry. *Paleoceanography*, *22*(4).

Burckel, P., Waelbroeck, C., Luo, Y., Roche, D. M., Pichat, S., Jaccard, S. L., Gherardi, J., Govin, A., Lippold, J., and Thil, F. (2016). Changes in the geometry and strength of the atlantic meridional overturning circulation during the last glacial (20-50ka). *Climate of the Past*, *12*(11), 2061.

Clark, P. U., Dyke, A. S., Shakun, J. D., Carlson, A. E., Clark, J., Wohlfarth, B., Mitrovica, J. X., Hostetler, S. W., and McCabe, A. M. (2009). The last glacial maximum. *Science*, *325*(5941), 710–714.

Clark, P. U., Mitrovica, J., Milne, G., and Tamisiea, M. (2002). Sea-level fingerprinting as a direct test for the source of global meltwater pulse ia. *Science*, *295*(5564), 2438–2441.

Conway, T., Wolff, E., Röthlisberger, R., Mulvaney, R., and Elderfield, H. (2015). Constraints on soluble aerosol iron flux to the southern ocean at the last glacial maximum. *Nature communications*, *6*(7850).

Costa, K., McManus, J., Anderson, R., Ren, H., Sigman, D., Winckler, G., Fleisher, M., Marcantonio, F., and Ravelo, A. (2016). No iron fertilization in the equatorial pacific ocean during the last ice age. *Nature*, *529*(7587), 519–522.

Dale, A. W., Nickelsen, L., Scholz, F., Hensen, C., Oschlies, A., and Wallmann, K. (2015). A revised global estimate of dissolved iron fluxes from marine sediments. *Global Biogeochemical Cycles*, *29*(5), 691–707.

Dee, D., Uppala, S., Simmons, A., Berrisford, P., Poli, P., Kobayashi, S., Andrae, U., Balmaseda, M., Balsamo, G., Bauer, P., et al. (2011). The era-interim reanalysis: Configuration and performance of the data assimilation system. *Quarterly Journal of the royal meteorological society*, *137*(656), 553–597.

Duplessy, J.-C., Shackleton, N. J., Matthews, R. K., Prell, W., Ruddiman, W. F., Caralp, M., and Hendy, C. H. (1984). 13c record of benthic foraminifera in the last interglacial ocean: implications for the carbon cycle and the global deep water circulation. *Quaternary Research*, *21*(2), 225–243.

Elderfield, H., Ferretti, P., Greaves, M., Crowhurst, S., McCave, I., Hodell, D., and Piotrowski, A. (2012). Evolution of ocean temperature and ice volume through the mid-pleistocene climate transition. *Science*, *337*(6095), 704–709.

Elrod, V. A., Berelson, W. M., Coale, K. H., and Johnson, K. S. (2004). The flux of iron from continental shelf sediments: A missing source for global budgets. *Geophysical Research Letters*, *31*(12).

Fennel, K., Abbott, M. R., Spitz, Y. H., Richman, J. G., and Nelson, D. M. (2003). Impacts of iron control on phytoplankton production in the modern and glacial southern ocean. *Deep Sea Res. Pt. II*, *50*(3), 833–851.

Ferrari, R., Jansen, M. F., Adkins, J. F., Burke, A., Stewart, A. L., and Thompson, A. F. (2014). Antarctic sea ice control on ocean circulation in present and glacial climates. *Proceedings of the National Science Academy of the USA*, *111*(24), 8753–8758.

Franois, R., Altabet, M. A., Yu, E.-F., Sigman, D. M., Bacon, M. P., Frank, M., Bohrmann, G., Bareille, G., and Labeyrie, L. D. (1997). Contribution of southern ocean surface-water stratification to low atmospheric co2 concentrations during the last glacial period. *Nature*, *389*(6654), 929–935.

Freeman, E., Skinner, L., Waelbroeck, C., and Hodell, D. (2016). Radiocarbon evidence for enhanced respired carbon storage in the atlantic at the last glacial maximum. *Nature Communications*.

Galbraith, E. D., Gnanadesikan, A., Dunne, J. P., and Hiscock, M. R. (2010). Regional impacts of iron-light colimitation in a global biogeochemical model. *Biogeosciences*, *7*(3), 1043–1064.

Galbraith, E. D., Kwon, E. Y., Bianchi, D., Hain, M. P., and Sarmiento, J. L. (2015). The impact of atmospheric pco2 on carbon isotope ratios of the atmosphere and ocean. *Global Biogeochemical Cycles*, *29*(3), 307–324.

Gebbie, G. (2014). How much did glacial North Atlantic Water shoal? *Paleoceanography*, *29*(3), 190–209.

Getzlaff, J., and Dietze, H. (2013). Effects of increased isopycnal diffusivity mimicking the unresolved equatorial intermediate current system in an earth system climate model. *Geophysical Research Letters*, *40*(10), 2166–2170.

Gherardi, J.-M., Labeyrie, L., Nave, S., Francois, R., McManus, J. F., and Cortijo, E. (2009). Glacial-interglacial circulation changes inferred from 231Pa/230Th sedimentary record in the North Atlantic region. *Paleoceanography*, *24*(2).

Gledhill, M., and Buck, K. N. (2012). The organic complexation of iron in the marine environment: a review. *Front. Microbiol.*, *3*, 1–17.

Godwin, H. (1962). Half-life of radiocarbon. *Nature*, *195*.

Goodwin, P., and Lauderdale, J. M. (2013). Carbonate ion concentrations, ocean carbon storage, and atmospheric co2. *Global Biogeochemical Cycles*, *27*(3), 882–893.

Harrison, S. P., and Prentice, C. I. (2003). Climate and co2 controls on global vegetation distribution at the last glacial maximum: analysis based on palaeovegetation data, biome modelling and palaeoclimate simulations. *Global Change Biology*, *9*(7), 983–1004.

Hays, J. D., Imbrie, J., Shackleton, N. J., et al. (1976). Variations in the earth's orbit: pacemaker of the ice ages. vol. 194, (pp. 1121–1132).

Hu, A., Meehl, G. A., Otto-Bliesner, B. L., Waelbroeck, C., Han, W., Loutre, M.-F., Lambeck, K., Mitrovica, J. X., and Rosenbloom, N. (2010). Influence of bering strait flow and north atlantic circulation on glacial sea-level changes. *Nature Geoscience*, *3*(2), 118–121.

Insua, T. L., Spivack, A. J., Graham, D., D'Hondt, S., and Moran, K. (2014). Reconstruction of Pacific Ocean bottom water salinity during the Last Glacial Maximum. *Geophysical Research Letters*, *41*(8), 2914–2920.

Ito, T., and Follows, M. J. (2005). Preformed phosphate, soft tissue pump and atmospheric co2. *Journal of Marine Research*, *63*(4), 813–839.

Jickells, T., An, Z., Andersen, K. K., Baker, A., Bergametti, G., Brooks, N., Cao, J., Boyd, P., Duce, R., Hunter, K., et al. (2005). Global iron connections between desert dust, ocean biogeochemistry, and climate. *Science*, *308*(5718), 67–71.

Kalnay, E., Kanamitsu, M., Kistler, R., Collins, W., Deaven, D., Gandin, L., Iredell, M., Saha, S., White, G., Woollen, J., et al. (1996). The NCEP/NCAR reanalysis 40-year project. *Bull. Am. Meteorol. Soc*, *77*(3), 437–471.

Key, R. M., Kozyr, A., Sabine, C. L., Lee, K., Wanninkhof, R., Bullister, J. L., Feely, R. A., Millero, F. J., Mordy, C., and Peng, T.-H. (2004). A global ocean carbon climatology: Results from global data analysis project (glodap). *Global Biogeochemical Cycles*, *18*(4).

Khatiwala, S., Primeau, F., and Holzer, M. (2012). Ventilation of the deep ocean constrained with tracer observations and implications for radiocarbon estimates of ideal mean age. *Earth and Planetary Science Letters*, *325*, 116–125.

Kohfeld, K. E., Le Quéré, C., Harrison, S. P., and Anderson, R. F. (2005). Role of marine biology in glacial-interglacial CO2 cycles. *Science*, *308*(5718), 74–78.

Kuhlbrodt, T., Griesel, A., Montoya, M., Levermann, A., Hofmann, M., and Rahmstorf, S. (2007). On the driving processes of the Atlantic meridional overturning circulation. *Rev. of Geophys.*, *45*(2).

Kurahashi-Nakamura, T., Paul, A., and Losch, M. (2017). Dynamical reconstruction of the global ocean state during the last glacial maximum. *Paleoceanography*.

Lambeck, K., Rouby, H., Purcell, A., Sun, Y., and Sambridge, M. (2014). Sea level and global ice volumes from the Last Glacial Maximum to the Holocene. *Proceedings of the National Academy of Sciences*, *111*(43), 15296–15303.

Lambert, F., Tagliabue, A., Shaffer, G., Lamy, F., Winckler, G., Farias, L., Gallardo, L., Pol-Holz, D., et al. (2015). Dust fluxes and iron fertilization in Holocene and Last Glacial Maximum climates. *Geophysical Research Letters*, *42*(14), 6014–6023.

Levitus, S., Antonov, J., Baranova, O. K., Boyer, T., Coleman, C., Garcia, H., Grodsky, A., Johnson, D., Locarnini, R., Mishonov, A. V., et al. (2013). The world ocean database. *Data Science Journal*, *12*(0), WDS229–WDS234.

Lippold, J., Luo, Y., Francois, R., Allen, S. E., Gherardi, J., Pichat, S., Hickey, B., and Schulz, H. (2012). Strength and geometry of the glacial atlantic meridional overturning circulation. *Nature Geoscience*, *5*(11), 813–816.

Lund, D., Asimow, P., Farley, K., Rooney, T., Seeley, E., Jackson, E., and Durham, Z. (2016). Enhanced east pacific rise hydrothermal activity during the last two glacial terminations. *Science*, *351*(6272), 478–482.

Luo, C., Mahowald, N., Bond, T., Chuang, P., Artaxo, P., Siefert, R., Chen, Y., and Schauer, J. (2008). Combustion iron distribution and deposition. *Global Biogeochemical Cycles*, *22*(1).

Lynch-Stieglitz, J., Adkins, J. F., Curry, W. B., Dokken, T., Hall, I. R., Herguera, J. C., Hirschi, J. J.-M., Ivanova, E. V., Kissel, C., Marchal, O., et al. (2007). Atlantic meridional overturning circulation during the Last Glacial Maximum. *Science*, *316*(5821), 66–69.

Lynch-Stieglitz, J., Curry, W. B., and Slowey, N. (1999). Weaker Gulf Stream in the Florida straits during the last glacial maximum. *Nature*, *402*(6762), 644–648.

Lynch-Stieglitz, J., Ito, T., and Michel, E. (2016). Antarctic density stratification and the strength of the circumpolar current during the Last Glacial Maximum. *Paleoceanography*.

Maher, B., Prospero, J., Mackie, D., Gaiero, D., Hesse, P., and Balkanski, Y. (2010). Global connections between aeolian dust, climate and ocean biogeochemistry at the present day and at the last glacial maximum. *Earth-Science Reviews*, *99*(1), 61–97.

Mahowald, N. M., Engelstaedter, S., Luo, C., Sealy, A., Artaxo, P., Benitez-Nelson, C., Bonnet, S., Chen, Y., Chuang, P. Y., Cohen, D. D., et al. (2009). Atmospheric iron deposition: Global Distribution, Variability, and Human Perturbations*. *Annual Review of Marine Science*, *1*, 245–278.

Marcott, S. A., Bauska, T. K., Buizert, C., Steig, E. J., Rosen, J. L., Cuffey, K. M., Fudge, T., Severinghaus, J. P., Ahn, J., Kalk, M. L., McConnell, J. R., Sowers, T., Taylor, K. C., White, J. W. C., and J, B. E. (2014). Centennial-scale changes in the global carbon cycle during the last deglaciation. *Nature*, *514*(7524), 616–619.

Martin, J. H. (1990). Glacial-interglacial CO2 change: The iron hypothesis. *Paleoceanography*, *5*(1), 1–13.

Martínez-García, A., Sigman, D. M., Ren, H., Anderson, R. F., Straub, M., Hodell, D. A., Jaccard, S. L., Eglinton, T. I., and Haug, G. H. (2014). Iron fertilization of the Subantarctic Ocean during the last ice age. *Science*, *343*(6177), 1347–1350.

McCarthy, G., Smeed, D., Johns, W., Frajka-Williams, E., Moat, B., Rayner, D., Baringer, M., Meinen, C., Collins, J., and Bryden, H. (2015). Measuring the atlantic meridional overturning circulation at 26 n. *Progress in Oceanography*, *130*, 91–111.

McManus, J., Francois, R., Gherardi, J.-M., Keigwin, L., and Brown-Leger, S. (2004). Collapse and rapid resumption of Atlantic meridional circulation linked to deglacial climate changes. *Nature*, *428*(6985), 834–837.

Meissner, K., Weaver, A., Matthews, H., and Cox, P. (2003). The role of land surface dynamics in glacial inception: a study with the Uvic Earth System Model. *Climate Dynamics*, *21*(7-8), 515–537.

Menviel, L., Mouchet, A., Meissner, K., Joos, F., and England, M. (2015). Impact of oceanic circulation changes on atmospheric $\delta$13co2. *Global Biogeochemical Cycles*, *29*(11), 1944–1961.

Menviel, L., Yu, J., Joos, F., Mouchet, A., Meissner, K., and England, M. (2017). Poorly ventilated deep ocean at the last glacial maximum inferred from carbon isotopes: A data-model comparison study. *Paleoceanography*, *32*(1), 2–17.

Middleton, J. L., Langmuir, C. H., Mukhopadhyay, S., McManus, J. F., and Mitrovica, J. X. (2016). Hydrothermal iron flux variability following rapid sea level changes. *Geophysical Research Letters*, *43*(8), 3848–3856.

Miller, M. D., Simons, M., Adkins, J. F., and Minson, S. E. (2015). The information content of pore fluid $\delta$ 18O and [cl-]. *Journal of Physical Oceanography*, *45*(8), 2070–2094.

Molina-Kescher, M., Frank, M., Tapia, R., Ronge, T. A., Nürnberg, D., and Tiedemann, R. (2016). Reduced admixture of north atlantic deep water to the deep central south pacific during the last two glacial periods. *Paleoceanography*, *31*(6), 651–668.

Mongin, M., Nelson, D. M., Pondaven, P., and Tréguer, P. (2007). Potential phytoplankton responses to iron and stratification changes in the southern ocean based on a flexible-composition phytoplankton model. *Global Biogeochemical Cycles*, *21*(4).

Montoya, M., and Levermann, A. (2008). Surface wind-stress threshold for glacial atlantic overturning. *Geophysical Research Letters*, *35*(3).

Moore, J. K., Abbott, M. R., Richman, J. G., and Nelson, D. M. (2000a). The southern ocean at the last glacial maximum: A strong sink for atmospheric carbon dioxide. *Global Biogeochemical Cycles*, *14*(1), 455–475.

Moore, J. K., Abbott, M. R., Richman, J. G., and Nelson, D. M. (2000b). The southern ocean at the last glacial maximum: A strong sink for atmospheric carbon dioxide. *Global Biogeochemical Cycles*, *14*(1), 455–475.

Muglia, J., and Schmittner, A. (2015). Glacial Atlantic overturning increased by wind stress in climate models. *Geophysical Research Letters*, *42*(22), 9862–9868.

Muglia, J., Somes, C. J., Nickelsen, L., and Schmittner, A. (submitted). Combined effects of atmospheric and seafloor iron fluxes to the glacial ocean. *Paleoceanography*.

National Geophysical Data Center (2006). 2-minute gridded global relief data (ETOPO2v2).

Nickelsen, L. (2015). *Modelling the marine biogeochemical implications of aeolian, sedimentary and riverine iron supply*. Ph.D. thesis, Christian-Albrechts Universität Kiel.

Nickelsen, L., Keller, D., and Oschlies, A. (2015). A dynamic marine iron cycle module coupled to the University of Victoria Earth System Model: the Kiel Marine Biogeochemical Model 2 for UVic 2.9. *Geoscientific Model Development*, *8*, 1357–1381.

Nickelsen, L., and Oschlies, A. (2015). Enhanced sensitivity of oceanic co2 uptake to dust deposition by iron-light colimitation. *Geophysical Research Letters*, *42*(2), 492–499.

Oka, A., Hasumi, H., and Abe-Ouchi, A. (2012). The thermal threshold of the Atlantic meridional overturning circulation and its control by wind stress forcing during glacial climate. *Geophysical Research Letters*, *39*(9).

Otto-Bliesner, B., Hewitt, C., Marchitto, T., Brady, E., Abe-Ouchi, A., Crucifix, M., Murakami, S., and Weber, S. (2007). Last glacial maximum ocean thermohaline circulation: PMIP2 model intercomparisons and data constraints. *Geophysical Research Letters*, *34*(12).

Otto-Bliesner, B. L., Brady, E. C., Clauzet, G., Tomas, R., Levis, S., and Kothavala, Z. (2006). Last glacial maximum and Holocene climate in CCSM3. *Journal of Climate*, *19*(11), 2526–2544.

Palastanga, V., Slomp, C., and Heinze, C. (2013). Glacial-interglacial variability in ocean oxygen and phosphorus in a global biogeochemical model. *Biogeosciences*, *10*(2), 945–958.

Parekh, P., Follows, M. J., and Boyle, E. (2004). Modeling the global ocean iron cycle. *Global Biogeoch. Cy.*, *18*(1).

Parekh, P., Joos, F., and Mueller, S. A. (2008). A modeling assessment of the interplay between aeolian iron fluxes and iron-binding ligands in controlling carbon dioxide fluctuations during Antarctic warm events. *Paleoceanography*, *23*(4).

Peltier, W. (2004). Global glacial isostasy and the surface of the ice-age earth: the ice-5g (vm2) model and grace. *Annu. Rev. Earth Planet. Sci.*, *32*, 111–149.

Peltier, W., Argus, D., and Drummond, R. (2015). Space geodesy constrains ice age terminal deglaciation: The global ice-6g_c (vm5a) model. *J. Geophys. Res.-Sol. Ea.*, *120*(1), 450–487.

Peltier, W. R. (1994). Ice age paleotopography. *Science-New York then Washington-*, (pp. 195–195).

Peterson, C. D., Lisiecki, L. E., and Stern, J. V. (2014). Deglacial whole-ocean $\delta$13c change estimated from 480 benthic foraminiferal records. *Paleoceanography*, *29*(6), 549–563.

Petit, J.-R., Jouzel, J., Raynaud, D., Barkov, N. I., Barnola, J.-M., Basile, I., Bender, M., Chappellaz, J., Davis, M., Delaygue, G., et al. (1999). Climate and atmospheric history of the past 420,000 years from the vostok ice core, antarctica. *Nature*, *399*(6735), 429–436.

Ramsey, C. B., Staff, R. A., Bryant, C. L., Brock, F., Kitagawa, H., van der Plicht, J., Schlolaut, G., Marshall, M. H., Brauer, A., Lamb, H. F., et al. (2012).

A complete terrestrial radiocarbon record for 11.2 to 52.8 kyr bp. *Science*, *338*(6105), 370–374.

Reimer, P. J., Baillie, M. G., Bard, E., Bayliss, A., Beck, J. W., Blackwell, P. G., Ramsey, C. B., Buck, C. E., Burr, G. S., Edwards, R. L., et al. (2009). Intcal09 and marine09 radiocarbon age calibration curves, 0–50,000 years cal bp. *Radiocarbon*, *51*(04), 1111–1150.

Resing, J. A., Sedwick, P. N., German, C. R., Jenkins, W. J., Moffett, J. W., Sohst, B. M., and Tagliabue, A. (2015). Basin-scale transport of hydrothermal dissolved metals across the south pacific ocean. *Nature*, *523*(7559), 200–203.

Saenko, O. A., Weaver, A. J., and Schmittner, A. (2003). Atlantic deep circulation controlled by freshening in the Southern Ocean. *Geophysical Research Letters*, *30*(14).

Sarnthein, M., Schneider, B., and Grootes, P. M. (2013). Peak glacial 14c ventilation ages suggest major draw-down of carbon into the abyssal ocean. *Climate of the Past*, *9*(6), 2595–2614.

Schmittner, A. (2003). Southern ocean sea ice and radiocarbon ages of glacial bottom waters. *Earth and Planetary Science Letters*, *213*(1), 53–62.

Schmittner, A., and Egbert, G. (2013). An improved parameterization of tidal mixing for ocean models. *Geoscientific Model Development*, *7*, 211–224.

Schmittner, A., and Galbraith, E. D. (2008). Glacial greenhouse-gas fluctuations controlled by ocean circulation changes. *Nature*, *456*(7220), 373–376.

Schmittner, A., Green, J., and Wilmes, S. (2015). Glacial ocean over-turning intensified by tidal mixing in a global circulation model. *Geophysical Research Letters*, *42*, 2.

Schmittner, A., Gruber, N., Mix, A., Key, R., Tagliabue, A., and Westberry, T. (2013). Biology and air–sea gas exchange controls on the distribution of carbon isotope ratios ($\delta$ 13 c) in the ocean. *Biogeosciences*, *10*(9), 5793–5816.

Schmittner, A., and Somes, C. J. (2016). Complementary constraints from carbon (13c) and nitrogen (15n) isotopes on the glacial ocean's soft-tissue biological pump. *Paleoceanography*, *31*(6), 669–693.

Shackleton, N. (1977). Carbon 13 in uvigerina: Tropical rainforest history and the equatorial pacific carbonate dissolution cycles. *Marine science*.

Sholkovitz, E. R., Sedwick, P. N., Church, T. M., Baker, A. R., and Powell, C. F. (2012). Fractional solubility of aerosol iron: Synthesis of a global-scale data set. *Geochim. Cosmochim. Ac.*, *89*, 173–189.

Sigman, D. M., and Boyle, E. A. (2000). Glacial/interglacial variations in atmospheric carbon dioxide. *Nature*, *407*(6806), 859–869.

Sigman, D. M., De Boer, A. M., and Haug, G. H. (2007). Antarctic stratification, atmospheric water vapor, and heinrich events: A hypothesis for late pleistocene deglaciations. *Ocean Circulation: Mechanisms and Impacts-Past and Future Changes of Meridional Overturning*, (pp. 335–349).

Sigman, D. M., Hain, M. P., and Haug, G. H. (2010). The polar ocean and glacial cycles in atmospheric co2 concentration. *Nature*, *466*(7302), 47–55.

Sikes, E. L., Elmore, A. C., Allen, K. A., Cook, M. S., and Guilderson, T. P. (2016). Glacial water mass structure and rapid $\delta$ 18 o and $\delta$ 13 c changes during the last glacial termination in the southwest pacific. *Earth and Planetary Science Letters*, *456*, 87–97.

Skinner, L., Primeau, F., Freeman, E., de la Fuente, M., Goodwin, P., Gottschalk, J., Huang, E., McCave, I., Noble, T., and Scrivner, A. (2017). Radiocarbon constraints on the glacial ocean circulation and its impact on atmospheric co2. *accepted for Nature Communications*.

Somes, C. J., and Oschlies, A. (2015). On the influence of non-Redfield dissolved organic nutrient dynamics on the spatial distribution of N2 fixation and the size of the marine fixed nitrogen inventory. *Global Biogeoch. Cyc.*, *29*(7), 973–993.

Somes, C. J., Schmittner, A., Galbraith, E. D., Lehmann, M. F., Altabet, M. A., Montoya, J. P., Letelier, R. M., Mix, A. C., Bourbonnais, A., and Eby, M. (2010). Simulating the global distribution of nitrogen isotopes in the ocean. *Global Biogeochemical Cycles*, *24*(4).

Somes, C. J., Schmittner, A., Muglia, J., and Oschlies, A. (2017). A three-dimensional model of the marine nitrogen cycle during the last glacial maximum constrained by sedimentary isotopes. *Front. Mar. Sci.*, *4*, 108.

Stocker, T. F., Qin, D., Plattner, G.-K., Tignor, M., Allen, S. K., Boschung, J., Nauels, A., Xia, Y., Bex, V., Midgley, P. M., et al. (2013). Climate change 2013. the physical science basis. working Group I contribution to the fifth assessment report of the intergovernmental panel on climate change-abstract for decision-makers. Tech. rep., Groupe d'experts intergouvernemental sur l'evolution du climat/Intergovernmental Panel on Climate Change-IPCC, C/O World Meteorological Organization, 7bis Avenue de la Paix, CP 2300 CH-1211 Geneva 2 (Switzerland).

Tagliabue, A., Aumont, O., and Bopp, L. (2014). The impact of different external sources of iron on the global carbon cycle. *Geophysical Research Letters*, *41*(3), 920–926.

Tagliabue, A., Aumont, O., DeAth, R., Dunne, J. P., Dutkiewicz, S., Galbraith, E., Misumi, K., Moore, J. K., Ridgwell, A., Sherman, E., et al. (2016). How well do global ocean biogeochemistry models simulate dissolved iron distributions? *Global Biogeochem. Cy.*, *30*, 149–174.

Tagliabue, A., Bopp, L., Dutay, J.-C., Bowie, A. R., Chever, F., Jean-Baptiste, P., Bucciarelli, E., Lannuzel, D., Remenyi, T., Sarthou, G., et al. (2010). Hydrothermal contribution to the oceanic dissolved iron inventory. *Nature Geoscience*, *3*(4), 252–256.

Tagliabue, A., Bopp, L., Roche, D., Bouttes, N., Dutay, J.-C., Alkama, R., Kageyama, M., Michel, E., and Paillard, D. (2009). Quantifying the roles of ocean circulation and biogeochemistry in governing ocean carbon-13 and atmospheric carbon dioxide at the last glacial maximum. *Climate of the Past*, *5*(4), 695–706.

Tagliabue, A., Bowie, A. R., Boyd, P. W., Buck, K. N., Johnson, K. S., and Saito, M. A. (2017). The integral role of iron in ocean biogeochemistry. *Nature*, *543*(7643), 51–59.

Tagliabue, A., Mtshali, T., Aumont, O., Bowie, A., Klunder, M., Roychoudhury, A., and Swart, S. (2012). A global compilation of dissolved iron measurements: focus on distributions and processes in the southern ocean. *Biogeosciences*, *9*(6), 2333–2349.

Takahashi, T., Feely, R. A., Weiss, R. F., Wanninkhof, R. H., Chipman, D. W., Sutherland, S. C., and Takahashi, T. T. (1997). Global air-sea flux of co2: An

estimate based on measurements of sea–air pco2 difference. *Proceedings of the National Academy of Sciences*, *94*(16), 8292–8299.

Toggweiler, J., and Samuels, B. (1995). Effect of Drake Passage on the global thermohaline circulation. *Deep Sea Res. Pt I*, *42*(4), 477–500.

Ullman, D., LeGrande, A., Carlson, A., Anslow, F., and Licciardi, J. (2014). Assessing the impact of Laurentide ice sheet topography on glacial climate. *Climate of the Past*, *10*, 487–507.

Völker, C., and Tagliabue, A. (2015). Modeling organic iron-binding ligands in a three-dimensional biogeochemical ocean model. *Marine Chemistry*, *173*, 67–77.

Waelbroeck, C., Paul, A., Kucera, M., Rosell-Melé, A., Weinelt, M., Schneider, R., Mix, A. C., Abelmann, A., Armand, L., Bard, E., et al. (2009). Constraints on the magnitude and patterns of ocean cooling at the last glacial maximum. *Nature Geoscience*, *2*(2), 127–132.

Weaver, A. J., Eby, M., Wiebe, E. C., Bitz, C. M., Duffy, P. B., Ewen, T. L., Fanning, A. F., Holland, M. M., MacFadyen, A., Matthews, H. D., et al. (2001). The UVic earth system climate model: Model description, climatology, and applications to past, present and future climates. *Atmos. Ocean*, *39*(4), 361–428.

Weaver, A. J., Sedláček, J., Eby, M., Alexander, K., Crespin, E., Fichefet, T., Philippon-Berthier, G., Joos, F., Kawamiya, M., Matsumoto, K., et al. (2012). Stability of the atlantic meridional overturning circulation: A model intercomparison. *Geophysical Research Letters*, *39*(20).

Weber, S., Drijfhout, S., Abe-Ouchi, A., Crucifix, M., Eby, M., Ganopolski, A., Murakami, S., Otto-Bliesner, B., Peltier, W., et al. (2007). The modern and glacial overturning circulation in the Atlantic Ocean in PMIP coupled model simulations. *Climate of the Past*, *3*(1), 51–64.

Winckler, G., Anderson, R. F., Jaccard, S. L., and Marcantonio, F. (2016). Ocean dynamics, not dust, have controlled equatorial pacific productivity over the past 500,000 years. *Proceedings of the National Academy of Sciences*, *113*(22), 6119–6124.

Winton, V., Edwards, R., Delmonte, B., Ellis, A., Andersson, P., Bowie, A., Bertler, N., Neff, P., and Tuohy, A. (2016). Multiple sources of soluble atmospheric iron to Antarctic waters. *Global Biogeoch. Cyc.*, *30*, 421–437.

Wunsch, C. (2003). Determining paleoceanographic circulations, with emphasis on the last glacial maximum. *Quaternary Science Review*, *22*(2), 371–385.

Wunsch, C. (2016). Pore fluids and the LGM ocean salinityreconsidered. *Quaternary Science Review*, *135*, 154–170.

Zeebe, R. E., and Wolf-Gladrow, D. A. (2001). *CO2 in seawater: equilibrium, kinetics, isotopes*. Gulf Professional Publishing.

Zhang, X., Lohmann, G., Knorr, G., and Purcell, C. (2014). Abrupt glacial climate shifts controlled by ice sheet changes. *Nature*, *512*(7514), 290–294.

Zhang, X., Lohmann, G., Knorr, G., and Xu, X. (2013). Different ocean states and transient characteristics in last glacial maximum simulations and implications for deglaciation. *Climate of the Past*, *9*, 2319–2333.